ENTROPY OF JAMMED GRANULAR MATTER

by

Christopher Briscoe

A dissertation submitted to the Graduate Faculty in Physics in partial fulfillment of the requirements for the degree of Doctor of Philosophy, The City University of New York

2009

This manuscript has been read and accepted for the
Graduate Faculty in Physics in satisfaction of the
dissertation requirement for the degree of Doctor of Philosophy.

Prof. Hernãn Makse

Date — Chair of Examining Committee

Prof. Steven Greenbaum

Date — Executive Officer

Prof. Hernãn Makse, Physics Department, CCNY

Prof. Joel Koplik, Physics Department, CCNY

Prof. Jeff Koberstein, Chemical Engineering Department, Columbia University

Prof. Mark Shattuck, Physics Department, CCNY

Prof. Charles Maldarelli, Chemical Engineering Department, CCNY

Supervisory Committee

THE CITY UNIVERSITY OF NEW YORK

Abstract

ENTROPY OF JAMMED GRANULAR MATTER

by

Christopher Briscoe

Adviser: Professor Hernán A. Makse

Granular matter can be considered a non-equilibrium system, such that equilibrium statistics is insufficient to describe the dynamics. A phase transition occurs when granular materials are compressed such that a nonzero stress develops in response to a strain deformation. This transition, referred to as the *jamming transition*, occurs at a critical volume fraction, ϕ_c depending on friction and preparation protocol. Analysis of the jamming transition produces a phase diagram of jammed granular matter for identical spheres, characterized by the critical volume fraction, ϕ_c and the average coordination number, Z. The boundaries of the phase diagram are related to well-defined upper and lower limits in the density of disordered packings; random close packing (RCP) and random loose packing (RLP).

Frictional systems, such as granular matter, exhibit an inherent path dependency resulting in the loss of energy conservation, an important facet of equilibrium statistics. It has been suggested Edwards that the volume-force (V-F) ensemble, wherein volume replaces energy as the conservative quantity, may provide a sufficient framework to create a statistical ensemble for jammed granular matter. Treating a jammed system via the V-F ensemble introduces an analogue to tem-

perature in equilibrium systems. This analogue, "compactivity", measures how compact a system could be and governs fluctuation in the volume statistics.

Randomness in statistical systems is typically characterized by entropy, the equation of state derived from the number of microstates available to the system. In equilibrium statistical mechanics, entropy provides the link between these microstates and the macroscopic thermodynamic properties of the system. Therefore, calculating the entropy within the V-F ensemble can relate the available microscopic volume for each grain to the macroscopic system properties.

The entropy is shown to be minimal at RCP and maximal at the minimum RLP limit, via several methods utilizing simulations and theoretical models. Within this framework RCP is achieved in the limit of minimal compactivity and RLP is achieved in the limit of maximal compactivity. The boundaries of a phase diagram for jammed matter could thereby be defined by the limits of zero and infinite compactivities, characterizing the RCP and RLP limits of granular matter.

Acknowledgements

I am indebted to my advisor, Professor Hernán A. Makse, Physics Department and Levich Institute, City College of New York, for initiating this work and continuously supporting my research. I am also grateful for the privilege of working closely with my colleagues Dr. Ping Wang and Dr. Chaoming Song of the Physics Department and Levich Institute, City College of New York. Without their insightful projects this work would not be possible. In addition, I am grateful for useful discussions with Dr. Jasna Bruijic, Dr. Guillaume Marty, Dr. Shomeek Mukhopadhyay, Dr. Diego Rybski, Dr. Hernán Rozenfeld, Dr. Lazraros Gallos, Kun Wang and Yuliang Jin. Lastly, I would like to thank my parents for their support throughout my academic career.

Contents

List of Figures

Chapter 1

Introduction to Jammed Matter

The jammed state is defined as the condition when a many-body system is blocked in a configuration far from equilibrium, such that relaxation cannot occur within a measurable time-scale. Jamming has emerged as a governing feature in many systems, such as granular materials, emulsions, colloidal suspensions, structural glasses and spin glasses, among numerous others.

The above disordered systems are examples of non-equilibrium systems, wherein a state may occur having particles in close contact with one another and therefore experience a jamming transition. All these systems belong to a class of materials known as 'soft' matter, referring to their complex mechanical properties, being neither fluid nor solid-like. The process of jamming is specific to each system based on their particular microscopic properties. For example, pouring a granular material into a closed container, accompanied by oscillation, is sufficient to achieve the jamming condition, while glasses can be cooled down to very low temperatures at which the molecules can no longer diffuse, thus resulting in a jammed configu-

ration. Hence, through very different jamming mechanisms, the jammed state is achieved for a variety of systems.

The soft nature of these systems plays an important role in their capability to support a mechanical disturbance once it has achieved jamming. While the concepts of crowding and the subsequent mechanical response unite these materials, the details of their constituent particles introduce important differences. In a polymer melt, it is the physical chemistry of the individual strands that govern the ensemble, whereas interactions between the colloidal particles, rather than their constituent molecules, which will determine the behavior in suspensions. Further, particles up to $1\mu m$ in size obey the laws of statistical mechanics since their dynamics is due to Brownian motion. Above that threshold size, commonly seen in granular materials, the gravitational potential energy exceeds $k_B T$, prohibiting thermal motion. Therefore, the colloidal regime is defined for sizes between $1nm$ and $1\mu m$ to accommodate thermal averaging.

In a fluid at thermal equilibrium the particle dynamics is too fast to capture the detail of the underlying potential energy landscape, thus appearing flat. Decreasing the temperature impedes Brownian motion, introducing a limiting temperature below which the fluid can no longer be equilibrated. Hence, the thermal system falls out of equilibrium on the time scale of the experiment and experiences a glass transition. The motion of each particle is no longer thermally activated and only the vibration inside the cage formed by its surrounding neighbors persists. Below the glass transition temperature the particles continue to relax, but very different to equilibrium relaxation. This phenomenon of structural evolution beyond the glassy state is known as "aging". The dynamics here are dominated by the mul-

tidimensional potential energy landscape the system can explore as a function of the degrees of freedom of all constituent particles.

Unlike granular materials, a thermal system is never permanently trapped in the bottom of a valley, but escapes via accessible unstable directions through intrinsic thermal vibrations. At any finite temperature the glassy system will not resemble the granular system as the glassy system continuously evolves toward a maximum density state. The only true analogous situation between glasses and granular materials is valid at zero temperature. However, there are characteristic features of glassy relaxation at finite temperature that act as useful tools for the description of granular systems by exploiting the analogy between relaxation of granular material and glassy aging. Theories developed through the generalization of usual equilibrium relations, such as the fluctuation-dissipation relation, to situations far from equilibrium have led to better understanding of glassy systems. Further, they have resulted in macroscopic observable properties, such as an "effective temperature" for slow modes of glassy relaxation. The existence of this effective temperature suggests an ergodic long-time behavior of the system. This ergodicity is related to the statistical mechanics ideas for granular systems discussed in the present study.

1.1 Jamming in Particulate Systems

The inability to describe a granular system on the continuum level in any way except its geometrical features has led to a lack of a well established granular theory until the present. There remains a need to describe the universal features

of observations within a theoretical framework devised for granular matter, with a great deal of environmental and industrial importance.

Edwards and collaborators postulate the existence of a statistical ensemble for granular matter, despite the lack of thermal motion and the absence of an equilibrium state. The main postulate is based on jamming the granular particles at a fixed total volume such that all microscopic jammed states are equally probable and exhibit ergodicity. The exploration is achieved via an external perturbation such as tapping or shear, just as thermal systems explore their energy landscape through Brownian motion. Granular materials achieve a jammed configuration if all the constituent particles are packed together such that all particles contact their neighbors, requiring a sufficiently high packing fraction. The typical energy necessary to explore different jammed configurations is several orders of magnitude greater than the thermal energy at room temperature. There is no kinetic energy of consequence in these athermal systems.

It is of great importance to note the subtle difference between a configuration in mechanical equilibrium and a jammed configuration. Arriving at a static configuration by an increase in density is not necessarily sufficient to satisfy the jamming condition, especially when considering systems displaying a hysteresis. For example, pouring grains into a container results in a pile at a particular angle of repose. This mechanical equilibrium configuration is not jammed because in response to an external perturbation, the constituent particles will irreversibly rearrange, approaching a truly jammed configuration. The ergodic hypothesis is simply not valid in such hysteretic samples. By allowing the system to explore the available configuration space by means of external perturbation, all possible

configurations must become accessible to one another, with respect to the perturbation. Statistical analysis can only be performed on those systems having no memory of their creation, and are therefore jammed by the definition herein. The aggregate of these jammed states are thereby suitable for a plausible application of statistical mechanics.

The conditions for a statistical ensemble of jammed configurations can be achieved by implementing perturbations on a granular packing. This perturbation could be tapping, slow shearing, or another perturbation which makes effort to replicate Brownian motion in an athermal system. Starting with a low packing of grains, the perturbation initially removes unstable voids in the packing, eliminating irreversible grain motion. Once all grains are in contact with their neighbors, the density of the resulting configuration becomes dependent on the perturbation amplitude, with the density decreasing as amplitude is increased. The mechanism of this compaction process leading to a steady-state density is extremely slow, observed to depend logarithmically on the number of perturbations. The dependence of the density on the external perturbation of the system, once the hysteretic factors have been removed, is known as the reversible branch of this compaction curve, shown below.

Despite the presence of friction between grains, demanding memory effects in packing creation, this curve is reversible, establishing a new type of equilibrium state. It is along this curve that the statistical mechanics for jammed granular matter can be applied. There have been many experiments confirming these results for different system geometries, particle elasticities and compaction techniques. For example, the system can be mechanically tapped or oscillated, slowly sheared in

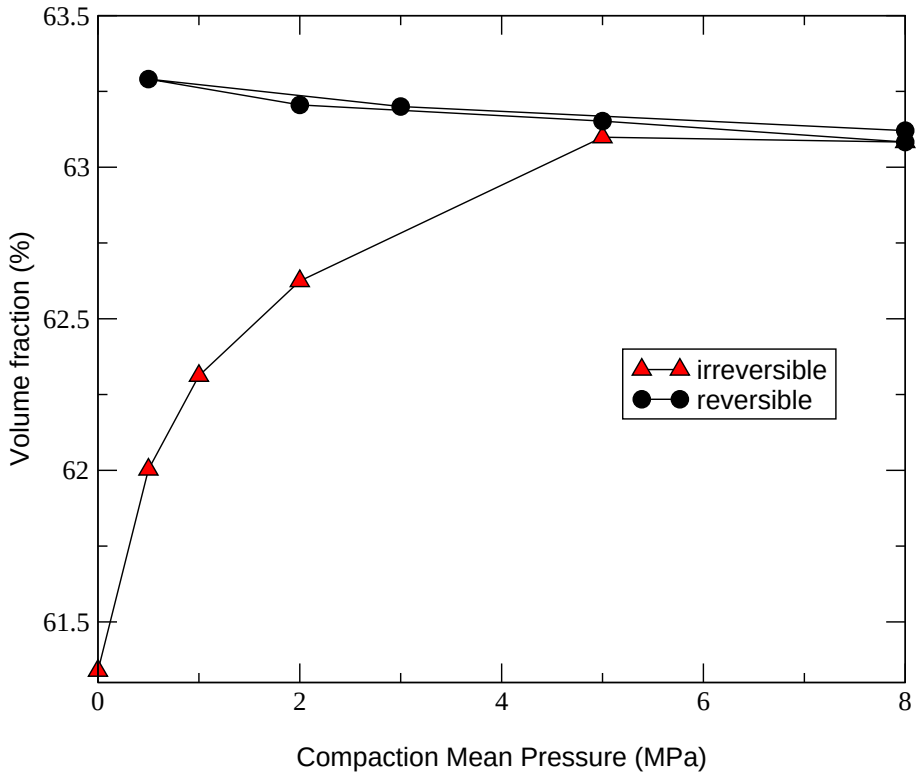

Figure 1.1: Compaction curve for a packing of glass beads under an oscillating pressure. Increasing the amplitude of oscillation initially increases the density by filling the loose voids, after which a reversible regime is achieved.

Couette cell geometry, or allowed to relax under large pressures over long periods of time, all with the same compaction curve. If the application of statistical mechanics to jammed configurations proves reasonable, macroscopic quantities of the non-equilibrium system could be predicted, such as viscosity and complex shear moduli, thereby providing thorough rheological characterization. It is here where industrial applications become evident. Further, a statistical ensemble for jammed matter could be among the few generalizations of the statistical mechanics of Gibbs and Boltzmann to systems in non-equilibrium conditions.

It is important to note that infinitely rigid grains have been considered, where an increase in the system pressure, by placing a piston on top of the grains for example, causes no change in the shape of the grains and therefore no change in the density. Clearly, real grains have a finite elastic modulus, and application of a sufficiently large external pressure will result in grain deformation, inducing a density increase unrelated to the external perturbation. In softer particles, such as emulsions, the effect of pressure is more significant. The tapping experiment described above measured the resulting densities at atmospheric pressure, which is considered to be zero reference pressure. The same experiment can be repeated at finite pressures giving rise to equivalent compaction curves, depicted below

While hard grains, such as glass beads, require large pressures ($1MPa$) to deform, softer matter, such as rubber, can reach higher densities at lower pressures.

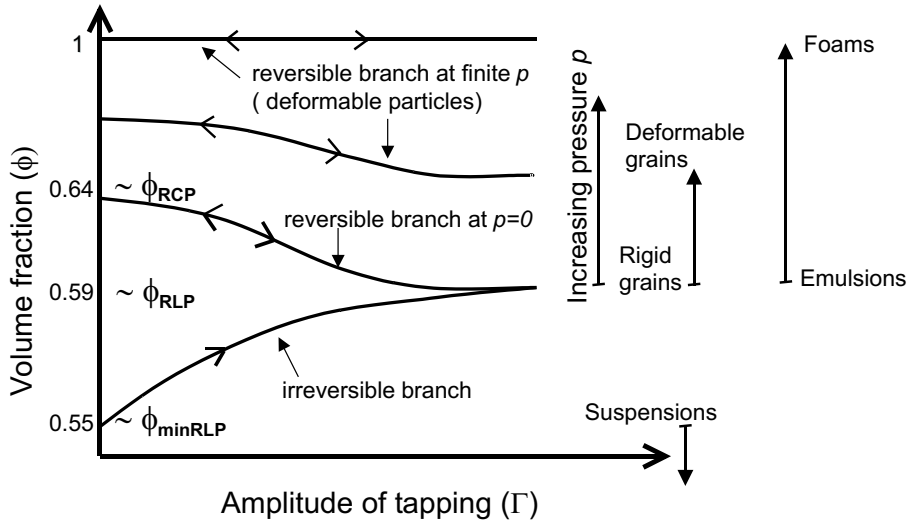

Figure 1.2: Compaction curves of volume fraction ϕ versus amplitude of oscillation A for different external confining pressures, p. Increasing the amplitude of oscillation initially increases the volume fraction by filling the loose voids (irreversible branch), after which a reversible regime is achieved. For infinitely rigid grains (the "zero pressure" curve) the minimum volume fraction along the irreversible branch is the random loose packing. The reversible branch goes from the maximum random loose packing fraction to the random close packing fraction. Below the minimum RLP only suspensions can exist.

1.2 Statistical Mechanics of Jammed Matter

In the conventional statistical mechanics of thermal systems, the different possible configurations, or microstates, of the system are given by points in the phase space of all positions and momenta, p and q, of the constituent particles. The equilibrium probability density ρ_{eqm} must be a stationary state of Louisville's equation which implies ρ_{eqm} must be expressed only in terms of the total energy of the system, E. The simplest form for a system with Hamiltonian $H(p, q)$ is the microcanonical distribution:

$$\rho_{\text{eqm}}(E) = \frac{1}{\Sigma_{\text{eqm}}(E)}, \tag{1.1}$$

for the microstates within the ensemble, $\mathcal{H}(p, q) = E$, and zero otherwise. Here,

$$\Sigma_{\text{eqm}}(E) = \int \delta(E - \mathcal{H}(p, q)) \;\; dp \; dq, \tag{1.2}$$

is the area of energy surface $\mathcal{H}(p, q) = E$.

This is the statement that all microstates are equally probable. Assuming this, the true distribution of the system implies accepting the ergodic hypothesis, where the trajectory of the closed system will pass arbitrarily close to any point in phase space. Boltzmann associated the number of microstates with the thermodynamic entropy through his formula

$$S_{\text{eqm}}(E) = k_B \log \Omega_{\text{eqm}}(E). \tag{1.3}$$

In classical, equilibrium, statistical mechanics, the total energy of the system

is sufficient to describe the density of states, and therefore explore the phase, or configuration, space. A new statistical method, unrelated to the temperature, must be constructed for granular matter.

Consider a jammed granular system composed of infinitely rigid grains of a specified shape. Such a system is analogously described by a network of contacts between the constituent particles in a fixed volume, V. For granular materials, the analogue of phase space, the space of microstates of the system, is the space of possible jammed configurations as a function of the degrees of freedom of the system, ζ. It is proposed that is the volume of this system, V, rather than the energy, E, which is the key macroscopic quantity governing granular material. The statistics of this system would then be defined by a function $W(\zeta)$, a function giving the volume of the system in terms of the degrees of freedom, replacing the Hamiltonian, $H(p, q)$. The average of $W(\zeta)$ over all the jammed configurations determines the volume V of the system in the same way as the average of the Hamiltonian determines the average energy of the system.

Several methods exist for determining the correct $W(\zeta)$ function. In this study, Delaunay triangulation along with Voronoi tessellation will be heavily utilized in describing the volume per particle of the system. Starting from any arbitrary grain in a 2d system, one would draw a line connecting that grain to all other grains, and then bisect each line. The smallest possible area created by the intersection of the bisections would define the area inside of which all points are closer to the original grain than any other. This area is the Voronoi volume for the original grain, and the method is then further extended to the entire granular system, covering the entire volume.

Using an explicitly defined $W(\zeta)$ it is possible to define the entropy of the granular packing. The number of microstates for a given volume V is measured by the area of the surface $W(\zeta) = V$ in the phase space of jammed configurations and is given by:

$$\Sigma_{\text{jammed}}(V) = \int \delta\Big(V - \mathcal{W}(\zeta)\Big) \;\; \Theta(\zeta) \;\; d\zeta, \tag{1.4}$$

$\Theta(\zeta)$ is a constraint that restricts the integral to only reversible jammed configurations as opposed to merely static equilibrium configurations as discussed above. The novelty in this approach is the assumption of equally probable microstates which leads to analogous entropy associated with this statistical quantity:

$$S(V) = \lambda \log \Sigma_{\text{jammed}}(V) = \lambda \log \int \delta(V - \mathcal{W}(\zeta)) \;\; \Theta(\zeta) \;\; d\zeta, \tag{1.5}$$

where, λ is the analogue of the Boltzmann constant. The analogue of temperature, named the "compactivity", is defined as

$$X^{-1} = \frac{\partial S}{\partial V}. \tag{1.6}$$

where the subscript V refers to the derivative of the entropy with respect to the volume.

Compactivity can be interpreted as a measure of how much more compacted the system could be, such that a higher compactivity implies a loose configuration, tending towards random loose packing, RLP. A lower compactivity implies a more compact structure tending towards random close packing, RCP, the densest possible random packing of mono-disperse hard spheres. With respect to the com-

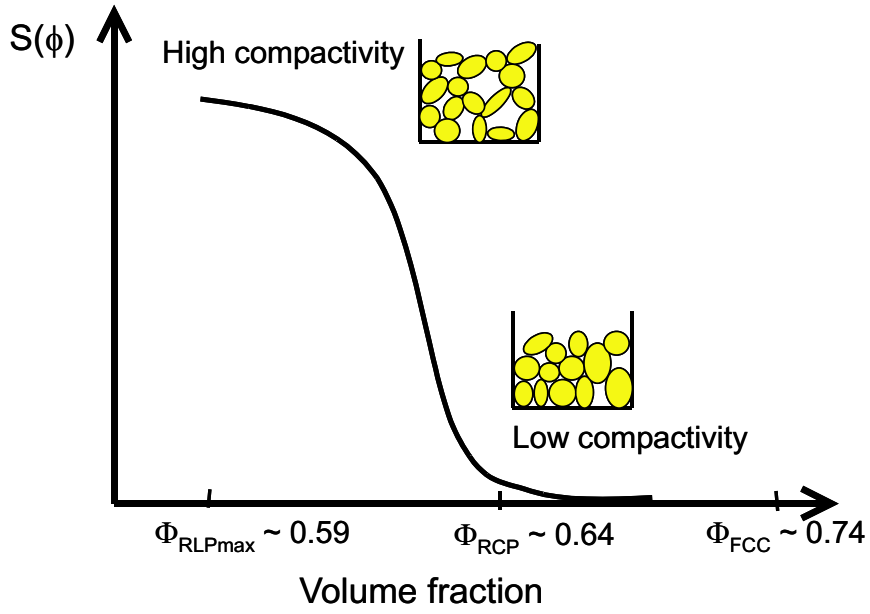

Figure 1.3: Interpretation of the compactivity and entropy in terms of different packings.

paction curve, large amplitudes generate packings of high compactivities, while in the limit of the amplitude going to zero a low compactivity is achieved. In terms of the entropy, many more configurations are available at high compactivity, as shown in the figure below:

At any given tapping amplitude, there exists an equilibrium volume fraction toward which the system slowly evolves. For instance, a system may find itself at a lower entropy than the equilibrium curve by the application of an internal constraint at a given volume fraction. This situation can be achieved by creating small crystalline regions within a packing configuration of a lower density, and looser regions compensating for the volume reduction such that the total volume of the system remains constant. This configuration, given that it is not jammed, will tend toward the equilibrium packing via the application of a small perturbation

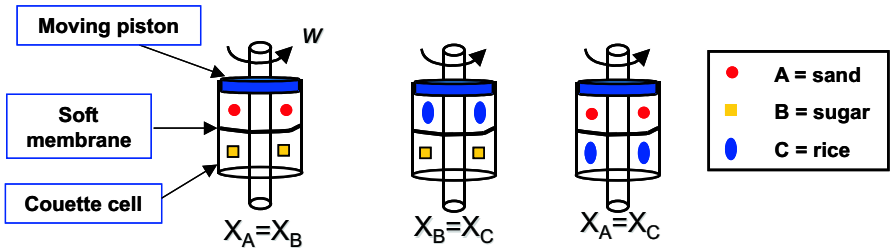

Figure 1.4: ABC experiment to test the zero-th law of granular thermodynamics.

by increasing its entropy.

It becomes clear from Eq. (1.6) that the compactivity is only applicable in equilibrated jammed states. As an analogue of temperature, it should also obey the zero-th law of thermodynamics. Hence, two different powders in physical contact with one another should equilibrate at the same compactivity, given a mechanism of momentum transfer between the two systems. Indeed, one may think of an appropriate laboratory experiment which would test this hypothesis under certain conditions necessary for creating the analogous situation to heat flow.

Two powders, A and B, of different grain types are poured into a vertical Couette cell as shown in Fig. 1.4. The grains must experience an equivalent tapping or shearing regime, which is achieved by the rotation of the inner cylinder of the Couette cell. The species are separated by a flexible diaphragm, such that momentum transfer between the two systems is ensured. The two powders must be well separated such that there is no mixing involved, but in contact nevertheless. The grains are kept at a constant pressure by a piston which is allowed to move freely to accommodate for the changes in volume experienced by the two types of grains. Gravity may play a role in the experiment, which is avoided by density matching the particles with a suspending fluid.

The experiment consists in placing powders A and B together in the above cell and slowly shearing them at a given velocity. The powders should come to equilibrium volumes V_A and V_B, with equivalent respective compactivities, $X_A = X_B = X$. In the absence of a compactivity scale, powder B is used as a 'thermometer' by placing it in contact with a third powder C. The volume B is kept at V_B and the volume of C is allowed to fluctuate until it reaches the equilibrium state. Finally, powders A and C are put together to test if they will reach the same volumes as they did in previous runs in contact with B, thus proving the zeroth law.

It should be noted that a packing fraction of 0.74, or FCC, cannot be reached by external perturbation. For a given perturbation amplitude, the system will slowly evolve towards an equilibrium volume fraction. Under the assumption that the system is not jammed, the external perturbation will adjust the volume fraction towards this value by increasing the entropy of the system. It is therefore important to develop a Boltzmann equation for jammed systems and show that this analysis can produce a second law of thermodynamics, $\delta S \geq 0$ for granular matter, the equality arising when the definition for the entropy of a jammed system is achieved. Such an equation would suggest proof for this entropy as a basis for granular statistical mechanics.

Boltzmann used basic assumptions and arguments with respect to particle interaction, including but not limited to two-body collision domination, as well as the un-correlation of collisions in the two-body process, in an effort to prove the now infamous second law of thermodynamics, stated simply here as:

$$\frac{\partial S}{\partial t} \geq 0, \tag{1.7}$$

Without exploring the exact details of Boltzmann's work, the Boltzmann distribution, shown below, is obtained when the condition of detailed balance is achieved

$$f(\nu) = (\frac{k_B T}{m\pi})^{\frac{3}{2}} e^{-\beta m \nu^2/2}, \tag{1.8}$$

Simplifying this equation even further, the kinetic energy is replaced by the total system energy

$$P(E) \propto e^{-\beta E}, \tag{1.9}$$

and via analogous approach, the following result is obtained for granular systems:

$$P(W) \propto e^{-W/\lambda X}, \tag{1.10}$$

presented here without complete proof, deferring to the literature to show $\delta S \geq 0$ for granular matter.

Analysis of a dynamic system of jammed matter reveals an extrapolation to a static system without negligible statistical mechanical properties. Therefore, the necessity to study a static jammed system, and characterize compactivity and entropy therein, if furthered as exemplified in the next chapter.

Chapter 2

Effective Temperature in A Sheared Couette Cell

2.1 Introduction

Fluctuation-Dissipation (FD) relations are commonly used in equilibrium systems, derived from the notion that small perturbations and Brownian fluctuations produce the same response in a given system [1]. Mobility, the constant of proportionality between a particles drift speed and a constant external force, is extracted from velocity statistics of particles in a given system. Diffusivity, calculated from fluctuation displacements of particles in a system over time, represent the Brownian motion. The temperature of a system in thermodynamic equilibrium can be extracted from a FD relation, defined as the ratio of diffusivity and mobility, as is commonly used in the Einstein relation. In equilibrium this temperature is taken to be the bath temperature.

In recent studies theoretical mean-field models of glasses [2] have introduced the concept of an "effective temperature" as extracted from the FD relations in non-equilibrium systems. While not equivalent to the equilibrium bath temperature, the effective temperature reflects a change in the relaxation time-scale of the system. These non-equilibrium systems extend beyond glasses, and into granular media, where physical size of the constituent grains inhibits motion, allowing for jammed systems far from equilibrium. This concept has been furthered by computer simulations of granular media and other non-equilibrium soft-matter systems [3, 4, 5, 6, 7, 8]. It remains an open question whether or not granular media can be characterized by an effective temperature, thus revealing a dynamic counterpart to the static "compactivity" as proposed by Edwards [9].

Athermal systems require the input of energy by an external source to explore the effective temperature [10]. One proposed method of calculating the effective temperature of a jammed granular system is a slow shearing procedure [11, 12, 13, 14, 15, 16, 17], leading to the design of the experiment presented in [18]. Slow shearing, at the quasi-static limit, allows for extrapolation towards an effective temperature of jammed, static, systems. The jammed system of interest is one of identical, spherical grains, confined between the two cylindrical walls of a 3D Couette cell. The grains are further confined by an external pressure in the vertical direction. The inner cylinder of the Couette cell is slowly rotated to induce shearing in the system. Tracer particles are inserted in the system, and their trajectories recorded in cylindrical coordinates, $(r(t), \theta(t), z(t))$ via multiple cameras surrounding the system. The Couette cell is partially filled with a refractive index matched fluid to allow for system transparency. The cylindrical walls are

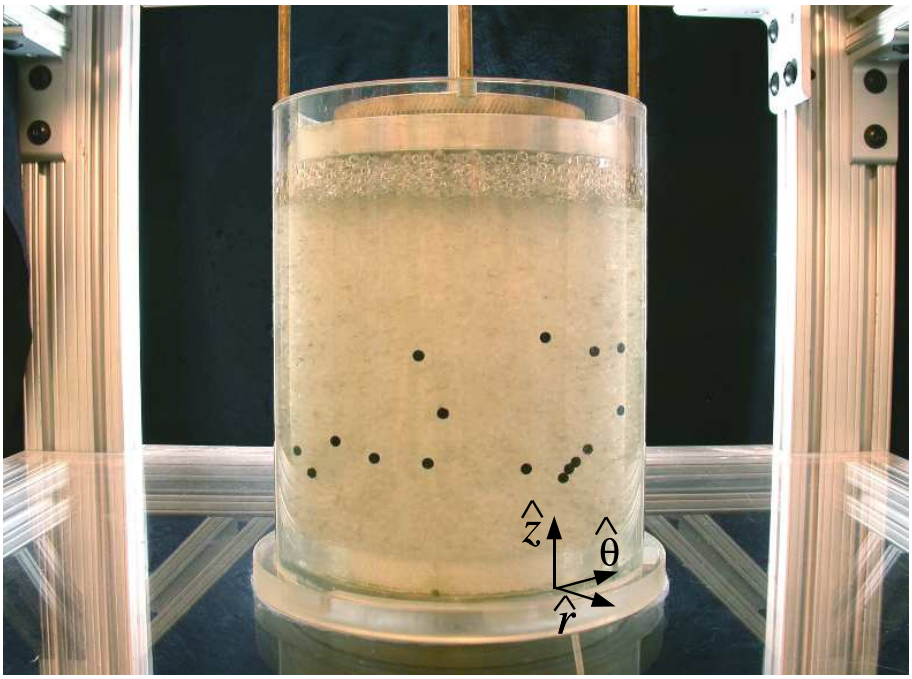

Figure 2.1: Picture of experimental set-up. Transparent acrylic grains and black tracers in a refractive index and density matched solution are confined between the inner cylinder of radius 5.08cm and the outer cylinder of radius 6.67cm.

roughened by gluing grains, identical to those of the bulk, such that crystallization is avoided.

Distributions of tracer particle displacements are measured in each direction. As gravity is the external force applicable to the mobility calculation in the current formalism, only displacements in the z-direction are applied to the FD relation. Additionally, average velocity profiles are calculated for each direction, first with constant shear rate, $\dot{\gamma}_e$, and further studied to determine shear rate dependence. Displacement measurements are further limited to the "constant mobility and diffusivity" (CMD) region, defined as the narrow range of radial coordinates such that the average vertical velocity is roughly independent of radial distance.

Utilizing the FD relations presented above, the diffusivity and mobility in the z-direction are extracted from the tracer particle trajectories and the effective temperature is realized. This effective temperature is found to be independent of tracer particle properties, as shown in [18], and further independent of the slow-shear rate. Moreover, the effective temperature may then be considered a physical variable that characterizes the jammed granular system, with respect to the generalization of the equilibrium statistical mechanics of Boltzmann, as applied to non-equilibrium systems.

Here, the limits within which this effective temperature may be a valid physical variable are studied, as mobility and diffusivity as a function of shear rate are determined. While diffusivity appears independent of shear rate, even somewhat above the 'slow' regime, mobility shows a clear decrease in magnitude for shear rates above the slow regime, resulting in an increase in the effective temperature as a function of shear rate.

2.2 Experimental Method

2.2.1 Experimental Setup

The grains are confined between two cylinders of height 19.0cm. The inner cylinder is rotated via a motor, while the outer cylinder remains fixed. The walls of the cylinders, in contact with the grains, are roughened by means of a glued layer of identical granular material, thereby minimizing wall slip. The walls of the inner and outer cylinders are roughened by acrylic beads with diameter 3.97mm and 1.59mm, respectively. Testing the experiment with a rough inner wall and a smooth outer wall resulted in packing crystallization. The grains are compacted by an external pressure of a specific value (typically 386 Pa), introduced by a moving piston at the top of the granular material, acting in the negative z-direction.

Observation techniques are used to monitor the granular packing evolution as it explores the available jammed configurations. The Couette cell is sheared at the quasi-static limit, with slow frequencies $f = 0.2 \sim 4.2$ mHz defining the external shear-rate $\dot{\gamma}_e = 2\pi f R_1/(R_2 - R_1) = \omega R_1/(R_2 - R_1) = 0.004 \sim 0.084$ s^{-1}, where $R_1 = 5.08$cm and $R_2 = 6.67$cm are the radius of the inner and outer cylinders, respectively, and ω is the angular velocity of the inner cylinder Note that R_1 and R_2 are measured after the walls are roughened by a glued layer of beads. The experiment is designed to measure the diffusivity and mobility of tracer particles [8, 18, 19], as opposed to tracking the motion of all constituent grains. The distance between the inner and outer cylinder is less than 10 grain diameters to prevent bulk shear band formation [16, 17, 13, 12, 15] that may interfere with the experimental measurements by altering the diffusivity.

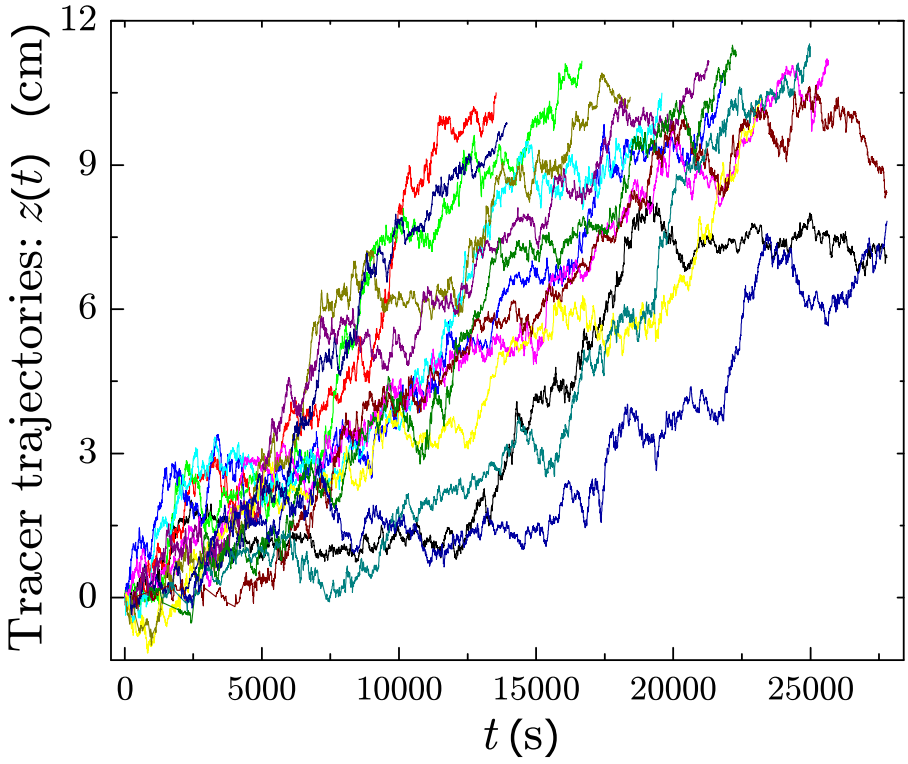

Figure 2.2: (Color online) Trajectories of the 3.97mm nylon tracers in Packing 1 showing the diffusion and response to the gravitational force when sheared in the Couette cell.

A refractive index matching suspending solution is employed in order to create a transparent sample. The suspending solution is also density matched to the grains in order to eliminate pressure gradients derived from gravity in the vertical direction, circumventing problems seen in previous experiments of compactivity [20] and other effects such as convection and size segregation such as the Brazil nut effect inside the cell [21].

2.2.2 Packing Preparation

The granular system is a bidisperse, 1:1 by mass, mixture of spherical, transparent Poly-methyl methacrylate (acrylic) particles, with density $\rho = 1.19$ and index of refraction $n \simeq 1.49$. The bidisperse mixture is used in an effort to inhibit crystallization of the system. The respective particle diameters are either 3.17mm and 3.97mm (Packing 1) or 3.97mm and 4.76mm (Packing 2). The approximate same size ratio of each bidisperse packing leads to approximately the same value of volume fraction for both, being 0.62 before shearing and 0.58 during shearing.

A negative consequence of utilizing a suspending solution includes possible modification of the friction coefficient between the grains. While this cannot be completely avoided, it is important to note that the liquid only partially fills the cell, such that the pressure of the piston is transmitted to the granular material exclusively, not to the fluid. Additionally, hydrodynamic effects from partial cell filling are avoided by the extremely slow rotational speeds applied to the system. The system remains very closely packed, such that particles are not free to float in the fluid. Therefore, the random motion of the particles is controlled by the 'jamming' forces exerted by the contacts between neighboring grains, not fluid

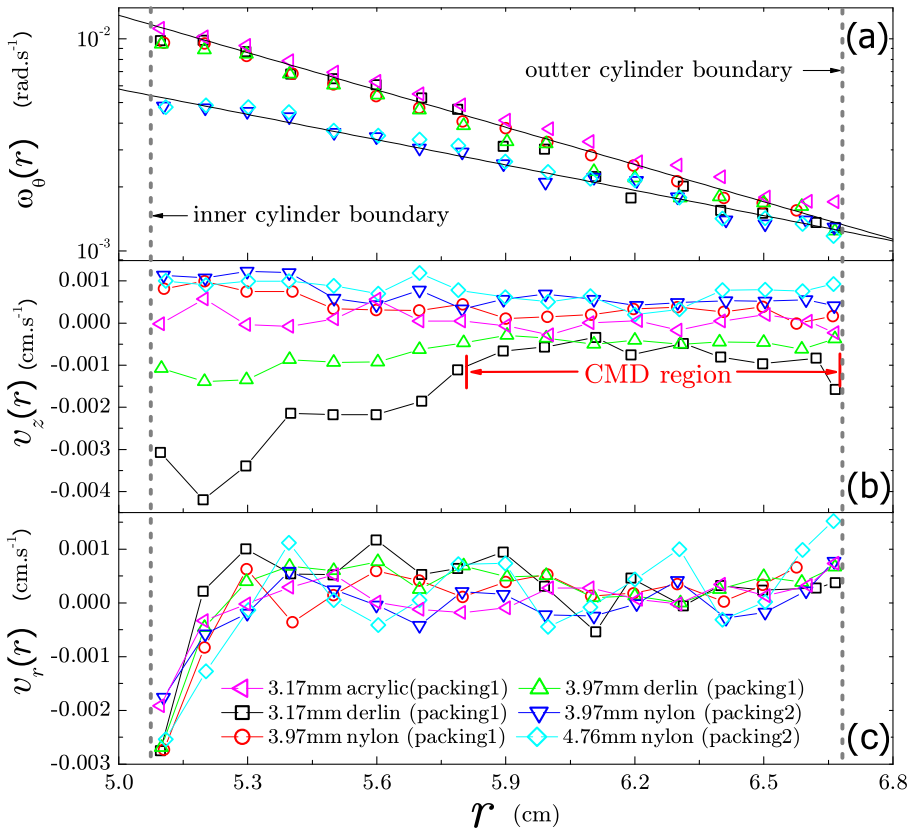

Figure 2.3: (a) Average angular velocity, $\omega_\theta(r)$, (b) Average vertical velocity, $v_z(r)$, and (c) Average radial velocity, $v_r(r)$, versus radial distance r for various tracers and different packings. Packing 1 and Packing 2 are run at $\dot{\gamma}_e = 0.048, 0.024\text{s}^{-1}$, respectively. In (a), solid lines are exponential fitting. In (b), the positive velocity of nylon tracer is due to the smaller density than acrylic's. The negative velocity of delrin tracer is due to the higher density than acrylic's.

mechanics.

2.2.3 Implementation of Fluctuation-Dissipation Theory

For systems in thermal equilibrium, a Fluctuation-Dissipation (FD) relation may be utilized in an effort to calculate the bath temperature of the system. This method may be extended to non-equilibrium systems, such as jammed granular systems presented in this study. The FD relation is defined as follows:

$$\langle [x(t+\Delta t) - x(t)]^2 \rangle \sim 2D\Delta t, \tag{2.1}$$

$$\langle [x(t+\Delta t) - x(t) \rangle \sim MF\Delta t, \tag{2.2}$$

$$\langle [x(t+\Delta t) - x(t)]^2 \rangle = \ 2T_{\text{eff}} \ \frac{\langle x(t+\Delta t) - x(t) \rangle}{F}. \tag{2.3}$$

The tracer particles must experience a constant force, F, in order to calculate the mobility as defined above. The most convenient constant, external, force is gravity in the z-direction. If the effective temperature is to be regarded as an intensive variable of the non-equilibrium system, it requires independence from the tracer particles properties. However, temperature measurements from multiple observables would be necessary to analyze the underlying thermodynamic meaning of T_{eff}.

2.2.4 Properties of Tracer Particles

Tracer particles added to the bulk must have properties unique from the grains comprising the bulk. However, tracer particles too small, or too large, with respect to the acrylic grains described previously, would result in erroneous measurements. Dynamics of tracer particles that were too small would be dominated by "percolation effects" [22], resulting in larger than expected tracer particle displacements. Those too large would require shear rates above the quasi-static limit studied herein, or possibly have no dynamics at all due to size limitations. With these notions in mind, two different types of tracers, nylon ($\rho' = 1.12$) and delrin ($\rho' = 1.36$), are employed, which result in different external forces, $F = (\rho' - \rho)Vg$, where ρ and ρ' are the densities of the acrylic particles and the tracers, respectively, V is the volume of the tracer particle and g the gravitational acceleration. Variations in tracer particle diameter and density allow us to study dynamical changes due to a change in constant external force, while remaining within a range appropriate to achieve results expected to be governed by the effective temperature.

2.3 Results

2.3.1 Average Velocity Profiles

Velocity profiles for a fixed shear rate, $\dot{\gamma}_e$, are presented followed by a study on the shear rate dependence in the next section. The average velocity profile in the vertical direction, $v_z(r)$, is obtained by averaging the velocities of all tracer particles over all times at each radius r, as shown in Fig. 2.3. The mean vertical

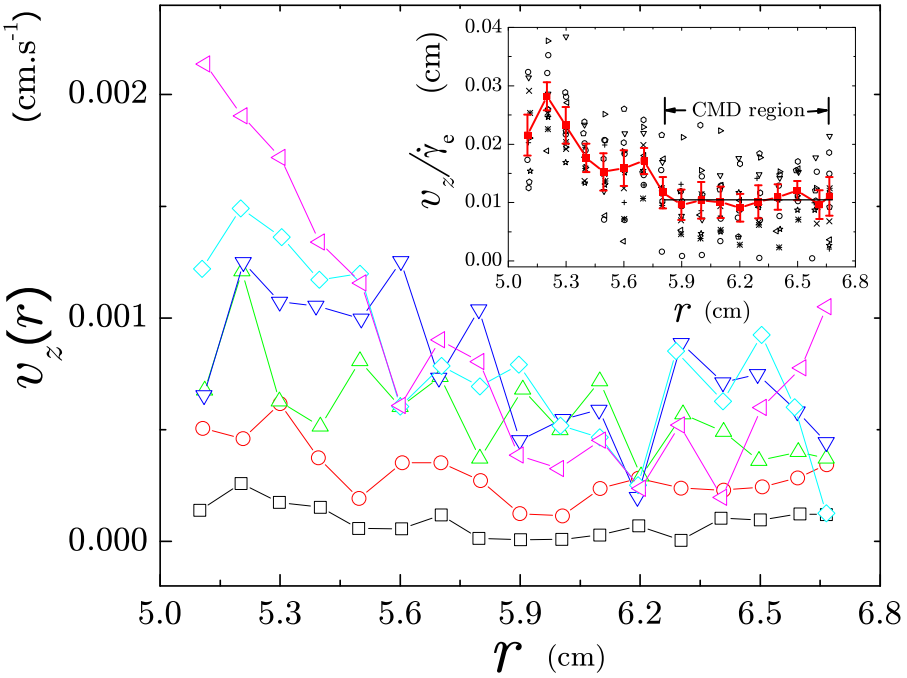

Figure 2.4: Average vertical velocity of tracers, $v_z(r)$, versus radial distance r for various shear rate $\dot{\gamma}_e$ in Packing 2. Black square, red circle, green triangle, blue triangle-down, cyan diamond, magenta triangle-left are corresponding to $\dot{\gamma}_e = 0.008, 0.016, 0.032, 0.048, 0.060, 0.084\text{s}^{-1}$, respectively. The inset plots the collapsing of average vertical velocity scaled by shear rate, $v_z(r)/\dot{\gamma}_e$, versus radial distance r for various shear rate $\dot{\gamma}_e$. The red solid curve is the average result of the collapsing.

velocity of tracer particles does not decay to zero even if the tracers come close to outer cylinder surface, due to the grains glued to the cylindrical walls, as shown in Fig. 2.4 at $r = R_2$.

In order to avoid the tracer particles sticking to the outer cylinder surface and forcing its velocity to zero, smaller sized particles are glued to roughen the outer cylinder. This roughens the surface of the outer cylinder and avoids crystallization. Further, this allows slipping of the bulk particles at the outer cylinder, forcing the shear band to be located exactly at the outer cylinder, not in the bulk. The glued particles are 1.59mm, smaller than the sheared granular material. The mean angular and vertical velocity, v_z, of tracer particles do not decay to zero even if the tracers come close to outer cylinder surface, as shown in Fig. 2.4 at $r = R_2$.

As shown in Fig. 2.3b, there exists a plateau in the vertical velocity profile which can be further seen in Fig. 2.4. Similar behavior is observed in the vertical diffusivity profile, $D_z(r)$ as shown in Fig. 2.6, discussed in detail in Section 2.3.3. This is denoted the "constant mobility and diffusivity region", i.e., CMD region, 5.80cm $< r <$ 6.67cm. Contrary to prior work [11, 12, 13, 14, 15, 16, 17] on sheared granular matter in the Couette cell, this experiment focuses only a narrow radial gap of Couette cell. The CMD region allows us to well define the diffusivity and mobility of the tracer particles, such that average vertical velocity, v_z, and the average vertical diffusivity, D_z, are calculated by averaging the velocities of all tracers over all times in the CMD region, significantly improving the statistics. In this study, the statistical average and the measurements of tracer fluctuations will be confined only to the CMD region.

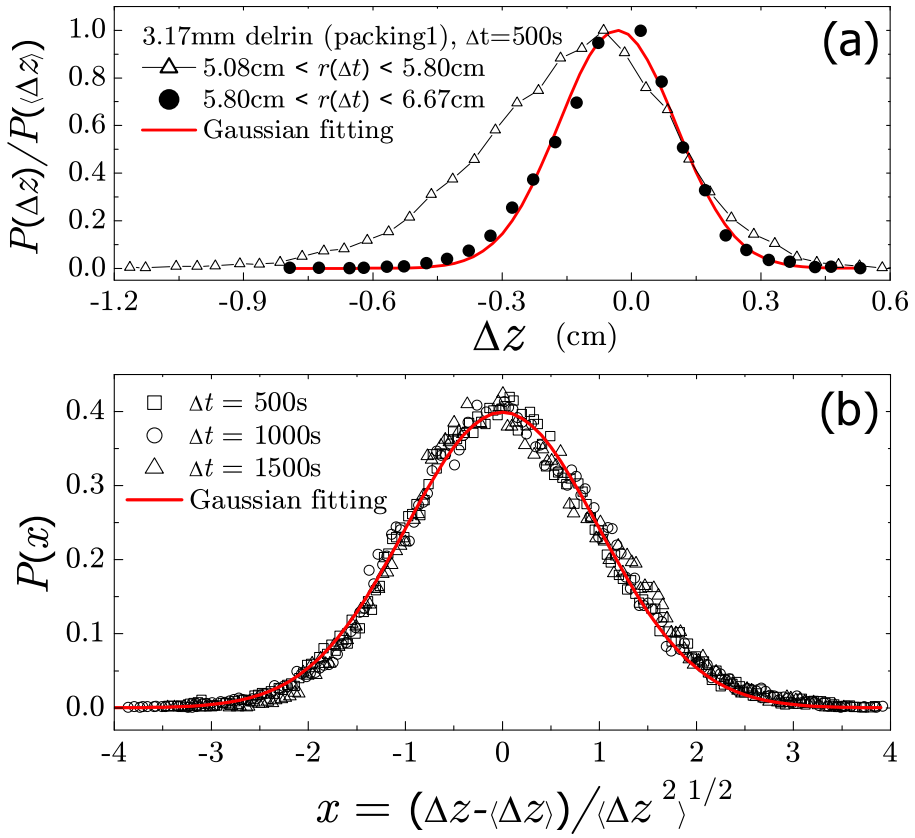

Figure 2.5: (a) PDF of the vertical displacements, $P(\Delta z)$, of the 3.17mm delrin tracers in Packing 1 for a given time interval $\Delta t = 50$s, and with $\dot{\gamma}_e = 0.048\text{s}^{-1}$. Tracer trajectories are split into sub-trajectories confined in two regions, (i): 5.08cm $< r <$ 5.80cm, which is close to inner rotating cylinder, and (ii): 5.80cm $< r <$ 6.67cm, which is far away from inner rotation cylinder. The calculated $P(\Delta z)$ are compared by using the sub-trajectories from the regions of (i) and (ii) respectively, which are plotted as black triangle and black circle. See more details in the main text. (b) PDF of the vertical displacements, $P(\Delta z)$, of the 3.97mm nylon tracers in Packing 1 with $\dot{\gamma}_e = 0.048\text{s}^{-1}$, shifted by the average displacement $\langle \Delta z \rangle$ and scaled by the root-mean-square deviation $\langle \Delta z(t)^2 \rangle^{1/2}$. The red solid curve is a Gaussian distribution, $P(x) = 0.4\text{e}^{-x^2/2}$.

2.3.2 Probability Distribution of Displacements

Fig. 2.5a shows the results of the probability distribution of the displacements Δz in the vertical direction for a given time interval Δt. The data corresponds to the 3.17mm delrin tracers in Packing 1. Usually, 20 tracers are used for calculations. Tracer trajectories are split into sub-trajectories confined in two regions, (i): 5.08cm $< r <$ 5.80cm, close to the inner rotating cylinder, and (ii): 5.80cm $< r <$ 6.67cm, i.e., CMD region, close to the outer cylinder. The calculated $P(\Delta z)$ are compared by using the sub-trajectories from the regions of (i) and (ii) respectively, which are plotted as black triangle and black circle in the Fig. 2.5a. The data in the inner region (i) clearly display an asymmetric tail for $\Delta z < 0$. This extra spreading is similar to the phenomena of the Taylor dispersion [23].

For the region (ii) of Fig. 2.3b , the CMD region, the gradient of the flow, i.e., the shear rate is approximately constant, giving rise to a Gaussian diffusion, as shown in Fig. 2.5a. By measuring the width and the mean value of this Gaussian distribution of

$$\begin{aligned} P(\Delta z) &\sim \exp[-\frac{(\Delta z - \langle \Delta z \rangle)^2}{2\langle \Delta z^2 \rangle}] \\ &\sim \exp[-\frac{(\Delta z - M_z F \Delta t)^2}{4 D_z \Delta t}], \end{aligned} \tag{2.4}$$

the diffusivity and mobility, D_z and M_z, can be defined, leading to the effective temperature of the granular packing discussed in the following section. Fig. 2.5b imposes a new scaled variable $x = \frac{\Delta z - \langle \Delta z \rangle}{\langle \Delta z^2 \rangle^{1/2}}$ and plots $P(x)$ for different Δt, where all curves are found to collapse into a single curve.

$$P(x) \sim \mathrm{e}^{-x^2/2}. \tag{2.5}$$

In the CMD region, the mobility is a constant, shown as s plateau in the inset of Fig. 2.4, and Taylor dispersion effects are absent.

D_z is calculated by measuring the width and the mean value of the Gaussian distribution of $P(\Delta z)$, and obtain the $P(\Delta z)$ by averaging the displacement fluctuations of all tracers over all time in the CMD region. Another method reveals how $D_z(r)$ depends on the radial distance r, as shown in the Fig. 2.6. First $P(\Delta z, r)$ is obtained for a certain radial distance r, then $D_z(r)$ is calculated by measuring the width and the mean value of the Gaussian distribution of $P(\Delta z, r)$. In Fig. 2.6, the tracer particles have higher diffusivity close to the inner cylinder than the outer. Since $D_z \sim \dot{\gamma}_e$, all the $D_z(r)$ can be collapsed for various shear rates, as shown in the inset of Fig. 2.6. The collapse of $D_z(r)/\dot{\gamma}_e$ shows a plateau close to the outer cylinder, consistent with the previous discussion of the CMD region.

2.3.3 Effective Temperature

Results for the diffusivity are presented in the z direction, the only direction where the effective temperature can be calculated due to the vertically acting external force. The Gaussian distribution in $P(\Delta z)$ allows us to apply the FD relation to the particle displacements, as the diffusivity is proportional to the variance of a Gaussian distribution in displacements.

A common method of performing a time average to measure transport coefficients is employed (see Chapter 5.3 in [25]) by dividing the trajectory of a single

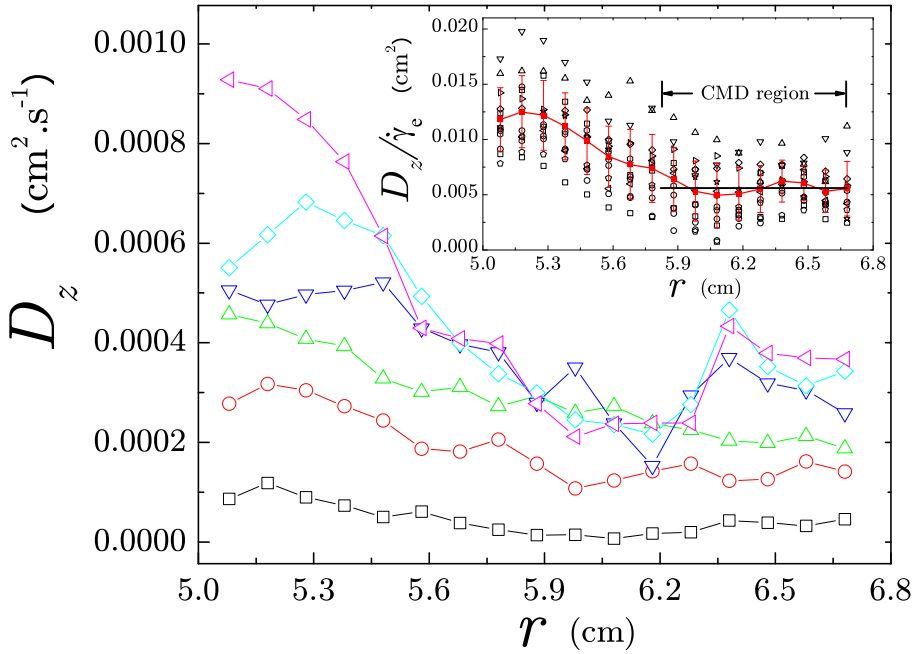

Figure 2.6: Diffusivity D_z versus radial distance r for various shear rate $\dot{\gamma}_e$ in Packing 2. Black square, red circle, green triangle, blue triangle-down, cyan diamond, magenta triangle-left are corresponding to $\dot{\gamma}_e = 0.008, 0.016, 0.032, 0.048, 0.060, 0.084\text{s}^{-1}$, respectively. The inset plots the collapsing of diffusivity scaled by shear rate, $D_z/\dot{\gamma}_e$, versus radial distance r for various shear rate $\dot{\gamma}_e$. The red solid curve is the average result of the collapsing.

Packing 1, 1:1 mass mixture of 3.17mm & 3.97mm acrylic beads, $\dot{\gamma}_e = 0.048\text{s}^{-1}$					
tracer	d (mm)	ρ (g·cm^{-3})	D_z (10^{-8} m^2·s^{-1})	M_z (10^{-2} s·kg^{-1})	T_{eff} (10^{-7} J)
acrylic	3.17	1.19	2.5 ± 0.3		
delrin	3.17	1.36	2.4 ± 0.3	24 ± 3	1.0 ± 0.2
delrin	3.97	1.36	1.2 ± 0.1	9.3 ± 0.9	1.3 ± 0.2
nylon	3.97	1.12	1.1 ± 0.1	9.5 ± 0.9	1.2 ± 0.2
ceramic	3.97	3.28		2.2 ± 0.2	
brass	3.97	8.4		1.7 ± 0.1	
Packing 2, 1:1 mass mixture of 3.97mm & 4.76mm acrylic beads, $\dot{\gamma}_e = 0.024\text{s}^{-1}$					
tracer	d (mm)	ρ (g·cm^{-3})	D_z (10^{-8} m^2·s^{-1})	M_z (10^{-2} s·kg^{-1})	T_{eff} (10^{-7} J)
nylon	3.97	1.12	1.8 ± 0.1	19.0 ± 0.9	0.95 ± 0.07
nylon	4.76	1.12	1.6 ± 0.1	15.7 ± 0.4	1.0 ± 0.1

Table 2.1: Diffusivity and mobility for the different types of tracer and packings.

tracer particle into a series of trajectories, having evenly spaced start times, separated by time interval Δt. The diffusion constant is obtained by averaging over the aggregate of tracers and over the initial time intervals, allowing for the use of merely 20 tracer particles in this particular system. Correlations between measurements are ensured to have decayed almost to zero, rendering time-translational invariance valid in this system, without any measurable"aging", since under shearing the system reaches the "stationary state" [26]. Furthermore, doubling the number of tracer particles leaves D_z unchanged, indicating independence of the diffusion constant from the number of tracers that explore the jammed configurations of this non-equilibrium system.

Analysis of the vertical particle displacements in the CMD region reveals a Gaussian distribution, broadening over time, as seen in Fig. 2.5. For sufficiently long times period, the mean square fluctuations grow linearly (see Fig. 2.7a):

$$\langle [z(t+\Delta t) - z(t)]^2 \rangle \sim 2D_z \Delta t, \tag{2.6}$$

where D_z is the self-diffusion constant in the vertical direction. For the both nylon and delrin 3.97mm tracers in Packing 1 $D_{z\ 3.97\text{mm}} \approx (1.15 \pm 0.1) \times 10^{-8}$ m^2/s.

Figure 2.7b shows mean value tracer particle positions, extracted from the peak of the Gaussian distribution, as a function of time. The mobility in the vertical direction, M_z, is defined as

$$\langle z(t+\Delta t) - z(t) \rangle \sim M_z F \Delta t. \tag{2.7}$$

The applied force on the tracers, $F = (\rho - \rho')Vg$, is the gravitational force due to

density mismatch where ρ and ρ' are the densities of the acrylic particles and the tracers, respectively, V is the volume of the tracer particle and g the gravitational acceleration. The value of the mobility for the both nylon and delrin 3.97mm tracers in Packing 1 is $M_{z\ 3.97\text{mm}} \approx (9.4 \pm 0.9) \times 10^{-2}$ s/kg.

Fig. 2.7a further reveals a downward curvature of the mean-square fluctuations, for sufficiently long times period. Additionally, an apparent cut-off time for the tracer particles fluctuation measurements is shown. These effects are due to the finite size effect imposed upon the tracers by the finite trajectories and should be inversely proportional to the tracer particles velocities. Tracer particles with larger mobility will have larger mean velocities and take a shorter time to complete its trajectory in the cell. The cut-off discussed in reference to Fig. 2.7a is prominently displayed in the 3.17mm delrin tracers of Packing 1, having the largest mobility, hence increased mean velocities, as shown in Fig. 2.7b. The larger mobility results in the shortest cut-off time for the diffusivity. Conversely, 3.97mm delrin tracers of Packing 1 have a smaller mobility, hence a longer cut-off time for the diffusivity. It is important to note that for all tracer particles studied here, the cut-off is observed for distances larger than a few particles diameters, ensuring that the study examines the structural motion of the grains and not internal motion inside of "cages".

According to a Fluctuation-Dissipation relation:

$$T_{\text{eff}} = \frac{F\langle[z(t+\Delta t) - z(t)]^2\rangle}{2\langle z(t+\Delta t) - z(t)\rangle}. \tag{2.8}$$

Fig. 2.7c shows a parametric plot of fluctuations and responses, with Δt, as the parameter, as extracted from Fig. 2.7a and Fig. 2.7b. A linear relationship

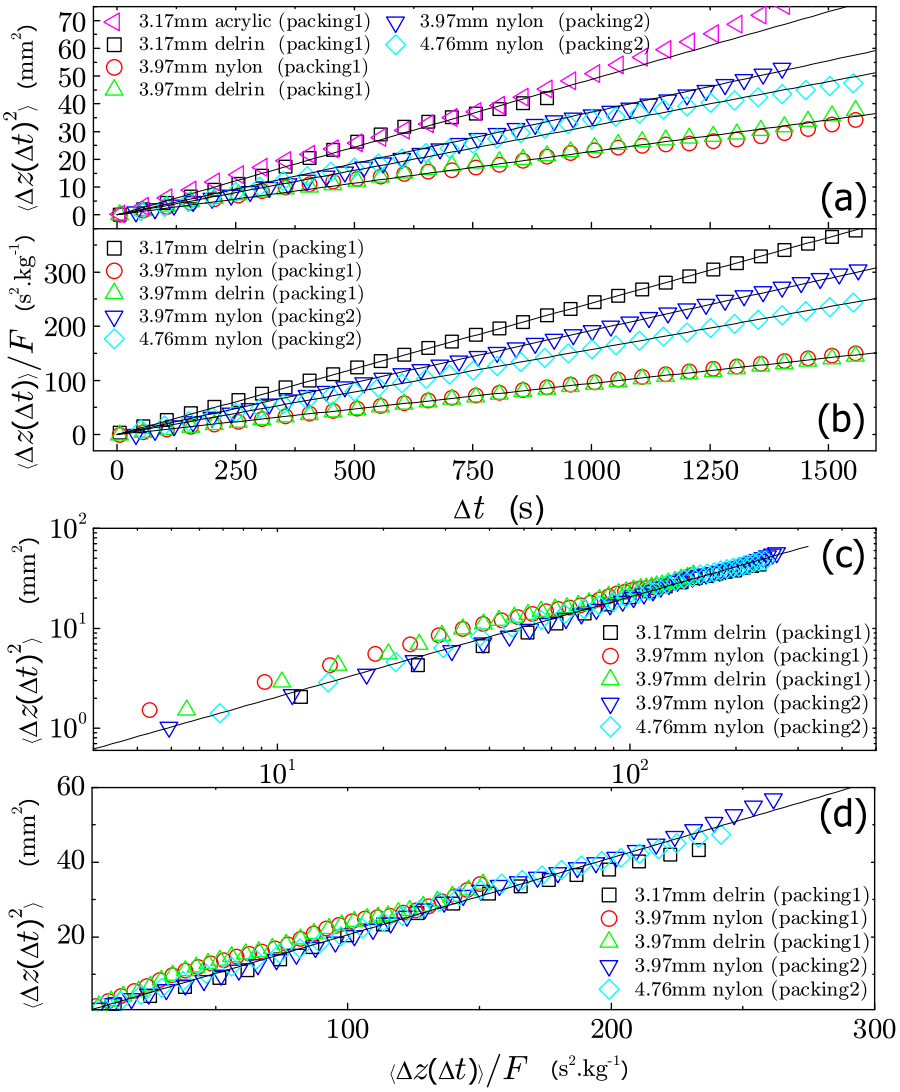

Figure 2.7: (a) Autocorrelation function of tracers. (b) Response function of tracers. (c) Log-log plot of effective temperatures for various tracers and different packings as obtained from a parametric plot of their autocorrelation function versus response function. (d) Same as (c) but in a linear-linear plot. The slopes for different tracer diffusivity vs. mobility curves return the same average value of $T_{\text{eff}} \approx (1.1 \pm 0.2) \times 10^{-7}$J as given by Eq. (2.3).

exists between diffusivity and mobility, with a slope of T_{eff}. For the both nylon and delrin 3.97mm tracers in Packing 1, $T_{\text{eff}} \approx (1.25 \pm 0.2) \times 10^{-7}$J.

If the effective temperature is to be regarded as an intensive thermodynamic quantity, changing the tracer particle size should give rise to a different diffusion and mobility yet result in the same measurement of effective temperature. The above calculation is repeated for delrin tracers of 3.17mm in Packing 1. While the mobility and diffusivity change dramatically with respect to tracers of 3.97mm, ($D_{z\ 3.17\text{mm}} = (2.4 \pm 0.3) \times 10^{-8}$ m^2/s and $M_{z\ 3.17\text{mm}} = (2.4 \pm 0.3) \times 10^{-1}$ s/kg) as shown in Table 2.1, due to the change in tracer size, their ratio remains unchanged. In all cases D_z and M_z are inversely proportional to the size of the tracers, but the effective temperature remains approximately the same, as seen in Fig. 2.7c, with an average value over all tracers of

$$T_{\text{eff}} \approx (1.1 \pm 0.2) \times 10^{-7}\text{J}. \tag{2.9}$$

Though this effective temperature is high with respect to the bath temperature, note that a plausible scale for the system energy [10], is $(\rho - \rho')gd$, the gravitational potential energy to move a nylon tracer particle one particle diameter, d. A corresponding temperature would arise from the conversion of this energy into a temperature via the Boltzmann constant, k_B, is $T_{\text{eff}} = 2.7 \times 10^{13} k_B T$ at room temperature (T = 300K). This specific value serves as a coarse-grained estimate, since the tracer size and density clearly shift its value, and focus on the order of magnitude. This large value is expected [10], and agrees with computer simulation estimates for an athermal granular system [8]. Therefore, the calculated value for T_{eff} in a sheared granular system appears reasonable within the boundaries of the

present theory.

2.3.4 Shear Rate Dependence

In Fig. 2.8 the effective temperature seems to become approximately constant, as long as the particulate motion is slow enough such that the system is very close to jamming. Within a quasi-static range, D_z and M_z are both proportional to $\dot{\gamma}_e$, while $T_{\text{eff}} = D_z/M_z$ remains approximately constant for sufficiently small $\dot{\gamma}_e$.

It is within this quasi-static range where the effective temperature could be identified with exploration of the jammed configurations. As it remains an important assumption of this study that the system is being continuously jammed, shear rates high enough to impact the effective temperature measurement imply systems that are not continuously exploring jammed configurations. Studying the nature of the jammed granular packings, it is logical to presume that quasi-static shearing will provide systems of interest. The limit of T_{eff} as $\dot{\gamma}_e \to 0$ may result in an effective temperature for the static jammed configuration. The quasi-static shear rate regime observed could be analogous to the shear-rate independent regime observed in the behavior of shear stress in slowly sheared granular materials [27, 28]. This solid friction-like behavior has been previously studied [27, 28] and occurs when frictional forces and enduring contacts dominate the dynamics. This regime has been also observed in recent computer simulations of the effective temperature of sheared granular materials [7, 29]. The calculations of T_{eff} for systems close to jamming exclude the systems outside of the quasi-static range, in accordance with prior studies.

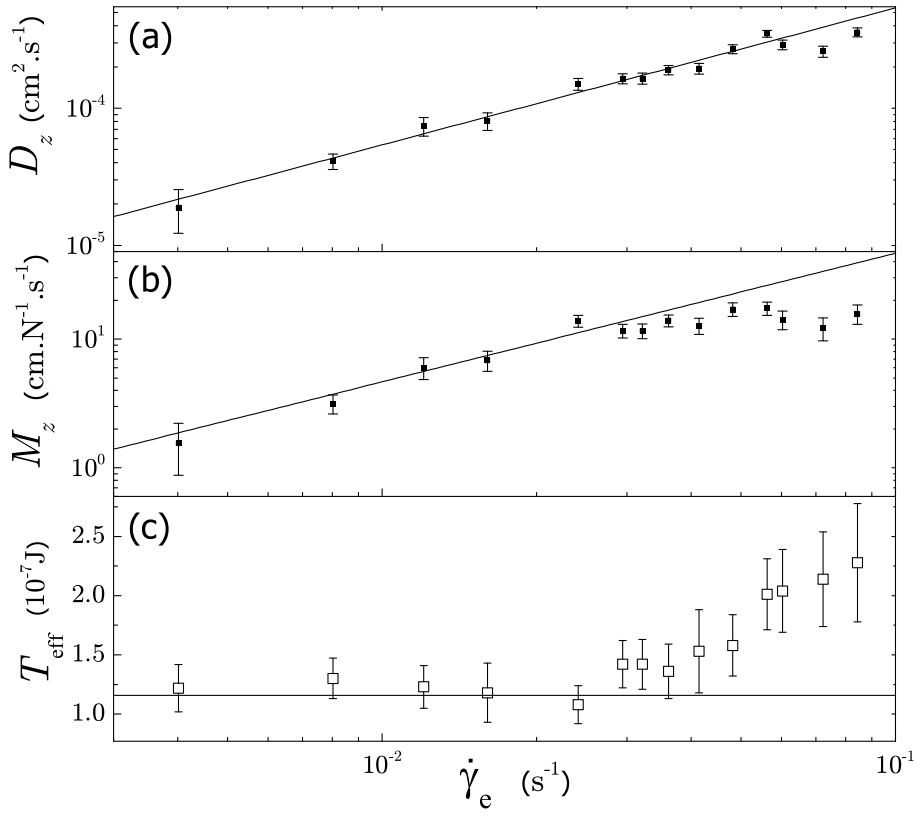

Figure 2.8: The dependence of (a) diffusivity D_z, (b) mobility M_z and (c) effective temperature T_{eff} on the shear rate $\dot{\gamma}_e$ for the 4.76mm nylon tracers in Packing 2. The solid lines in (a) and (b) are linear fitting [note that the line in (b) is a fitting only for the first 6 data points at the small value of shear rate $\dot{\gamma}_e$]. $D_z \sim \dot{\gamma}_e$ and $M_z \sim \dot{\gamma}_e$, while $T_{\text{eff}} = D_z/M_z$ is approximately constant for sufficiently small $\dot{\gamma}_e$. This quasi-static regime coincides with the appearance of a rate-independent stress in experiments [28], that T_{eff} is interpreted as the temperature of the jammed states. The height of flat solid line in (c) is calculated from the slope of lines in (a) and (b), which indicates a constant effective temperature $T_{\text{eff}} = (1.2 \pm 0.2) \times 10^{-7}$J at the small value of shear rate $\dot{\gamma}_e$.

2.4 Significance Of T_{eff} for a Statistical Mechanics of Grains

In contrast to measurements of slow mode temperatures, exemplified by T_{eff}, the temperature of the fast modes is given by the root mean square (RMS) fluctuations of the velocity of the particles. It should be noted that these velocities are not instantaneous, as the time necessary to obtain an instantaneous velocity is much smaller than the time between measurements. Nevertheless, an estimate of the kinetic granular temperature can be obtained, T_k, from $T_k = \frac{2}{3}E_k$, where $E_k = \frac{1}{2}m\overline{v^2}$ with $\overline{v^2}$ the average kinetic energy of the grains. $T_k = 9.17 \times 10^{10} k_B T$, or $3.77 \times 10^{-10} J$ and $T_k = 1.54 \times 10^{11} k_B T$, or $6.34 \times 10^{-10} J$, for 3.17 mm and 3.97 mm delrin tracers in packing 1, respectively. Here, $T = 298.15K$, the room temperature, and $k_B = 1.3806504 \times 10^{-23} JK^{-1}$. This kinetic granular temperature is smaller than T_{eff} and differs for each type of tracer indicating that it is not governed by the same statistics. Similar results have been obtained in experiments of vibrated granular gases [30]. The significance of this result is that fast modes of relaxation are governed by a different temperature. This result is analogous to what is found in models of glasses and computer simulations of molecular glasses (see for instance Refs. [2, 31, 32, 26, 33]). In the glassy phase of these models, the bath temperature is found to control the fast modes of relaxation and a different, larger, effective temperature is found to control the slow modes of relaxation. Similarly, a granular bath temperature exists for fast modes of relaxation and a larger effective temperature for slow modes of relaxation.

It is possible to identify T_{eff} as the property of the system governing the ex-

ploration of jammed configurations. As this particular non-equilibrium system remains athermal, the 'bath' temperature in which the grains exist is immaterial, as shown above. Particle diffusion is of the order of several particle diameters over the time scale of the experiment (see Fig. 2.2 and 2.7a) implying that exploration of the available jammed configurations occurs via rearrangements of the particles outside their "cages", suggesting that the trajectory of the system can be mapped onto successive jammed configurations explored by the system.

Incorporating certain experimental conditions of reversibility, and ergodicity, a statistical mechanics formulation may well describe a jammed granular system [9, 34]. Under the primary assumption that different jammed configurations are taken to have equal statistical weight, observables can be calculated by "flat" averages over the jammed configurational space [9, 35, 4, 36, 8, 37, 38]. This assumption, advocated by Edwards and collaborators, has been thoroughly debated in the literature (see for instance [26, 39]). Existing work suggests the effective temperature obtained by applying a fluctuation-dissipation theory to non-equilibrium systems is analogous to performing a "flat" average over the jammed configurational space, at least for frictionless systems [8]. Additionally, the effective temperature can be identified with the compactivity introduced in [9], resulting from entropic calculations of the granular packing [35, 4, 8]. Experimentally testing these ideas is difficult as the entropy of the jammed configurations is not easily measured, and it is not possible to obtain the compactivity from entropic considerations in the present study.

The exploration of reversible jammed states in granular matter bears similarity to that of inherent structures in glasses. Inherent structures form a network of

attractive basins within an energy landscape, and the system explores these basins as governed by their stability over the slow-relaxation time of the glass. It should be noted, however, that there exists a crucial difference between glasses and grains. In liquids energy remains conserved, while energy is dissipated in granular systems through frictional contact and path dependent forces between grains. Thus, a driven granular system will quickly come to a mechanically stable, or jammed, state after the removal of the driving forces. By its nature, energy is not conserved in a granular system. As energy conservation is the crucial property used to define an energy ensemble in statistical mechanics, the use of energy to characterize granular systems is questionable. Thus, while T_{eff} seems to imply the exploration of reversible jammed states within an energy ensemble, with

$$P(E) \sim \mathrm{e}^{-\frac{E}{T_{\text{eff}}}} \tag{2.10}$$

describing the nature of the exploration, the validity of the energy ensemble to describe granular matter in the absence of energy conservation remains an open question. Here, the analogous Boltzmann constant for grains equal to unity for simplicity.

Noting the drastic difference between the bath temperature and the effective temperature in a granular system, a more careful analysis of the energy ensemble in slowly driven granular systems is inspired. The work of Edwards has promoted the concept of a volume ensemble, where the free volume per grain in a static granular system replaces the energy as the conserved quantity of the non-equilibrium system, at a particular volume fraction [9, 34]. The basis for using the volume ensemble stems from the ability to conserve volume in a given packing and additivity

of volume per grain. Further, it is possible to explore the configuration of states at a fixed volume, via experiment or simulation. The statistical mechanics is then derived using methods similar to Boltzmann statistics for equilibrium systems. From these methods, one can obtain the compactivity, X, as a derivative of the entropy with respect to the volume, enabling the calculation of an equation of state. The compactivity, X, is thereby assumed to be an equilibrium measure of a system within the framework of the volume ensemble, much like the bath temperature of the energy ensemble. This assumption can be realized by performing an ABC experiment and testing a zero-th law of thermodynamics for volumes [39]. This experiment is feasible due to the fact that it is always possible to prepare a system at a given volume fraction and will be the subject of future study and experiment, facilitated by recent theoretical findings [40].

However, slowly driven granular systems introduce yet another ensemble, the energy ensemble, from which the above defined T_{eff} is derived. While the above results reveal that T_{eff} does not tend to zero as the magnitude of the driving force decreases, indicating extrapolation to a non-zero static quantity, it remains unclear how the effective temperature may relate to the compactivity as defined by Edwards statistics. Is a new static quantity defined by determining the static limit of T_{eff}, or does it merely expand the statistical mechanics of jammed granular matter to include dynamic systems by relating T_{eff} and X? T_{eff} is obtained in the quasi-static limit $\dot{\gamma}_e \to 0^+$, while the volume and force ensembles correspond to $\dot{\gamma}_e = 0$, exactly. Is it possible that a relation between T_{eff} and X can be expected?

There exists the further requirement of energy conservation for the validity of a Boltzmann approach that would guarantee:

$$T_{\text{eff}}^{-1} = \frac{\partial S}{\partial E} \tag{2.11}$$

As discussed above, energy is constantly dissipated in a driven granular system, through Coulomb friction and path-dependent tangential forces between grains. However, the input of energy by the external driving force brings the system to a steady state where the average energy is constant over the time-scale of the experiment. This steady state energy could be likened to the conserved variable in a statistical formalism depicted in Eq. 2.11, thereby introducing a thermodynamic meaning for T_{eff}.

2.5 Summary

In summary, this study focuses on the dynamics of slowly sheared granular matter in a 3D Couette cell. A mixture of spherical, transparent and bi-disperse grains are confined between two cylinders, having walls roughened by glued identical grains, with the inner cylinder rotated via motor. The grains are compacted by means of an external pressure in the negative z-direction. Fluid matching the density and refractive index of the grains partially fills the cell, allowing tracking of tracer particle trajectories as a function of time. Tracers of varying density and size are used. Multiple cameras track the tracer particle positions relative to the cylinders.

An "effective temperature", T_{eff}, is realized by a fluctuation-dissipation relation generalized to granular materials. Statistical measurements are confined exclusively to the CMD region. The mobility in the vertical direction, M_z, is found to be proportional to the shear rate, $\dot{\gamma}_e$, for small enough values of $\dot{\gamma}_e$. As D_z is

also found proportional to shear rate, collapsing all the $D_z(r)$ for various shear rates shows a plateau in the CMD region. An approximately constant effective temperature is obtained from measurements of the mobility and diffusivity, under a constant external applied force, and with sufficiently small shear rates. This effective temperature is calculated by an analogous equation used in equilibrium statistical mechanics and is found to be independent of the tracer particle properties, dependent only on the packing density of the system.

While this result describes an intensive property of the system, it remains an important future study to test the effective temperature against the laws of thermodynamics. More specifically, a test of the zeroth-law of thermodynamics with respect to these non-equilibrium jammed systems could expand the scope of T_{eff} beyond that of an intensive quantity of a particular system. The nearly constant value of T_{eff} with respect to varying tracer particle size indicates that a zero-th law of thermodynamics for slowly sheared jammed granular systems could be valid and prompts one to perform an ABC experiment, fully testing the zero-th law for the effective temperature. A well defined effective temperature in the radial direction may exist, though its existence would require a constant external force applied in the radial direction.

It is important to note that the effective temperature, defined in this study for small shear rates, does not remain constant as the shear rate increases. While previous studies have discovered an increasing effective temperature via simulations, diffusivity and mobility are measured separately in an effort to calculate T_{eff} through a fluctuation-dissipation relation. The diffusivity in the z-direction remains approximately constant throughout the range of shear rates used in this

experiment, while the mobility in the z-direction approaches a plateau. exclusively increasing T_{eff}.

A more complete description of the statistical mechanics of jammed granular matter strives to incorporate the varied statistical ensembles into one fundamental picture. These ensembles include the energy ensemble, as described herein, along with the volume and force ensembles, as proposed by Edwards. Such an incorporation may link static quantities of compacitivity and angoricity, describing volume and force ensembles, respectively, to the dynamic effective temperature presented in this study, derived from the energy ensemble. The exact nature of the relation between such quantities remains an open topic. The following chapters will focus on the volume ensemble, and characterize compactivity in jammed granular matter.

Chapter 3

Statistical Mechanics of Jammed Matter

3.1 Introduction

A large body of experiments, theory and simulations have focused on the study of volume fluctuations in granular media [26, 41]. Statistical studies have been concerned with testing for the existence of thermodynamics quantities such as effective temperatures and compactivity as well as challenging the foundations based on the ergodic hypothesis or equal probability of the jammed states.

Unfortunately, there is no first principle derivation of the granular statistical mechanics analogous to the Liouville theorem for equilibrium systems [1]. Therefore, advancing the statistical mechanics of granular matter requires well-defined theoretical predictions that can be tested experimentally or numerically. While the possibility of a thermodynamic principle describing jammed matter is recognized

as a sensible line of research, the problem with the statistical approach is that after almost 20 years there are no practical applications yet, such as predictions of equations of state relating the observables: pressure, volume, coordination number, entropy, etc, that may lead to new phenomena to be discovered and tested experimentally that will allow for a concrete exploitation of the thermodynamic framework.

Here, a systematic study of the V-F ensemble of jammed matter is developed. Systems of interest are primarily packings of granular materials, frictional colloids, infinitely rough grains and frictionless droplets mimicking concentrated emulsions.

3.1.1 Sphere packing problem

Filling containers with balls is one of the oldest mathematical puzzles known to scientists. The study of this problem started four centuries ago when Johannes Kepler conjectured that the most efficient arrangement of spheres is the FCC lattice (an important part of the 18th problem proposed by Hilbert in 1900). Even though this is a tool used for centuries in fruit markets around the globe, nearly 400 years passed before this conjecture was considered a mathematical proof, which has been developed only recently by Hales [42] in a series of articles covering 250 pages supplemented by 3Gb of computer code to determine the best ordered packing through linear programming. The difficulty arises since in 3d it is not enough to look at the packing of one cell, but it is necessary to consider several Voronoi cells at once. That is, the packing that minimize the volume locally (the dodecahedron) does not tile the system globally. Such a situation does not arise in 2d, where the hexagonal packing minimizes the volume locally and globally; the

Kepler conjecture in 2d was proved long ago.

The analogous problem for disordered packings has also an illustrious but unfinished history. This problem was initiated by the pioneering work of Bernal in the 1960's [43] (although earlier attempts can be found). The traditional view states that [44] "packings of spherical particles have been shaken, settled in different fluids and kneaded inside rubber balloons and all with no better results than a maximum density of 63%". This is the so-called random close packing RCP limit [43, 44, 45, 46, 47]. On the other hand, other experiments have shown that densities as low as 55% can be obtained in random loose packings, RLP [45, 47, 48]. To this date there is no physical explanation of this phenomenon, no theoretical prediction of such density values and heated debates are still found in the literature regarding the existence of rigorous definitions of the RCP and RLP, the uniqueness of the RCP state and the nature of their state of randomness.

3.2 Statistical mechanics of jammed matter

Edwards statistical mechanics is applied to study random disordered systems and the systems are treated at the ensemble level.

Conventional Statistical Mechanics uses the ergodic hypothesis to derive the microcanonical and canonical ensembles, based on the quantities conserved, typically the energy E [1]. Thus the entropy in the microcanonical ensemble is $S(E) = k_B \log \int \delta(E - \mathcal{H}(p,q))dpdq$, where $\mathcal{H}(p,q)$ is the Hamiltonian. This becomes the canonical ensemble with $\exp[-\mathcal{H}(\partial S/\partial E)]$.

The analogous development of a statistical mechanics of granular and other

jammed materials presents many difficulties. First, the macroscopic size of the constitutive particles forbids the equilibrium thermalization of the system. Second, the fact that energy is constantly dissipated via frictional interparticle forces further renders the problem outside the realm of equilibrium statistical mechanics due to the lack of energy conservation. In the absence of energy conservation laws, a new ensemble is needed in order to describe the system properties.

Following this theoretical perspective, Edwards proposed the statistical mechanics of jammed matter and interest in the problem of volume fluctuations has flourished [9]. The central concept is that of a volume function $\mathcal{W}$ replacing the role of the Hamiltonian in describing the microstates of the system in the V-ensemble and the stress boundary $\Pi_{ij} = \int \sigma_{ij} dV$ with the stress $\sigma_{ij} = 1/(2V) \sum_c f_i^c r_j^c$ describing the F-ensemble [51, 49, 50], where f_i^c, r_i^c are the force and position at contact c. For simplicity only the isotropic case is described. Thus, only the pressure $\sigma = \sigma_{ii}/3$ is necessary to describe force fluctuations.

If the space associating each particle is partitioned by its surrounding volume, $\mathcal{W}_i$ (for instance with a Voronoi tessellation as it will be done bellow), then the total volume, $\mathcal{W}$, of a system of N particles is given by:

$$\mathcal{W} = \sum_{i=1}^{N} \mathcal{W}_i. \tag{3.1}$$

The ensemble average of the volume function $\mathcal{W}$ provides the volume of the system, $V = \langle \mathcal{W} \rangle$, in an analogous way to the average of the Hamiltonian is the energy in the canonical ensemble of equilibrium statistical mechanics.

The full canonical partition function in the V-F ensemble is the starting point

of the statistical analysis [51]:

$$\mathcal{Q}(X,A) = \int g(\mathcal{W},\Pi)\ \exp\Big[-\frac{\Pi}{A}-\frac{\mathcal{W}}{X}\Big]\ \Theta_{\rm jam}\ d\mathcal{W}\ d\Pi, \tag{3.2}$$

where $g(\mathcal{W},\Pi)$ is the density of states for a given volume and boundary stress. Here $\Theta_{\rm jam}$ formally imposes the jamming restriction and therefore defines the ensemble of jammed matter. This crucial function will be discussed at length below. As a minimum requirement it should ensure touching grains, and obedience to Newton's force laws.

Just as $\partial E/\partial S = T$ is the temperature in equilibrium systems, the temperature-like variables in granular systems are the compactivity [9]:

$$X = \frac{\partial V}{\partial S}, \tag{3.3}$$

and the angoricity [from the Greek "$\acute{\alpha}\gamma\chi o\zeta$" (ankhos) = stress] [51]:

$$A = \frac{\partial \Pi}{\partial S}. \tag{3.4}$$

In the limit of vanishing angoricity, $A \to 0$, the system is described by the V-ensemble alone. This is the hard sphere limit with the following partition function:

$$\mathcal{Q}_{\rm sph}^{\rm hard}(X) = \int g(\mathcal{W})\ e^{-\mathcal{W}/X}\ \Theta_{\rm jam}\ d\mathcal{W}, \tag{3.5}$$

where $g(\mathcal{W})$ is the density of states for a given volume $\mathcal{W}$.

From Eq. (3.5) three steps in developing analytical solutions are discussed below. Section **3.3** discusses the need for a volume function, $\mathcal{W}$. Section **3.4**

discusses the need for a proper definition of the ensemble of jammed state allowing a definition of the constraint function Θ_{jam}. Section **3.5** discusses the derivation of the density of states.

3.3 Volume Function

While it is always possible to measure the total volume of the system, it is unclear how to treat the volume fluctuations at the grain level. The first step to study the V-ensemble is to find the volume function $\mathcal{W}_i$ associated to each particle that successfully tiles the system. This is analogous to the additive property of energy in equilibrium statistical mechanics.

Initial attempts at modelling $\mathcal{W}$ included, (a) a model volume function under mean-field approximation [9], (b) the work of Ball and Blumenfeld [52, 53] in 2d and in 3d [54], and (c) simpler versions in terms of the first coordination shell by Edwards [39]. These definitions are problematic: (a) is not given in terms of the contact network, (c) is not additive, (b) and (c) are proportional to the coordination number of the balls contrary to expectation. In [40] an analytical form of the volume function in any dimension is found and is demonstrated to be the Voronoi volume of the particle.

The definition of a Voronoi cell is a convex polygon whose interior consists of all points closer to a given particle than to any other (see Fig. 3.1). Its formula in terms of particle positions for monodisperse spherical packings in 3d is [40]:

$$\mathcal{W}_i^{\text{vor}} = \frac{1}{3}\left\langle \left(\frac{1}{2R} \min_j \frac{r_{ij}}{\cos\theta_{ij}} \right)^3 \right\rangle_s \equiv \langle \mathcal{W}_i^s \rangle_s, \tag{3.6}$$

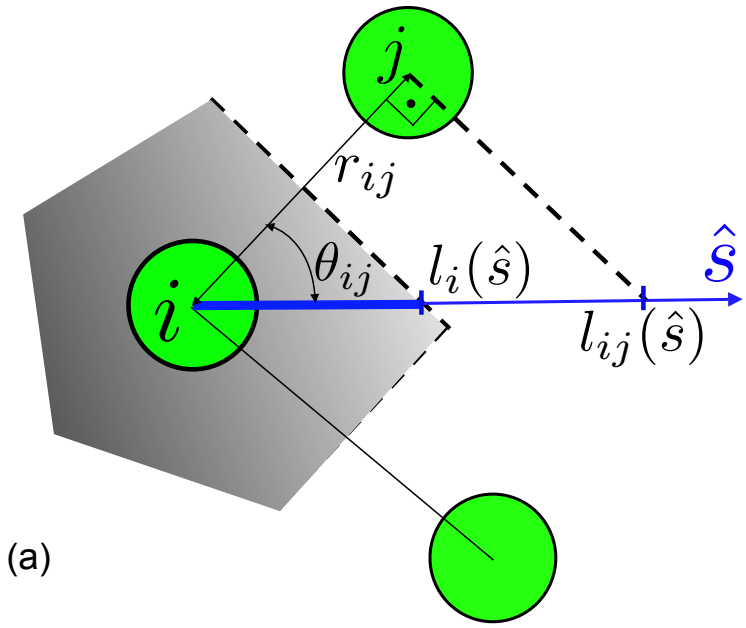

Figure 3.1: The Voronoi volume is the light grey area (shown in 2d for simplicity). The limit of the Voronoi cell of particle i in the direction s is $l_i(s) = r_{ij}/2\cos\theta_{ij}$. Then the Voronoi volume is proportional to the integration of $l_i(\hat{s})^3$ over s.

where $v(r_{ij})$ is the vector from the position of particle i to that of particle j, the average is over all the directions s forming an angle θ_{ij} with $v(r_{ij})$ as in Fig. 3.1, and R is the radius of the grain. $\mathcal{W}_i^s$ defines the orientational Voronoi volume which is obtained without the integration over s. While this formula may seem complicated, it has a simple interpretation depicted in Fig. 3.1.

The Voronoi construction is additive and successfully tiles the total volume. Prior to Eq. (3.6), there was no analytical formula to calculate the Voronoi volume in terms of the contact network r_{ij}. Equation (3.6) provides such a formula which allows theoretical analysis in the V-ensemble. However this microscopic version is difficult to incorporate into the partition function since it would necessitate a field theory. The next step is to develop a theory of volume fluctuations to coarse grain $\mathcal{W}_i^{vor}$ over a mesoscopic length scale and calculate an average volume function. The coarsening reduces the degrees of freedom to one variable, the coordination number of each grain, and defines a mesoscopic volume function [40]which is more amenable to statistical calculations than Eq. (3.6).

$$w(z) \equiv \frac{\langle \mathcal{W}_i^s \rangle_i - V_g}{V_g} = \frac{2\sqrt{3}}{z}, \tag{3.7}$$

valid for monodisperse hard spheres with volume V_g, where z is the geometrical coordination number (which is different from the mechanical coordination number, Z, see below). The average is over all the grains.

The inverse relation with z in Eq. (3.7) is in general agreement with experiments [55]. Many experiments have focused on the analysis of the system volume and single particle volume fluctuations in granular media [52, 56, 55, 57, 58, 20].

Of particular importance to the present theory are advances in X-ray tomography [55] and confocal microscopy [59] which have revealed the detailed internal structure of jammed matter allowing for the study of the free volume per particle. By partitioning the space with Voronoi diagrams, these studies show that $\mathcal{W}_i^{vor}$ is distributed with exponential tails [58, 55, 57, 60]. More importantly, the X-ray tomography experiments with 300,000 monodisperse hard spheres [55] find that the Voronoi volumes are inversely proportional, on average, to the coordination number of the particle, z, in reasonable agreement with the prediction of the volume function Eq. (3.7).

From Eq. (3.7)

$$\phi_i = \frac{1}{w+1} = \frac{z}{z+2\sqrt{3}}, \tag{3.8}$$

which agrees relatively well with the shape of the curves displayed in [55] for different packing preparations. It should be noted that for a more precise comparison a coarse grained volume fraction and geometrical coordination number should be considered in Eq. (3.8).

The free volume function decreases with z as expected since the more contacts per grain, the more jammed the particle is and the smaller the free volume associated with the grain. The coordination number z in Eq. (3.7) can be considered as a coarse-grained average associated with "quasiparticles" with mesoscopic free volume w. By analogy to the theory of quantum energy spectra, each state described by Eq. (3.7) is regarded as an assembly of "elementary excitations" which behave as independent quasiparticles. As a grain is jammed in the packing, it interacts with other grains. The role of this interaction between grains is assumed in the calculation of the volume function (3.7) and it is implicit in the

coarse-graining procedure explained above. The quasiparticles can be considered as particles in a self-consistent field of surrounding jammed matter. In the presence of this field, the volume of the quasiparticles depends on the surrounding particles as expressed in Eq. (3.6). The assembly of quasiparticles can be regarded as a set of non-interacting particles, when the number of elementary excitations is sufficiently low, and a single particle approximation can be used to solve the partition function formulated in Section 3.6.

While Eq. (3.6) is difficult to treat analytically, since it requires a field theory, the advantage of the mesoscopic Eq. (3.7) is that the partition function can be solved analytically since w depends on z only, instead of r_{ij}. The key result is the relation between the Voronoi volume and the coordination number which allow us to incorporate the volume function into a statistical mechanics approach of jammed hard spheres, by using the constraint of mechanical stability shown below.

3.4 Definition of jamming: isostatic conjecture

The definition of the constraint function Θ_{jam} is intimately related to the proper definition of a jammed state and should contain the minimum requirement of mechanical equilibrium.

Distinguishing between metastable and mechanically stable packings that define the jammed state through the Θ_{jam} function remains a problem under debate, related to the more fundamental question of whether or not a jammed packing is well-defined [61]. In practice, it is widely believed that the isostatic condition is necessary for a jammed disordered packing [62, 63, 64, 65, 66] following the

Alexander conjecture [67]. It is well known that mechanical equilibrium imposes an average coordination number larger or equal than a minimum coordination where the number of force variables equals the number of force and torque balance equations [67, 62].

It is important to note that the derivation of the volume function in Section 3.3 implies nothing about the value of the contact forces; the volume function represents the contribution arising purely from the geometry of the packing. Thus, the coordination number z appearing in Eq. (3.7) is the *geometrical* coordination number related to volume, which is different from the *mechanical* coordination number Z that counts the number of contacts per particle with non-zero force related to the isostatic condition and force network.

In the case of frictionless spherical particles in 3d the isostatic condition is $Z = 2d = 6$, while in the case of infinitely rough particles, having interparticle friction coefficient $\mu \to \infty$, the isostatic condition is $Z = d + 1 = 4$. Numerical simulations and theoretical work suggest that at the jamming transition the system becomes exactly isostatic [64, 68, 63, 69, 62, 66]. But no rigorous proof of this statement exists. In the following, this isostatic conjecture defines the ensemble of jammed matter.

While isostaticity holds for perfectly smooth and infinitely rough grains, the main problem is to extend it to finite frictional systems. For finite friction, the Coulomb condition takes the form of an inequality between the normal interparticle contact force F_n and the tangential one F_t: $F_t \leq \mu F_n$ and therefore no trivial solution to the minimum number of contacts can be obtained.

The problem can be understood as an optimization of an outcome based on a set

of constraints, i.e., minimizing a Hamiltonian of a system over a convex polyhedron specified by linear and non-negativity constraints. The isostatic condition can be augmented to indicate the number of extra equations for contacts satisfying the Coulomb condition, analogous to the number of redundant constraints in Maxwell constraint counting of rigidity percolation. This suggests that, for a finite value of μ, the original nonlinear problem can be mapped to a linear equation problem if the number of extra equations to be added is known.

Consider a set of spherical particles interacting via normal and tangential contact forces. These can be the standard Hertz and Mindlin/Coulomb forces of contact mechanics [70, 71, 72], respectively, addressed in greater detail in section 3.7.1. Set N: number of particles, N_n: number of unknown normal forces, N_t: number of unknown tangential forces, E_f: number of force balance equations, E_t: number of torque balance equations, $Z = 2M/N$: average coordination number of the packing, where M is the total number of contacts, $f_1(\mu)$: undetermined function of the friction coefficient μ such that $1 - f_1(\mu)$ is the fraction of spheres that can rotate freely ($f_1(0) = 0$ and $f_1(\infty) = 1$), and $f_2(\mu)$: undetermined function of μ indicating the ratio of contacts satisfying $F_t < \mu F_n$, which satisfies $f_2(0) = 0$ and $f_2(\infty) = 1$.

A packing is isostatic when

$$N_n + N_t = E_f + E_t. \tag{3.9}$$

The average coordination number at the isostatic point is then (see Table 3.1):

$$Z(\mu) = 2d\frac{1 + 1/2(d-1)f_1(\mu)}{1 + (d-1)f_2(\mu)}, \tag{3.10}$$

Table 3.1: Number of constraints and variables determining the isostatic condition for different systems of spherical particles.

Friction	N_n	N_t	E_f	E_t
$\mu = 0$	$\frac{1}{2}NZ$	0	dN	0
μ finite	$\frac{1}{2}NZ$	$\frac{1}{2}(d-1)NZf_2(\mu)$	dN	$\frac{1}{2}d(d-1)Nf_1(\mu)$
$\mu = \infty$	$\frac{1}{2}NZ$	$\frac{1}{2}(d-1)NZ$	dN	$\frac{1}{2}d(d-1)N$

reducing to the known $Z = 2d$ for frictionless particles and $Z = d+1$ for infinitely rough particles.

Numerical simulations with packings described in Section 3.7 corroborate this result and further show that the Z vs μ is independent of the preparation protocol as obtained in simulations (see Fig. 3.2). This result then generalizes the isostatic conditions from $\mu = 0$ and $\mu = \infty$ to finite μ. It should be noted that other preparation protocols could give rise to other dependence of Z on μ. However, the obtained phase diagram is given in terms of Z; the main prediction of the theory would still be valid irrespective of the particular dependence $Z(\mu)$. That is, the theory does not assume anything about the relation between the interparticle friction and Z.

3.4.1 Geometrical and mechanical coordination number

There is a difference between the geometrical coordination number z in Eq. (3.7) and the mechanical coordination number Z which counts only the contacts with non-zero forces.

Since some geometrical contacts may carry no force, then:

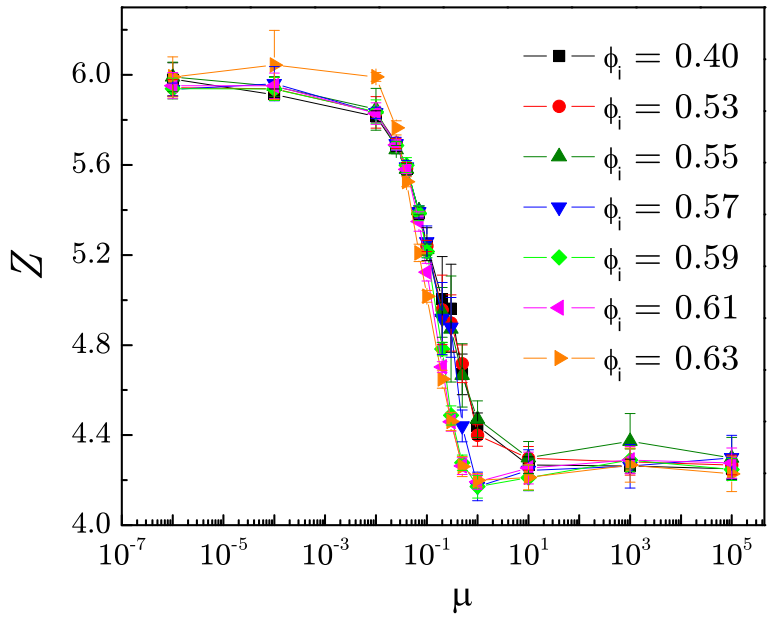

Figure 3.2: Mechanical coordination number versus friction μ obtained in numerical simulations explained in Section 3.7 for different preparation protocols characterized by the initial volume fractions ϕ_i indicated in the figure. The symbols and parameters used in these simulations are the same as in the plot of Fig. 3.7.

$$Z \leq z. \tag{3.11}$$

To show this, imagine a packing of infinitely rough spheres with volume fraction close to 0.64. There must be $z = 6$ nearest neighbors around each particle on the average. However, the mechanical balance law requires only $Z = 4$ contacts per particle on average, implying that 2 contacts have zero force and do not contribute to the contact force network.

Such a situation is possible starting with the contact network of an isostatic packing of frictionless spheres having $z = 6$ and all contacts carrying forces, such that $z = 6$ also, simply allow the existence of tangential forces between the particles and switch the friction coefficient to infinity. Subsequently, solve the force and torque balance equations again for this modified packing of infinitely rough spheres but same geometrical network. Notice that the shear force is composed of an elastic Mindlin component plus the Coulomb condition determined by μ. Thus when $\mu \to \infty$, the elastic Mindlin component still remains.

The resulting packing is mechanically stable and is obtained by setting to zero the forces of two contacts per ball, on average, to satisfy the new force and torque balance condition for the additional tangential force at the contact. Such a solution is guaranteed to exist due to the isostatic condition, because at $Z = 4$ the number of equations equals the number of force variables. Despite mechanical equilibrium, giving $Z = 4$, there are still $z = 6$ geometrical contacts contributing to the volume function.

Therefore, two types of coordination number are identified: the geometrical coordination number, z, contributing to the volume function and the mechanical

coordination number, Z, measuring the contacts that carry forces only. This distinction is crucial to understand the sum over the states and the bounds in the partition function as explained below.

These ideas are corroborated by numerical simulations in Section 3.7.6, below. The packings along the vertical RCP line found in the simulations (see Fig. 3.7) have approximately the same geometrical coordination number, $z \approx 6$. However, they differ in mechanical coordination number, going from the frictionless point $Z = 6$ to $Z \approx 4$ as the friction coefficient is increased to infinity.

A lower bound of the geometrical coordination in Eq. (3.11) is established. The upper bound arises from considering the constraints in the positions of the rigid hard spheres. For hard spheres, the Nd positions of the particles are constrained by the $Nz/2$ geometrical constraints, $|\vec{r}_{ij}| = 2R$, of rigidity. Thus, the number of contacts satisfies $Nz/2 \leq Nd$, and z is bounded by:

$$z \leq 2d. \tag{3.12}$$

Notice that this upper bound applies to the geometrical coordination, z and not to the mechanical one, Z, and it is valid for any system irrespective of the friction coefficient, from $\mu = 0 \rightarrow \infty$.

Furthermore, in relation with the discussion of frictionless isostaticity, it is believed that above $2d$, the system is partially crystallized. To increase the coordination number above 6, it is necessary to create partial crystallization in the packing, up to the point of full order of the FCC lattice with coordination number 12. Thus, by defining the upper bound at the frictionless isostatic limit partially crystalline packings are excluded from the ensemble. This is an important point,

akin to mathematical tricks employed in replica approaches to glasses [73].

In conclusion, the mechanical coordination number, Z, ranges from 4 to 6 as a function of μ, and provides a lower bound to the geometrical coordination number, while the upper bound is $2d$. A granular system is specified by the interparticle friction which determines the average mechanical coordination at which the system is equilibrated, $Z(\mu)$. The possible microstates in the ensemble available for this system follow a Boltzmann distribution Eq. (3.5) for states satisfying the following bounds:

$$Z(\mu) \leq z \leq 2d = 6. \tag{3.13}$$

3.5 Density of states

According to the statistical mechanics of jammed matter, the volume partition function $\mathcal{Q}$ is defined by Eq. (3.5). In the quasiparticle approximation:

$$\begin{aligned} \mathcal{Q}_{\text{sph}}^{\text{hard}}(X) = \int \dots \int g\Big(\sum w(z_i)\Big)\ e^{-\sum w(z_i)/X} \times \\ \times\ \Theta_{\text{jam}}\ \prod_i^N dw(z_i). \end{aligned} \tag{3.14}$$

Considering non-interacting quasiparticles with free volume $w(z)$, the partition function can be written as:

$$\mathcal{Q}_{\text{sph}}^{\text{hard}} = \Big(\int g(w)\ e^{-w/X}\ \Theta_{\text{jam}}\ dw \Big)^N. \tag{3.15}$$

Here, $g(w)$ is the density of states for a given quasiparticle free volume.

Since the mesoscopic w is directly related to z through Eq. (3.7), change variables to the geometrical coordination number in the partition function. The density of states for a single quasiparticle, $g(w)$, is computed as:

$$g(w) = \int_Z^6 P(w|z)g(z)dz, \tag{3.16}$$

where $P(w|z)$ is the conditional probability of a free volume w for a given z, and $g(z)$ is the density of states for a given z.

The next step in the derivation is the calculation of $g(z)$ which is developed in three steps:

First, consider that the packing of hard spheres is in a jammed configuration where there can be no collective motion of any contacting subset of particles leading to unjamming when including the normal and tangential forces between the particles. This definition is an extended version of the collectively jammed category proposed by Torquato *et al.* [74] that goes beyond the merely locally jammed configuration of packings, unstable to the motion of a single particle. While the degrees of freedom are continuous, the fact that the packing is collectively jammed implies that the jammed configurations in the volume space are not continuous. Otherwise there would be a continuous transformation in the position space that would unjam the system contradicting the fact that the packing is collectively jammed. Thus, consider that the configuration space of jammed matter is discrete since configurations cannot be changed from one to another in a continuous way. However, notice that the volume landscape could be continuous since the volume can be changed, or, in the case of soft particles, grain volume can be deformed.

Additionally, in the case of frictionless packings of soft particle, the energy of deformation is well-defined, and the collectively jammed configuration is defined as a minimum in the energy with definitive positive Hessian (or a zero order saddle). In this case, there could be no continuous transformation of the particle coordinates that brings one jammed state to the next, unless the particles are deformed. Thus, the space is discrete in this case as well.

Second, call the dimension per particle of the configuration space as $\mathcal{D}$ and consider that the distance between two jammed configurations is not broadly distributed, meaning that the average distance is well-defined. The typical average distance between configurations in the volume space is considered to be h_z, and therefore the number of configurations per particle is proportional to $1/(h_z)^{\mathcal{D}}$. The constant h_z is very small ($h_z \ll 1$) and plays the role of the Planck's constant, h, in quantum mechanics. The situation is analogous to the discreteness of the configuration space imposed by the Heisenberg uncertainty principle in quantum mechanics. The formula is analogous to the factor h^{-d} for the density of states in equilibrium statistical mechanics. While the degrees of freedom $\{p_i, q_i\}$ are continuous, the uncertainty principle imposes the discreteness $(\Delta p, \Delta q)$ in the configurational space given by $\Delta p \Delta q \sim h$. Formally, the sum over the states E_ν in equilibrium $\Sigma_\nu \exp(-\beta E_\nu)$ is replaced by, $\int \exp(-\beta E(p_i, q_i))\Pi_i(dq_i dp_i/h^d)$.

Third, add z constraints per particle due to the fact that the particle is jammed by z contacts. Thus, there are Nz position constrains ($|\vec{r}_{ij}| = 2R$) for a jammed state of hard spheres as compared to the unjammed "gas" state. Therefore, the number of degrees of freedom is reduced to $\mathcal{D} - z$, and the number of configurations is then $1/(h_z)^{\mathcal{D}-z}$. Note that since the term $1/(h_z)^{\mathcal{D}}$ is a constant, it will

not influence the average of the observables in the partition function, although it changes the value of the entropy. Therefore:

$$g(z) = (h_z)^{z-\mathcal{D}} = e^{-(z-\mathcal{D})/z_c}, \tag{3.17}$$

with $z_c^{-1} \equiv \ln(1/h_z)$. Physically, it is expected $h_z \ll 1$, such that $g(z)$ is an exponentially rapid decreasing function with z. The most populated state is the highest volume at $z = 4$ while the least populated state is the ground state at $z = 6$.

The negative of the geometrical coordination number, $-z$, plays the role of a dimensionality or number of degrees of freedom for a packing, due to the extra position constrains of the contacting particles. The coordination z can be then considered as the number of degrees of "frozen" per particle. Another way to understand Eq. (3.17) is the following. In the case of a continuous phase space of configurations $\frac{g(z+1)}{g(z)} = 0$. However, since the space of volume configurations is discrete as discussed above, the ratio $\frac{g(z+1)}{g(z)} \sim h_z$. This implies again Eq. (3.17).

The conditional probability $P(w|z)$ depends on the w function, $w = \frac{2\sqrt{3}}{z}$. The average is taken over a certain mesoscopic length scale since the volume of a particle depends on the positions of the particles surrounding it. Practically, such length scale is approximately of several particle diameters. w is a coarse-grained volume and independent of the microscopic partition of the particles, implying:

$$P(w|z) = \delta(w - 2\sqrt{3}/z). \tag{3.18}$$

The meaning of Eq. (3.18) is that fluctuations in the coordination number are

neglected due to the coarse graining procedure. A more general ensemble can be considered where the fluctuations in the geometrical coordination number are taken into account.

Substituting Eq. (3.18) and Eq. (3.17) into Eq. (3.15), the isostatic partition function becomes:

$$\mathcal{Q}_{\rm iso}(X,Z) = \int_Z^6 (h_z)^z \exp\left(-\frac{2\sqrt{3}}{zX}\right) dz. \tag{3.19}$$

3.6 Phase diagram

Here the equations of state define the phase diagram of jammed matter by solving the partition function. From Eq. (3.19), the average volume fraction $\phi^{-1} = w+1 = 2\sqrt{3}/z + 1$ is:

$$\begin{aligned} &\phi(X,Z) = \\ &\frac{1}{\mathcal{Q}_{\rm iso}(X,Z)} \int_Z^6 \frac{z}{z+2\sqrt{3}} \exp\left(-\frac{2\sqrt{3}}{zX} + z\ln h_z\right) dz. \end{aligned} \tag{3.20}$$

(a) In the limit of vanishing compactivity ($X \to 0$), only the minimum volume or ground state at $z = 6$ contributes to the partition function. This results in the ground state of jammed matter with a density:

$$\phi_{\rm RCP} = \phi(X=0,Z) = \frac{6}{6+2\sqrt{3}} \approx 0.634, \quad Z(\mu) \in [4,6]. \tag{3.21}$$

The meaning of the subscript RCP in (3.21) will become clear below.

(b) In the limit of infinite compactivity ($X \to \infty$), the Boltzmann factor

$\exp[-2\sqrt{3}/(zX)] \to 1$, and the average in (3.20) is taken over all the states with equal probability:

$$\phi_{\mathrm{RLP}}(Z) = \phi(X \to \infty, Z) = \\ \frac{1}{\mathcal{Q}_{\mathrm{iso}}(\infty, Z)} \int_Z^6 \frac{z}{z + 2\sqrt{3}} \exp\left(z \ln h_z\right) dz. \tag{3.22}$$

The constant h_z determines the minimum volume in the phase space. With $h_z \ll 1$, the exponential in Eq. (3.22) decays rapidly. Then the leading contribution to Eq. (3.22) is from the highest volume at $z = Z$ and therefore:

$$\phi_{\mathrm{RLP}}(Z) \approx \frac{Z}{Z + 2\sqrt{3}}, \quad Z(\mu) \in [4, 6]. \tag{3.23}$$

This dependence of the volume fraction on Z suggests using the (ϕ, Z) plane to define the phase diagram of jammed matter as plotted in Fig. 3.3. The equations of state (3.21) and (3.23) are plotted in the (ϕ, Z) plane in Fig. 3.3 providing two limits of the phase diagram. Since the mechanical coordination number is limited by $4 \leq Z \leq 6$ there are two horizontal limits: The phase space is delimited from below by the minimum coordination $Z = 4$ for infinitely rough grains, denoted the granular-line or G-line in Fig. 3.3.

All mechanically stable disordered jammed packings lie within the confining limits of the phase diagram (indicated by the yellow zone in Fig. 3.3), while the grey shaded area in Fig. 3.3 indicates the forbidden zone. For example, a packing of frictional hard spheres with $Z = 5$ (corresponding to a granular material with interparticle friction $\mu \approx 0.2$ according to Fig. 3.2) cannot be equilibrated

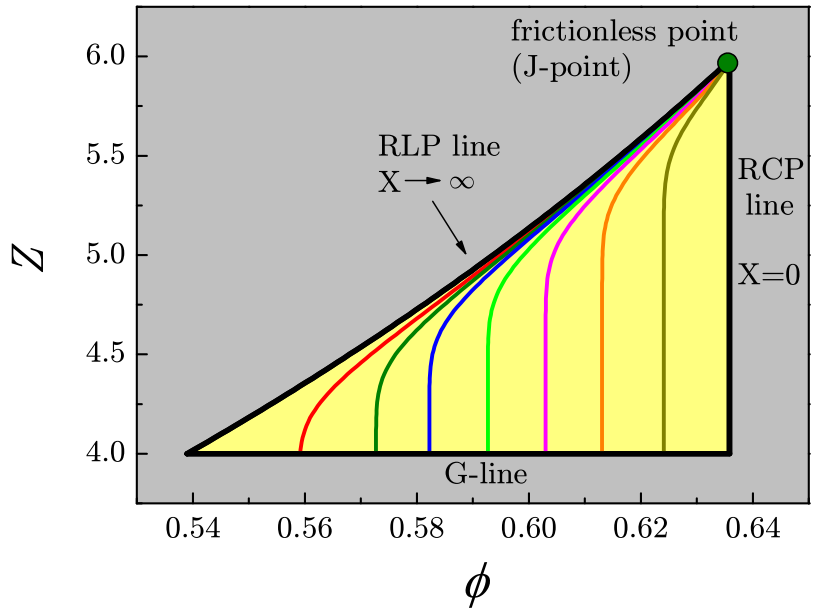

Figure 3.3: **Phase diagram of jammed matter: Theory**. Theoretical prediction of the statistical theory. All disordered packings lie within the yellow triangle demarcated by the RCP line, RLP line and G line. Lines of finite isocompactivity are in color. The grey area is the forbidden zone where no jammed packings can exist.

at volume fractions below $\phi < \phi_{\text{RLP}}(Z = 5) = 5/(5 + 2\sqrt{3}) = 0.591$ or above $\phi > \phi_{\text{RCP}} = 0.634$. It is worth noting that particular packings can exist in the forbidden zone; it is contended that they are zero measure and therefore have zero probability of occurrence at the ensemble level.

An important prediction is that for frictionless systems there is only one possible state at $Z = 6$. It is important to note that there is one state only at the mesoscopic level used in the theory. However, for a single mesoscopic state, many microstates are expected and are averaged out in the mesoscopic theory of the volume function. Thus, there could be more jammed states surrounding the frictionless point in the phase diagram. However, these states are further expected to be clustered in a narrow region around the frictionless point. To access these microstates it would require different preparation protocols, analogous to the dependence of the glass transition temperature on cooling rates in glasses [73].

(ii) **Definition of RLP.**— The equation of state (3.23) provides the lowest volume fraction for a given Z and represents a statistical definition of the RLP limit depicted by the RLP-line in Fig. 3.3. To the left of this line, packings are not predicted to be mechanically stable or they are experimentally irreversible as discussed in [20, 56, 75].

A review of the literature indicates that there is no general consensus on the value of RLP as different estimations have been reported ranging from 0.55 to 0.60 [45, 48, 47], proposing that there is no clear definition of RLP limit. The phase diagram proposes a solution to this problem. Following the infinite compactivity RLP-line, the volume fraction of the RLP decreases with increasing friction from the frictionless point $(\phi, Z) = (0.634, 6)$, towards the limit of infinitely rough hard

spheres, $Z \to 4$. Indeed, experiments [45] indicate that lower volume fractions are achieved for larger coefficient of friction. The lowest volume fraction in the limit is predicted: $\mu \to \infty$, $X \to \infty$ and $Z \to 4$ (and $h_z \ll 1$) at

$$\phi_{\rm RLP}^{\rm min} = \frac{4}{4+2\sqrt{3}} \approx 0.536. \tag{3.24}$$

Even though this is a theoretical limit, results indicate that for $\mu > 1$ this limit can be approximately achieved. The finding of a random loose packing bound is an interesting prediction of the present theory. The RLP limit has not been well investigated experimentally, and so far it was not certain whether this limit can or cannot be reached in real systems. The lowest stable volume fraction ever reported, 0.550 ± 0.006, obtained by Onoda and Liniger [48] as the limit of vanishing gravity for spherical glass beads, is not far from the present prediction.

The intersections of the RCP, RLP and the G-line identify three interesting points in the $(\phi, Z(\mu))$ plane:

(a) The frictionless point [63] $\mu = 0$, denoted J-point in [64], at J$\equiv (\phi_{\rm RCP}, Z) \equiv (0.634, 6)$ corresponds to a system of compressed emulsions in the limit of small osmotic pressure as discussed in Chapter 4. (b) The lowest possible coordination number $Z = 4$ plotted as the G-line defines two associated points from the lowest volume fraction of loose packings, L-point, $L \equiv (\phi_{\rm RLP}, Z) = (0.536, 4)$, to the zero compactivity state of close packing, C-point, $C \equiv (\phi_{\rm RCP}, Z) = (0.634, 4)$. The full JLC triangle defines the isostatic plane where the jammed hard sphere packings reside.

Of interest is the dependence of the prediction of the "Planck constant" of jammed matter, h_z, that determines the minimum volume in the phase space.

The equation of state (3.23) and the prediction of the minimum RLP, Eq. (3.24) have been obtained by considering $h_z \to 0$ but still nonzero. Thus, the only state contributing to the volume partition function is the most populated at $z = 4$ in the case of $X \to \infty$. The approximation $h_z \ll 1$ is a sensible one, since the discretization of the space is supposed to be very small. However, this constant remains a fitting parameter of the theory. Indeed the simulations use a value of $h_z = e^{-100}$ in order to fit the theoretical values with the numerical ones for finite compactivity. This extremely small constant shifts the value of the minimum RLP a little bit to the right of the phase diagram from the prediction of Eq. (3.24). Indeed, when plotting the phase diagram of Fig. 3.3 with a $h_z = e^{-100}$ a slightly larger value of $\phi_{\mathrm{RLP}}^{\mathrm{min}}$ is obtained as seen in Fig. 3.3. In the limit of $h_z \to 1$ a minimum RLP value of $(\phi_{\mathrm{RLP}}^{\mathrm{min}} + \phi_{\mathrm{RCP}})/2$ is obtained, although this would correspond to an unphysical situation. However, it should be stressed that all the above argument depend on the assumed exponential form of the density of states. Without an exact form for the density of states, the results could change if other more accurate form is found to be valid. On the other hand the prediction of the ground state at RCP, Eq. (3.21), remains unaffected by the density of state or the value of h_z.

It is interesting to note that the compactivity can be extended to negative values and study the limit $X \to 0^-$. Indeed, for any value of h_z, the prediction of Eq. (3.23) is obtained. If the expectation $h_z \ll 1$ is correct, it may not be necessary to use the negative compactivity states to describe RLP. Being sure, that it is still very difficult to accept the notion of compactivity in many quarters, even 20 years following its inception, and negative compaction may be an even

more arbitrary concept at this point. This will be discussed in greater detail in Chapter 5

(iii) Intermediate isocompactivity states.— For finite X, Eq. (3.20) can be solved numerically. For each X, the function $\phi(X, Z)$ can be obtained and is plotted as each isocompactivity color line in Fig. 3.3. Between the two limits Eqs. (3.21) and (3.23), there are packings inside the yellow zone in Fig. 3.3 with finite compactivity, $0 < X < \infty$. Since X controls the probability of each state, like in condensed matter through a Boltzmann-like factor in Eq. (3.5), it characterizes the number of possible ways to rearrange a packing having a given volume and entropy, S. Thus, the limit of the most compact and least compact stable arrangements correspond to $X \to 0$ and $X \to \infty$, respectively. Between these limits, the compactivity determines the volume fraction from RCP to RLP.

3.6.1 Equations of state

Further statistical characterization of the jammed structures can be obtained through the calculation of the equations of state in the three-dimensional space (X, ϕ, S) as seen in Fig. 3.4.

The entropy density, $s = \frac{S}{N}$, is obtained as:

$$s(X, Z) = \langle w \rangle / X + \ln \mathcal{Q}_{\text{iso}}(X, Z) \tag{3.25}$$

This equation is obtained in analogy with equilibrium statistical mechanics and it is analogous to the definition of free energy: $F = E - TS$ where $F = -T \ln \mathcal{Q}$ is the free energy. Replace $T \to X$, $E \to \langle w \rangle$. Therefore, $F = E - TS$ or

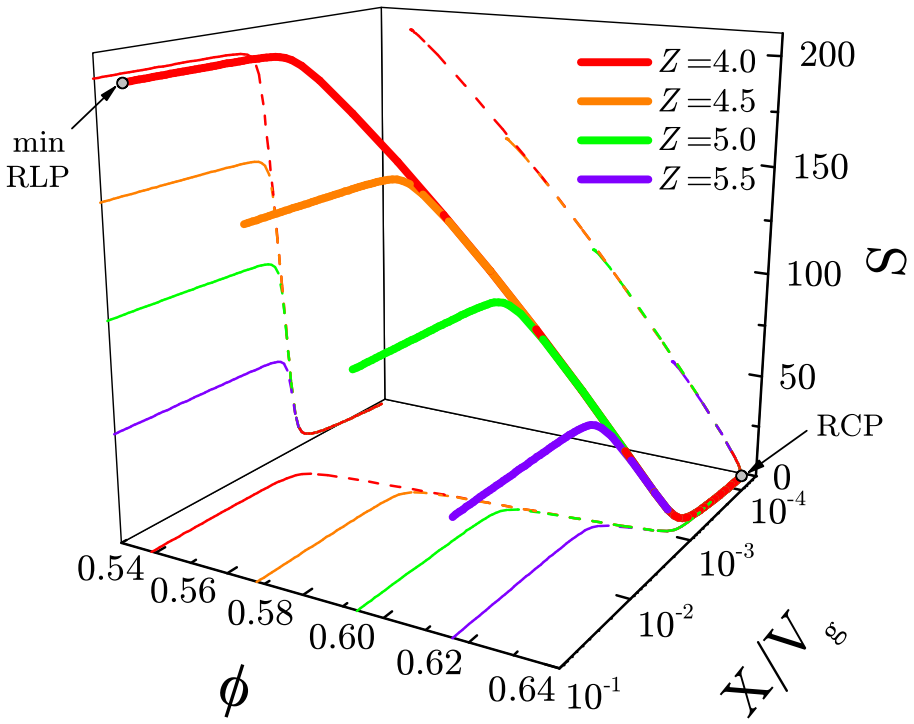

Figure 3.4: **Predictions of the equation of state of jammed matter in the (X, ϕ, S) space.** Each line corresponds to a different system with Z as indicated. The projections in the (ϕ, S) and (X, S) planes show that the RCP ($X = 0$) is less disordered than the RLP ($X \to \infty$). The projection in the (X, ϕ) plane resembles qualitatively the compaction curves of the experiments [20, 56, 75].

$S = (E - F)/T = E/T + \ln \mathcal{Q}$ is now $s(X, Z) = \langle w \rangle / X + \ln \mathcal{Q}_{\rm iso}(X, Z)$, which is plotted as the equation of state in Fig. 3.4. For the calculation of s consider $g(z) = {h_z}^{z-2d}$ since for $z = 2d$ there is only one mesoscopic state or $g(z) = e^{-\frac{z-2d}{z_c}}$ with $z_c = \frac{1}{\ln(h_z^{-1})} = 0.01$ as used in Fig. 3.4 and 3.7. This correction is irrelevant for average quantities like $\phi(X, Z)$ but determines a constant factor in the entropy from the term $\ln \mathcal{Q}_{\rm iso}$.

Each curve in the figure corresponds to a system with a different $Z(\mu)$. The projections $S(X)$ and $S(\phi)$ in Fig. 3.4 characterize the nature of randomness in the packings. When comparing all the packings, the maximum entropy is at $\phi_{\rm RLP}^{\rm min}$ and $X \to \infty$ while the entropy is minimum for $\phi_{\rm RCP}$ at $X \to 0$. Following the G-line in the phase diagram the entropy for infinitely rough spheres is larger for RLP than RCP. The same conclusion is obtained for the other packings at finite friction ($4 < Z(\mu) < 6$). The RLP states are more disordered than the RCP states. Approaching the frictionless J-point, $\mu \to 0$ ($Z = 6$) the entropy vanishes. More precisely, it vanishes for a slightly smaller ϕ than $\phi_{\rm RCP}$ of the order h_z. Strictly speaking it diverges to $-\infty$ at $\phi_{\rm RCP}$ as $S \to \ln X$ for any value of Z, in analogy with the classical equation of state, when approaching RCP to distances smaller than h_z. However, this is an unphysical limit, as it would be considering distances in phase space smaller than the Planck constant.

It is commonly believed that the RCP limit corresponds to a state with the highest number of configurations and therefore the highest entropy. However, the states with a higher compactivity have a higher entropy, corresponding to looser packings. Within a statistical mechanics framework of jammed matter, this result is a natural consequence. and gives support to such an underlying statistical

picture. A more detailed study of the entropy is performed in Chapter 5.

The interpretation of the RCP as the ground state, $X \to 0$, with vanishing entropy, $S \to 0$, warrants an elaboration. Since there exist packings above RCP all the way to $\phi_{\text{fcc}} = 0.74048$, these packings have some degree of order. These packings do not appear in the presented theory, treating only disordered packings characterized by the mesoscopic volume function derived under the isotropic assumption. Crystals or partially crystalline packings are not considered in the ensemble. This interprets the RCP in the context of the found third-law of thermodynamics. Neglecting the crystal state from the ensemble has analogies in replica treatment of glasses [76].

The equation of state $\phi(X)$ for different values of Z can be seen in the projection of Fig. 3.4. The volume fraction diminishes with increasing compactivity according to the theoretical picture of the phase diagram. The curves $\phi(X)$ qualitatively resemble the reversible branch of compaction curves in the experiments of [20] for shaken granular materials and oscillatory compression of grains [75] suggesting a correspondence between X and shaking amplitude. The contention is that, different control parameters in experiments could be related to a state variable, and therefore might help experimentalists to describe results obtained under different protocols. For any value of Z, there is a common limit $\phi \to \phi_{\text{RCP}}$ as $X \to 0$, indicating the constant volume fraction for all the RCP states. The singular nature of the frictionless J-point is revealed as the volume fraction remains constant for any value of X, explaining why this point is the confluence of the isocompactivity lines, including RCP and RLP. At the frictionless J-point the compactivity does not play a role, at least at the mesoscopic level.

3.6.2 Experimental realization of the phase diagram

A reanalysis of the available experimental data tends to agree with the above theoretical predictions. However, it would be desirable to perform more controlled experiments in light of the present results. As in other out of equilibrium systems, such as glasses, the inherent path-dependency of jammed matter materializes in the fact that different packing structures can be realized with different preparation protocols [77, 20, 56, 75, 78] involving tapping, fluidized beds, settling particles at different speeds, acoustic perturbations or pressure waves [48].

Previous experiments [48] and simulations [72] find that lower volume fractions can be achieved for smaller settling speeds of the grains or slower compression, or quenching, rates during packing preparation. Colloidal glasses find a similar scenario [73, 89], with their glass transition temperature dependence on the quench rate of cooling, although due to different reasons. This raises the question of whether the jamming point is unique or determined by the preparation protocol [89].

The experiments performed by Onoda and Liniger with glass spheres in liquid of varying density to adjust conditions of buoyancy in the limit of vanishing gravity show that for larger values of gravity, the volume fraction decreases. This indicates that settling speed of the particles can determine the final volume fraction. Indeed, it was found numerically that the compression rate during preparation of the packings is a systematic way to obtain lower packing fractions, such that lower volume fractions can be achieved with quasi-static compression rates during preparation of the packings [72].

These results provide a hint on how to generate the packings in the phase space

and they are exploited in the following section treating the dynamical generation of the packings predicted in the phase diagram. Since Z is directly determined by μ, and the compactivity determines what value of the volume fraction a packing has between the limits of the phase diagram, the main question is how to generate packings with different ϕ for a fixed μ to allow the exploration of the phase diagram.

3.7 Numerical tests

In this section two different numerical tests are performed: on the predictions of the theory and the assumptions of the theory. The former are explained in Section 3.7.3 while the latter are elaborated in Section 3.7.6. It is worth mentioning that the predictions can be tested with packings prepared numerically and experimentally. However, the test of the assumptions of the theory is not so trivial. This is because the theory is based on the existence of quasiparticles which carry the information at a mesoscopic scale. Thus, quasiparticles cannot be measured using real packings such as computer generated packings or experimental ones. The information obtained from those packings already contains ensemble averages through the Boltzmann distribution and density of states. In principle, it is not possible to isolate the behavior of quasiparticles from the real measures rendering difficult to properly test some of the assumptions and predictions of the theory at the more basic mesoscopic scale. Nevertheless, Section 3.7.6 describes such a test. These packings are obtained as flat averages in the ensemble without the corresponding Boltzmann factor and may contain direct information on the mesoscopic fluctuations.

The existence of the theoretically inferred jammed states opens such predictions to experimental and computational investigation. Numerical tests predict the phase diagram by preparing monodisperse packings of Hertz-Mindlin [70, 71] spheres with friction coefficient μ at the jamming transition using methods previously developed [63, 72, 79, 80].

Although diverse states are predicted by the theory, they may not be easily accessible by experimentation due to their low probability of occurrence. For instance packings close to the C-point, having a high volume fraction, high friction, and low mechanical coordination number, are difficult to obtain. Nevertheless, the advantage of the theoretical framework is that it systematically classifies the different packings into a coherent picture of the phase diagram. In the following different preparation protocols generate all the phase space of jamming.

Different packing states are achieved by compressing a system from an initial volume fraction ϕ_i with a compression rate Γ in a medium of viscosity (damping) η where the particles are disperse. The system is defined by the friction coefficient μ which set $Z(\mu)$ according to Fig. 3.2. While the simulations are not realistic (no gravity, boundaries, or realistic protocol is employed), they provide a way to test the main predictions of the theory. The final state (ϕ, Z) is achieved by the system for every $(\phi_i, \Gamma, \eta, \mu)$ at the jamming transition of vanishing stress with a method explained next.

It should be noted though that other experimental protocols could be also adapted to the exploration of the phase diagram, including (a) Gentle tapping with servo mechanisms that adjust the system at a specified pressure [80], (b) Gentle tapping with external oscillatory perturbations, (c) Settling of grains under

gravity in a variety of liquids with viscosity η, (d) fluidized beds.

Relation with hard sphere simulations.— The present algorithm finds analogies with recent attempts to describe jamming using ideas coming from the theory of mean-field spin glasses and optimization problems [73, 89]. This is an interesting situation since it has been shown that in the case of hard spheres the system always crystallizes unless an infinite quench is applied [61]. However, soft sphere simulations do not produce appreciable crystallization in the packing.

One could imagine that there exists a typical quench rate, depending on the stiffness of the grains, as a division of the ordered and disordered (jammed) phases. It is interesting to note that at the hard-sphere limit, $G \to \infty$, all the packings are in the ordered phase except when $\Gamma \to \infty$, where $\phi \approx 0.64$. This explains the behavior of the hard sphere packings found in previous works [61]. For the soft ball case, the situation is more subtle since a certain range of compression rate is acceptable for the acquirement of disordered packings. It is in this range that simulations are performed.

According to this picture, in the theoretical limit of infinitely slow quench rates, the system should in principle crystallize for any G. In granular matter, this limit is almost impossible to achieve, since it is always found that the system is random and far from the crystal structure. This is in part because, in the absence of temperature bath, the granular system is always stuck in a jammed configuration far from the crystal one. The contention is that for a well defined set of quenches the system does not crystallize and the study of the disordered phase ensues. Indeed, numerical and experimental evidence points to the validity of this assertion. The present theory neglects the existence of the ordered phase

and assumes an ensemble of the disordered states.

3.7.1 Molecular dynamics simulations of grains

Static packings of spherical grains are prepared interacting via elastic forces and Coulomb friction [63, 72]. The system size ranges from $N = 1,024$ to $N = 10,000$ particles. Two spherical grains in contact at positions $\vec{x}_1$ and $\vec{x}_2$ and with radius R interact with a Hertz normal repulsive force [70]

$$F_n = \frac{2}{3}\, k_n R^{1/2} \delta^{3/2}, \tag{3.26}$$

and an incremental Mindlin tangential force [71]

$$\Delta F_t = k_t (R\delta)^{1/2} \Delta s, \tag{3.27}$$

Here the normal overlap is $\delta = (1/2)[2R - |\vec{x}_1 - \vec{x}_2|] > 0$. The normal force acts only in compression, $F_n = 0$ when $\delta < 0$. The variable s is defined such that the relative shear displacement between the two grain centers is $2s$. The prefactors $k_n = 4G/(1-\nu)$ and $k_t = 8G/(2-\nu)$ are defined in terms of the shear modulus G and the Poisson's ratio ν of the material from which the grains are made. $G = 29$ GPa and $\nu = 0.2$ typical values for spherical glass beads and $R = 5 \times 10^{-3}$ m and the density of the particles, $\rho = 2 \times 10^3$ kg/m^3. Viscous dissipative forces are added at the global level affecting the total velocity of each particle through a term $-\gamma \dot{\vec{x}}$ in the equation of motion, where γ is the damping coefficient related to

the viscosity of the medium $\eta = \gamma/(6\pi R)$. Sliding friction is also considered:

$$F_t \leq \mu F_n. \tag{3.28}$$

That is, when F_t exceeds the Coulomb threshold, μF_n, the grains slide and $F_t = \mu F_n$, where μ is the static friction coefficient between the spheres. Time is measured in units of $t_0 = R\sqrt{\rho/G}$, the compression rate in units of $\Gamma_0 = 5.9t_0^{-1}$ and the viscosity in units of $\eta_0 = 8.2R^2\rho/t_0$. The dynamics follows integration of Newton's equation for translations and rotations.

3.7.2 Preparation protocol: Packings at the jamming transition with the split algorithm

The critical volume fraction at the jamming transition, ϕ_c will be identified by the "split" algorithm as explained in [72], allowing one to obtain packings at the critical density of jamming with arbitrary precision. Preliminary results indicate that lower values of ϕ_c are obtained for slow compression [72]. Thus by varying Γ or η the phase space will be explored. Also, the initial ϕ_i plays an important role in achieving packings close to the RCP line.

The preparation protocol consists of first preparing a gas of non-interacting particles at an initial volume fraction ϕ_i in a periodically repeated cubic box. The particles do not interact and therefore the stress in the system is $\sigma = 0$ and $Z = 0$.

To generate a random configuration with friction at volume fraction ~ 0.64 is very difficult. Therefore to achieve any volume fraction in this initial stage, initially the system is frictionless. A very dilute (unjammed gas of non interacting

particles) grain configuration is randomly generated, usually with a volume fraction $\phi_0 \approx 0.30 \sim 0.36$, then an extremely slow isotropic compression is applied without friction on this dilute configuration until the system reaches another unjammed configuration at higher density, ϕ_i. The reason to add an extremely slow isotropic compression to the dilute configuration is to avoid involving any kinetic energy to keep the system as random as possible. After obtaining this unjammed state with initial volume fraction ϕ_i, friction is restored and a compression is applied with a compression rate Γ until a given volume fraction ϕ_1. Then the compression is stopped and the system is allowed to relax to mechanical equilibrium by following Newton's equations without further compression.

After the compression to ϕ_1, two things can occur (see Fig. 3.5):

(a) The system jams: If the system is above the jamming point $\phi_1 > \phi_c$, then the stress will decrease and ultimately stabilize to a finite nonzero value, meaning that the pressure of the system remains unchanged (usually $\Delta\sigma < 10^{-3}$ Pa, red line, Fig 3.5) over a large period of time (usually $\sim 10^7$ MD steps). The coordination number usually has a first initial decrease, but if the system is jammed it will also stabilize at a constant value above the isostatic minimal number (inset Fig. 3.5).

(b) The system is not jammed: here the stress and the coordination number will relax to zero. This fact is illustrated in Fig. 3.5. If the packing has $\phi_1 > \phi_c$, it stabilizes at a non-zero pressure above the jamming transition, but the pressure decreases very quickly to zero (the system is not jammed) if $\phi_2 < \phi_c$, even though ϕ_1 and ϕ_2 differ only by 2×10^{-4}.

A search procedure consisting of several cycles is applied such that in each cycle the lower and upper boundaries of ϕ_c are fixed. The difference between the

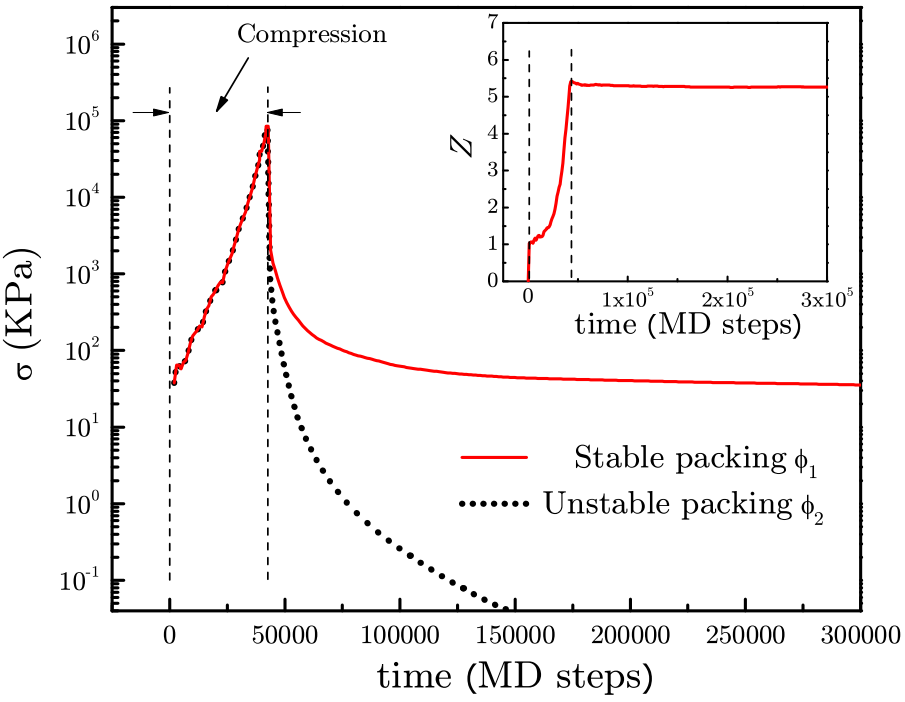

Figure 3.5: Time evolution of stress (the pressure in the system) for two packings simulated as explained in the text. The solid red line represents a packing with $\phi_1 > \phi_c$ and dotted black line represents a packing with $\phi_2 < \phi_c$, where $\phi_1 = \phi_2 + 2 \times 10^{-4}$. The inset shows the time evolution of the coordination number.

boundaries gets smaller as the cycles proceed, meaning that ϕ_c is fixed with higher and higher precision. Starting from the packing of high volume fraction $\phi_1 > \phi_c$ a series of packings are generated with step-decreasing volume fractions until the first packing with zero pressure is observed, which has a volume fraction $\phi = \phi_1 - \Delta\phi$. Thus, ϕ_c is bounded between $\phi_1 - \Delta\phi$ and ϕ_1. Then test if $\phi = \phi_1 - \Delta\phi/2$. If $\phi = \phi_1 - \Delta\phi/2$ is stable, ϕ_c is between $\phi_1 - \Delta\phi$ and $\phi_1 - \Delta\phi/2$. If $\phi = \phi_1 - \Delta\phi/2$ is unstable, ϕ_c is between $\phi_1 - \Delta\phi/2$ and ϕ_1. Therefore, in this cycle, the region where ϕ_c possibly lies in is reduced from $\Delta\phi$ to $\Delta\phi/2$. If this cycle is carried out for n times, the precision is improved to $\Delta\phi_n = \Delta\phi/2^n$. In the simulations cycling ceases when $\Delta\phi_n$ gets below 2×10^{-4} and $n = 12$. A similar algorithm was employed in [72] to study the approach to the jamming transition by preparing packings at a finite pressure.

It is important to determine whether the packings are jammed in the sense that they are not only mechanically stable but also they are stable under perturbations. Numerical protocols herein assure that the system is at least locally jammed since each particle is in mechanical equilibrium [74]. To test if the system is collectively jammed is more involved. For frictionless systems, where tangential forces are removed, the Hertz energy $U_{\text{hertz}} = \frac{4}{15}\ k_n R^{1/2} \delta^{5/2}$ is used to test whether the Hessian of the jammed configurations is positive [64]. The frictionless configurations have positive Hessian indicating that they are collectively jammed. However, this method is not useful when considering frictional systems. The energy of deformation depends on the path taken to deform the system and cannot be defined uniquely. In this case, a numerical test of the stability of the packings applies a small random velocity to each jammed particle. The packings are stable to small

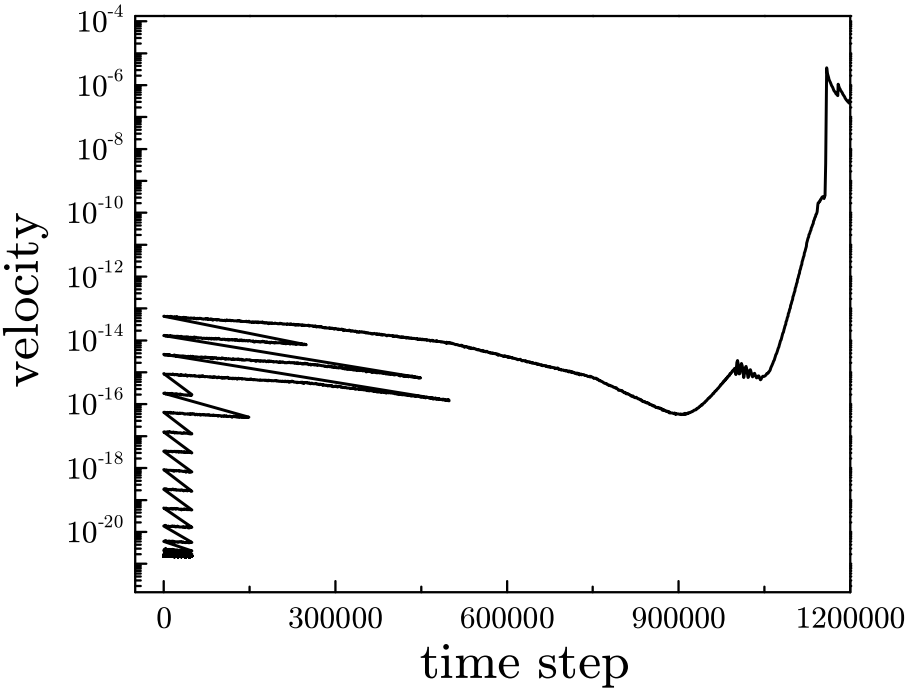

Figure 3.6: Study of the stability of the packings under perturbations.

perturbations consisting of external forces of the order of 0.1 times the value of the average force, indicating that the packings may be collectively jammed (see Fig 3.6).

3.7.3 Results: phase diagram

Figure 3.7 shows the results for a system of $N = 1024$. Each data point corresponds to a single set of $(\phi_i, \Gamma, \eta, \mu)$ and is averaged over these 10 realizations, where $0.40 \leq \phi_i \leq 0.63$, $10^{-7} \leq \Gamma \leq 10^{-3}$, $10^{-4} \leq \eta \leq 10^{-3}$, and $0 \leq \mu \leq \infty$. The error of ϕ_c obtained over the 10 realizations as shown in Fig. 3.7 is usually 5×10^{-4}, larger than the precision of the split algorithm (2×10^{-4}). In general, all numerically generated jammed states lie approximately within the predicted bounds of the

phase diagram.

The plot in Fig. 3.7a explores the dependence of the packings (ϕ, Z) on the initial state ϕ_i. (In the plot, ϕ refers to the ϕ_c obtained in a split algorithm). In Fig. 3.7 results are plotted for a fixed quench rate $\Gamma = 10^{-7}$ and damping coefficient $\eta = 10^{-3}$ (except for the last orange curve on the right with $\eta = 10^{-4}$) and for different initial states ranging from left to right (see Fig. 3.7 for details) Each color here corresponds to a particular ϕ_i (0.40 at the left to 0.65 at the right), while each data point along a curve corresponds to a prepared system at a given friction from $\mu = 0$ at $Z \approx 6$ to $\mu \to \infty$ at $Z \approx 4$. For the states observed having $\mu = 0.8$, there is an almost horizontal line with $Z \approx 4.4$, as shown in Fig. 3.7a.

The packings prepared from the larger initial densities ϕ_i closely reproduce the RCP line of zero compactivity at ϕ_{RCP}, confirming the prediction that the frictionless J-point at $Z = 6$ but extend along the vertical line until $Z \approx 4$.

The packings along the RCP line have equal geometrical coordination number $z \approx 6$ but differ in their mechanical one from $Z = 6$ to $Z \approx 4$, in agreement with theory (see Section 3.7.6). These states are then identified with the ground state of jammed matter.

In the limit of small densities for the initial state (see curves for $\phi_i = 0.40, 0.53, 0.55$ in the phase space Fig. 3.7a, the predictions of the RLP-line are approximately reproduced. These packings follow the theoretical prediction for infinite compactivity except for deviations (less than 5%) in the coordination number for packings close to the lower value of $Z = 4$, where the numerical curve seems to flatten out deviating from the theory. Numerically, the lowest volume fraction is found at $\phi_{\mathrm{RLP}}^{\mathrm{min}} = 0.539 \pm 0.003$, close to the theoretical prediction, $\phi_{\mathrm{RLP}}^{\mathrm{min}} = 0.536$.

Packings with the lowest Z correspond to infinitely rough spheres. The deviation of coordination number between theory and simulation (specially at low volume fraction) could be from the system not achieving an isostatic state at infinite friction. In general, while there are many states along the RLP line, the barriers of these states decrease as the coordination number decreases towards $Z = 4$, i.e. when the friction increases. Thus, the states at the lower left part of the phase diagram are very difficult to equilibrate.

Besides the states delimiting the phase space, other packings are generated with intermediate values of $\phi_i = 0.57, 0.59, 0.61$ as shown in Fig. 3.7a. Interestingly, these states (all obtained for fixed $\Gamma = 10^{-7}$ and $\eta = 10^{-3}$) closely follow the predicted lines of isocompactivity as indicated in the figure. The simulations from $\phi_i = 0.57, 0.59, 0.61$ correspond to compactivities $X = 1.62, 1.38$, and 1.16, respectively (measured in units of $10^{-3}V_g$).

The constant h_z weakly affects the finite compactivity lines and $h_z = e^{-100}$ provides the best fit to the data for finite isocompactivity lines in Fig. 3.7a. Thus, with reasonable approximation and for this particular protocol, the density of the initial state, ϕ_i is identified with the compactivity of the packing, providing a way to prepare a packing with a desired compactivity. However, it should be noted that other values of h_z produce approximately the same phase diagram boundaries (i.e., the RLP and RCP lines, as long as $h_z \ll 1$) but do not fit the isocompactivity lines within as accurately. Thus, the identification of the compactivity with ϕ_i remains dependent on this particular value of h_z used to fit the theory.

It is also interesting to investigate the packings generated by fixed friction and varying quenched rate, since this situation corresponds to a given system. For a

given μ a common value of $Z(\mu)$ independent of Γ, is found, as discussed in Fig. 3.2, indicating that the curve $Z(\mu)$ is independent of the protocol. Thus, a fixed μ corresponds to a horizontal line in the phase diagram as indicated in Fig 3.7a for $\mu = 0.8$ and $Z(0.3) = 4.4$. The value of the friction coefficient determines $Z(\mu)$ independently of the value of (Γ, ϕ_i, η) as seen in Fig. 3.2. Thus, in terms of the phase diagram in Fig. 3.7a, a given μ defines a horizontal line between the RCP and RLP limits.

The least difficult packings to generate are along the RLP line while the most difficult are deep in the phase diagram with low coordination number (large friction) and high volume fraction, that is near the C-point. In general, always start with a dilute (non-interacting gas) sample without friction and compressed slowly until another dilute sample not jammed at a volume fraction ϕ_i. If ϕ_i is around or smaller than 0.55 then the RLP line is obtained. If the compression rate is decreased even by 3 orders of magnitudes, packings move inside the phase diagram, though not substantially, as indicated schematically in the figure.

In order to access the inner states at high friction, one must take another route. A frictionless dilute unjammed sample is prepared at a higher ϕ_i, which can be as close as possible to ~ 0.64 since frictionless spheres only jam at RCP. Then friction is applied and all the packings inside the phase diagram can be achieved. Experimentally, this path could be reproduced by stabilizing a frictional packing with fast compressions and resetting the interparticle forces by gently tapping. This simulates the loss of path dependence induced by the initial compression without friction and may allow one to reach the packings around the C-point.

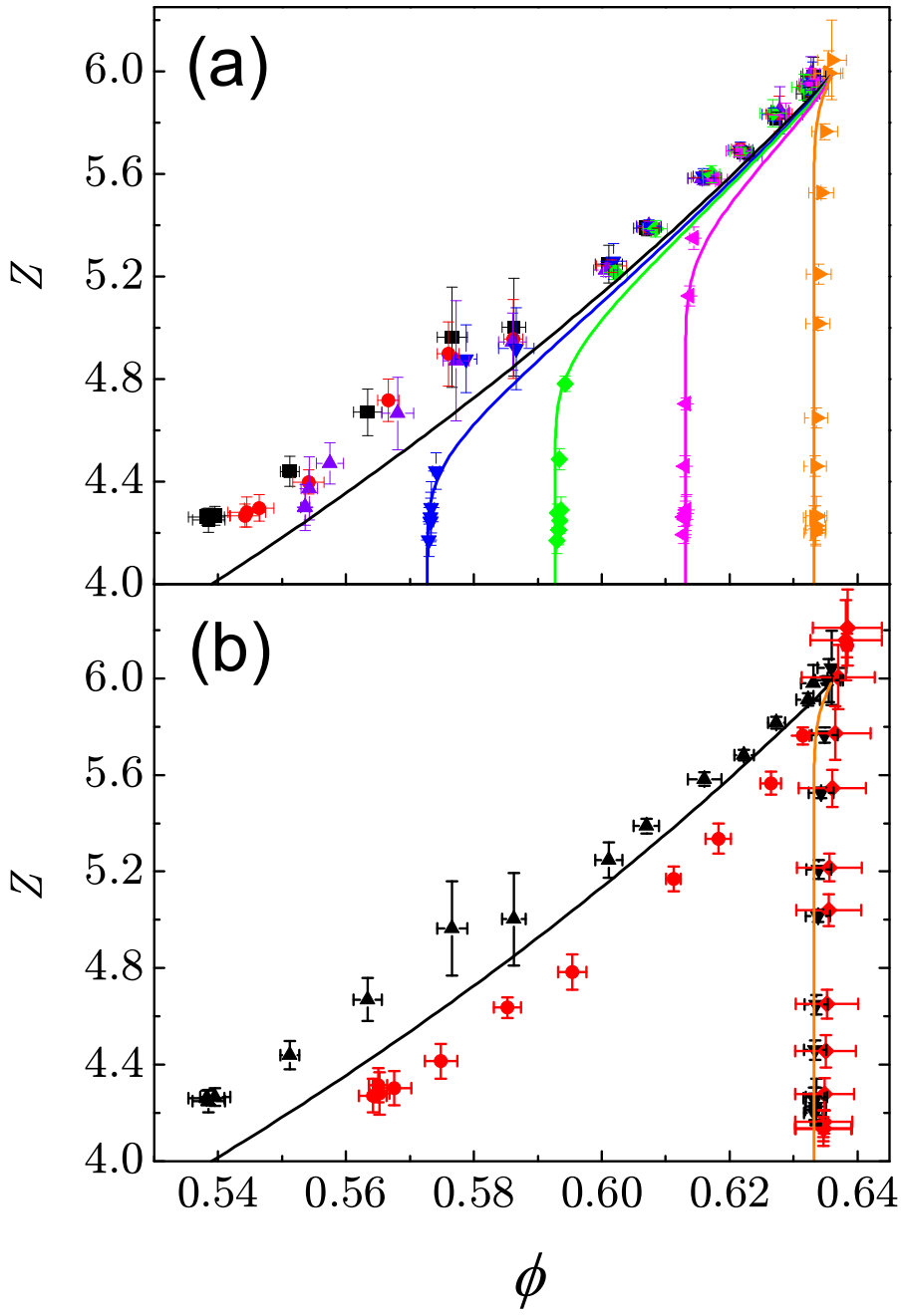

Figure 3.7: Phase diagram of jammed matter: Simulations. Numerical simulations demonstrate how to dynamically access the theoretically found states. The numerical protocol is parameterized by $(\phi_i, \Gamma, \eta, \mu)$. (a) The plot shows the dependence of the final jammed states (ϕ, Z) on ϕ_i for a fix $\Gamma = 10^{-7}$ and $\eta = 10^{-3}$ (except for the orange curve which is for $\eta = 10^{-4}$) from left to right $\phi_i = 0.40$ (black), 0.53 (red), 0.55 (violet), 0.57 (blue), 0.59 (green), 0.61 (pink) and 0.63 (orange). Each equal-color line set represents a different ϕ_i and each data point along equal-color line represents a different μ. Solid lines represent the theoretical results with $h_z = e^{-100}$ or $z_c = 0.01$ for different compactivities measured in units of $10^{-3}V_g$. From left to right $X = \infty$ (black solid line), 1.62 (blue solid line), 1.38 (green solid line), 1.16 (pink solid line) and 0.88 (orange solid line). The error bars correspond to the s.d. over 10 realizations of the packings. (b) The plot focuses on the dependence of (ϕ, Z) on (Γ, η) for two different ϕ_i. Solid black symbols are

3.7.4 Compactimeter for granular matter

At this point there is no theoretical explanation for why packings with the same initial unjammed state ϕ_i end up having the same compactivity when jammed after compression. It is important to note that this finding is based on the particular value used for h_z, such that a change in h_z gives rise to different lines of isocompactivity which may not fit the simulation results of Fig. 3.7a so closely. Nevertheless, the close fit between theory and simulation deserves an explanation. It may be conjectured that ϕ_i determines a type of disorder quenched in the initial configuration that leads to systems with the same compactivity but different volume fractions and coordination numbers, evidenced by the results. This empirical result can be used to control the compactivity of the packing, at least for this particular protocol, defining a "granular compactimeter". Laboratory measurements of compactivity usually involve indirect measures through Fluctuation-Dissipation relations between fluctuations and response functions [20, 56, 8]. However, there is no simple "compactimeter" to measure this observable directly in a packing. These results can be used to, at a minimum, define packings with equal compactivity. The empirical identification of X with ϕ_i promotes the possibility of controlling X within this particular protocol, an important step in any thermodynamical analysis.

The advance of a granular thermodynamics crucially depends on the invention of a thermometer that can easily measure the compactivity, as in Fig. 3.8. A zero-th law of thermodynamics presents serious challenges in granular materials since there is no straight forward way to define a compactivity bath or reservoir.

The present theory predicts the dependence of the volume fraction, $\phi(X)$, on

Figure 3.8: Measuring the temperature of sand. Pictorial representation.

the compactivity, allowing for the development of a compactimeter: Such a device consists of a known granular medium, having a given μ and therefore coordination number. The compactimeter is inserted in a granular system and the entire system is shaken to allow for equilibration at a common compactivity. The compactimeter has a flexible membrane that allows volume transfer between both systems in contact. The volume of the system in the compactimeter will adjust accordingly and the compactivity can be read directly from the scale attached to it through the equation of state provided by the theory.

The foundation of the above compactimeter relies on the validity of a zero-th law for granular thermodynamics that determines the equilibration at a given compactivity of a system: Two systems in contact should mechanically equilibrate at the same compactivity. The test of the zero-th law is difficult to facilitate without theoretical guidance. Thus, it will be useful to perform the following test, either numerically or experimentally to test not only the idea of equilibration but also the possibility to describe granular matter under the V-ensemble. Such a test has been labelled the ABC experiment as proposed by Edwards [39], which is now possible to perform using the phase diagram.

Two packings are numerically prepared at points A and B in the Fig. 1.4 for different μ, $\mu_{\rm A} < \mu_{\rm B}$. The systems are equilibrated at different compactivities $X_{\rm A} < X_{\rm B}$, as indicated in the figure. They are then put into contact through a flexible membrane, or by simply putting the particles at the surface in contact, and allow the full system to mechanically equilibrate by gently shaking the system. The total volume is kept fixed and the volumes of the subsystems should change accordingly, $V = V_A + V_B$. If the AB system equilibrates at the same compactivity, then it will follow the trajectory depicted in Fig. 3.9 towards the point C of equilibration along the isocompactivity line. This will provide an important test for the V-ensemble and compactivity to describe jammed matter, as well as the validity of the phase diagram.

Another intriguing possibility would be to mix a frictionless A packing with an infinite friction B packing, which can be achieved numerically. This system would provide the maximum difference between the isolated packings, allowing study of the zero-th law with more accuracy. The frictionless packing is independent of

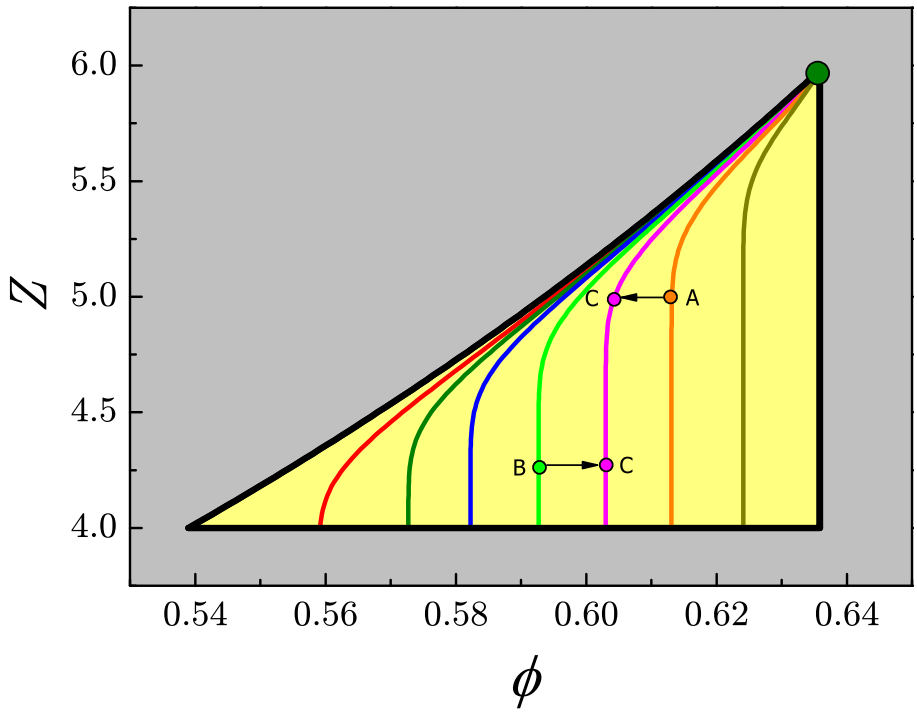

Figure 3.9: Sketch depicting a possible ABC experiment to test the zero-th law of granular thermodynamics and the validity of the phase diagram for finite compactivities. For intermediate frictions, the A and B systems should follow the arrows to C when put into contact and allow to interchange volume by gently shaking, as indicated in the figure.

X. Therefore, it should remain at the J-point. The $\mu \to \infty$ packing should, in principle, equilibrate at any X or volume fraction along the G-line. Most probably, it would stay put at the L-point since the A and B packings are joined by the isocompactivity infinite line. In any case, the resulting AB packing should fall inside the phase diagram if the theory is correct. If it does not equilibrate (falling outside the phase diagram) it will indicate the breakdown of the approach. Two conclusions could be reached from the failure of such a test. Either the V-ensemble is wrong or the approximations of the V-ensemble theory are not correct. In the latter, more sophisticated theories should be developed. If the former case occurs, then a different ensemble will have to be considered beyond isostaticity.

3.7.5 Microscopic states versus mesoscopic states

The distinction between microscopic and mesoscopic implies an intrinsic difference between the current mesoscopic theory, Eq. (3.19), and the full Edwards' statistics given by Eq. (3.5). A very tentative scenario is as follows. The entire entropy S could be separated into two parts as $S = S_{\text{meso}} + S_{\text{micro}}$ respectively, in terms of the different length scales. For the frictionless packing S_{meso} vanishes and then $S = S_{\text{micro}}$ and the microscopic compactivity $X_{\text{micro}} \equiv \frac{\partial V}{\partial S_{\text{micro}}}$ is equivalent to the Edwards compactivity: $X_{\text{Edw}} \equiv \frac{\partial V}{\partial S_{\text{Edw}}}$. Thus, one compactivity $X_{\text{micro}} = X_{\text{Edw}}$ is needed to describe the jamming point in the frictionless case. The frictional case is more complicated since both mesoscopic and microscopic entropies play important roles. The fact that there exist packings beyond the predicted mesoscopic volume fraction of RCP with $S_{\text{meso}} = 0$ implies that there must be another compactivity to describe at least these packings. Thus, a two-compactivity scenario is suggested

based on the separation of microscopic and mesoscopic length-scale, which is different from the Edwards/one-compactivity scenario valid for frictionless grains. The FDT then provides a formalism to test the fluctuations and measure both compactivities which is written according to different scales:

$$\begin{aligned} \langle \Delta V_{\text{micro}}^2 \rangle &= X_{\text{micro}}^2 \frac{\partial \langle V \rangle}{\partial X_{\text{micro}}} \\ \langle \Delta V_{\text{meso}}^2 \rangle &= X_{\text{meso}}^2 \frac{\partial \langle V \rangle}{\partial X_{\text{meso}}}, \end{aligned} \tag{3.29}$$

and the total volume fluctuation

$$\langle \Delta V^2 \rangle = (X_{\text{micro}}^2 \frac{\partial}{\partial X_{\text{micro}}} + X_{\text{meso}}^2 \frac{\partial}{\partial X_{\text{meso}}}) \langle V \rangle. \tag{3.30}$$

Experimentally, the compactivities could be accessible by the intensity of tapping. The microscopic states have smaller "volume" barriers than the mesoscopic states, thus they should be accessible via very gentle tapping that do not change the global Z, while stronger tapping would give the mesoscopic states. Chapter 5 further explores the idea of a mesoscopic and microscopic contribution to the entropy of a jammed packing.

3.7.6 Geometrical versus mechanical coordination number: measuring the behavior of quasiparticles

A quasiparticle is a mathematical entity that is, in principle, impossible to isolate from the structure of a real packing prepared either with MD computer simulations or experiments, rendering the measurement of their properties from real packings

difficult. This is because real packings already contain the ensemble average, and the ensemble cannot be dissociated, with the Boltzmann distribution of states, compactivity and density of states, from the isolated statistics of a quasiparticle.

Quasiparticles can be tested by preparing random packings with prescribed geometrical coordination number. However, approximate properties may be obtained from real packings in the limit $X \to \infty$ and $h_z \to 0$ based on the following observations: First, when $X \to \infty$ the Boltzmann factor is one, and the average in the partition function is flat over the configurations up to the density of states. Furthermore, the density of states is found to be a very fast decaying function of z. These two results imply that along the RLP-line of real packings (either numerical or experimental) one can obtain fully random packings which could reveal the properties of the quasiparticles.

Numerically, the quasiparticles size is of the order of two particle diameters. Once averaged over this range, z ranges approximately between $(Z, 6)$. In fact, an even more narrow distribution is found than theoretically expected, due to the fact that z is defined without the microscopic fluctuations but including the mesoscopic fluctuations. Once averaged over its neighbors, the microscopic fluctuations are completely removed in addition to partially removing the mesoscopic ones. In the limiting case of no mesoscopic fluctuations, when $X = 0$ along the RCP line, a very narrow distribution at $z \approx 6$ is found for any value of Z and μ, after averaging z over a mesoscopic region of two particle diameters. The distribution is even narrower when z is coarse-grained over a region of four particle diameters.

The X-ray tomography experiments of Aste [55] (Fig. 6a) reveal the trend predicted by Eq. (3.7) between the inverse of the Voronoi volume and the number

of neighbors of a set of Voronoi cells with similar volumes. However, it is evident from the figure that such number of neighbors is spanning a range of values between ~ 4 and ~ 10. The reason why the Aste's group [55] found a wider range of z is possibly due to the fact they did not consider a range of coarse-graining.

3.8 Conclusions

The final result of the phase diagram, the characterization of RCP and RLP using the compactivity, the role of friction in the determination of the limiting packings are interesting results, almost independent of the theory. The distinction between the geometrical and mechanical coordination number is also important, allowing for the implementation of averages in the partition function. Mathematically, the microscopic volume function and the formula obtained for the Voronoi cell in [40] are important and exact results which are the foundation of all work presented herein.

While the predictions Eqs. (3.21) and (3.23) of RCP and RLP approximate very well the known values, they are obviously not exact expressions, since they are based on several approximations of the statistical theory of volumes. Thus, the implementation of the mesoscopic volume function and the probability distribution of volumes on which these results are based are, perhaps, the points where improvements may be necessary. While the $\frac{2\sqrt{3}}{z}$ formula reproduces the average volume fraction surprisingly well, it is based on approximations to calculate the probability distribution of volumes as explained in [40].

Other approximations that require additional attention are the considerations

leading to the density of states $g(z)$. While the main results of RCP and RLP are nearly independent of the particular form of $g(z)$, other quantities such as the entropy and the equations of state for finite nonzero compactivity are more sensitive to it. By a direct measurement of the entropy, $g(z)$ can be calculated and compared to the simple exponential form used in the present study, and will be addressed in the next chapter.

Furthermore, crystal states are explicitly removed from the calculations by considering the upper bound of $z = 6$. A more general theory is needed then to investigate the transition from the RCP to the FCC as crystals starts to form in the system. Such a theory will include not only disordered states but also partially crystallized states and would give $X = 0$ at FCC following the full Edwards partition function, Eq. (3.5). Whether this disorder/order transition is critical or not is an interesting question which is under investigation. The present theory provides some ideas on how to proceed. The study of the distributions of local packings with a fix geometrical coordination number may provide some ideas to understand this problem.

Using Edwards statistical mechanics has elucidated some aspects of RLP and RCP in the disordered spherical packing problem herein. The numerical results suggest a way to experimentally test the existence of the predicted packings. By allowing the grains to settle in liquids of varying density, the speed of the particles can be varied and a systematic exploration of the jamming phase diagram can be achieved. Beyond the elucidation of some questions in the sphere packing problem, other problems can now be addressed systematically from the point of view of what has been learned from the phase diagram. This includes the investigation

of the criticality of the jamming transition from frictionless to frictional systems by extending the phase space to (ϕ, Z, σ), and generating packings away from the isostatic plane by isotropically compressing the packings generated in the plane of Fig. 3.3. Previous studies have focused on the frictionless point and on fixed friction. It is important to sample all the phase space for different friction and compactivities according to the preparation protocols explained above.

Previous results find power law scaling [64, 65, 63, 72] where the stress vanishes as $\sigma \sim (\phi - \phi_c)^{\alpha}$. A possible scenario is an extended phase diagram in the 3-dimensional space (ϕ, Z, σ), which could be tested numerically and experimentally. All the results presented herein study refer to the isostatic plane at the jamming transition $\sigma = 0$ or hard sphere limit. As soft sphere packings are compressed, different planes of $\sigma = \text{constant} \neq 0$ will be obtained. These compressed states are described not only by the compactivity X but also the angoricity A through the full partition function in the VF ensemble, Eq. (3.2). Preliminary results indicate that there seems to be evidence of criticality as the isostatic plane is approached when $\sigma \to 0$, although with exponents dependent on friction as well as the value of the compactivity.

The phase diagram introduced here serves as a beginning to understand how random packings fill space in 3d. The comparative advantage of the present numerical approach over extensive work done in the past, is in the classification of all packings through X, Z and ϕ in the theoretical phase diagram from where these studies could be systematically performed. This classification guides the search for indications of jamming from a systematic point of view, through the exploration of all jammed states from $\mu = 0$ to $\mu \to \infty$.

The next chapter will introduce another method of calculating the entropy of jammed matter using information theory.

Chapter 4

Entropy of Network Forming Materials

4.1 Shannon Entropy

Here, the work of Vink and Barkema [81] is presented to introduce the configurational, or Shannon, entropy.

A common computational procedure to estimate the entropy S at temperature T_2 is to measure the energy E as a function of temperature and then to integrate from a temperature T_1 at which the entropy is known

$$S(T_2) - S(T_1) = \int_{T_1}^{T_2} \frac{1}{T} \frac{\partial E}{\partial T} dT, \tag{4.1}$$

This process, however, requires sampling a large number of ensembles, and can therefore be applied only to systems with fast dynamics. Further, granular systems have no thermal energy to speak of, making such an integral immaterial.

A different approach, from information theory, is the Shannon entropy calculation. It is commonly explained in the context of a string of n bits. In this case, the Shannon entropy $H(n)$ is defined as:

$$H(n) = -\lambda \sum_i p(i) log_2 p(i), \tag{4.2}$$

where the index i runs over all possible bit sequences of length n and $p(i)$ is the probability of sequence i occurring. Also note that λ, the equivalent of the Boltzmann constant, is assumed to be unity. A further concept is the entropy density s of a large string of N bits, as $H(n)$ is an extensive quantity, its density will be intensive:

$$s = \lim_{n \to \infty} [H(n+1) = H(n)] \tag{4.3}$$

A procedure for estimating s for long string of bits is to extract from it a large number, m, subsequences, each containing n bits with $n < N$. An estimate for the probabilities $p(i)$ is given by

$$p(i) \approx f_i/m, \tag{4.4}$$

where f_i equals the number of times subsequence i was observed. For systems in equilibrium it can be shown without extensive calculation that the Shannon entropy is equivalent to the thermodynamic entropy, apart from a meaningless constant. The Shannon entropy is therefore estimated to be

$$H^*(n) = -\lambda \sum_i p(i) \ln p(i), \tag{4.5}$$

where $H^* \to H$ as $n \to \infty$.

To determine the configurational entropy of a network forming material, choose a large number, m, of random positions in the simulation cell. In the present study, the network could be a contact network, a Delaunay triangulation, or some other complete covering of the granular or compressed emulsion system. For each randomly chosen position one finds the nearest n particles and identify the graph formed by the bonds connecting these particles. Further, a label is assigned to this graph, based on the graph automorphism. This implies that different labels are assigned to sets of atoms with different bonding topologies, but renumbering the atoms does not yield a different label. The number of times a graph is observed is counted and the above approximate probability estimate to obtain a probability of occurrence. A value of $H(n)$ is then determined, though this value will be somewhat underestimated as it does not explore all possible graphs with finite m. However, a small displacement of one of these random positions will usually result in exactly the same list of n nearest particles and thus the same graph, resulting in an approximate upper bound to the number m of random positions that one should choose in a simulation cell containing N particles. The literature suggests this upper bound is obtained from the typical distance over which a random position can be displaced without altering the selected graph, resulted in a 3D upper bound of $m = 3.4n^2N$. The present studies have shown however that this remains an underestimate for appropriate convergence.

The Shannon entropy procedure must take into account that the number of

different graphs observed gets multiplied with a factor proportional to approximately n^{d-1}. This results in a correction to $H(n)$, $g(n) = (d-1)ln(n)$, where d is the dimensionality of the network. The latter can be verified in crystalline networks, such as cubic or FCC, where the configurational entropy must be zero. The present study will utilize more exact terms for $g(n)$, acknowledging that the given equation for $g(n)$ may be too general for accurate estimations of $H(n)$.

Graphs with $p(i)$ smaller than $1/m$ will likely be observed only once, if at all. This finite-size effect grows with increasing n, as graphs become very complex. The quantity $H_1(n)$ is defined as the contribution to $H(n)$ of the topologies observed once. Measurements where $H_1(n)$ exceeds a threshold percentage of $H(n)$ are not considered to be valid measurements.

In an effort to improve convergence, and thereby decrease simulation time for the calculation of the configurational entropy, a finite sample correction is applied. The details of this correction are presented here, as given in the master's thesis of Paul Rombouts [82].

Referring now to H^* from above, the probability $P_i(f_i)$ that a certain state i will be observed exactly f_i times is given by the binomial distribution

$$P_i(f_i) = \binom{m}{f_i} p_i^{f_i}(1-p_i)^{m-f_i}. \tag{4.6}$$

Define the probability of a certain event to be p and the number of observed events to be m. Furthermore let $F(x)$ be a function that can be Taylor expanded around p:

$$F(x) = F(p) + F'(p)(x-p) + \frac{1}{2}F''(p)(x-p)^2 + ... \tag{4.7}$$

The binomial distribution is concentrated around the average $\langle f_i/m \rangle = p$, and we obtain the following useful approximation

$$\langle F(\frac{f_i}{m}) \rangle = F(p) + F'(p)\langle \frac{f_i}{m} - p \rangle + \frac{1}{2}F''(p)\langle (\frac{f_i}{m} - p)^2 \rangle + ... = F(p) + \frac{1}{2}F''(p)\frac{p(1-p)}{m} + ..., \tag{4.8}$$

Let $F(x) = -x \log x$, an obvious choice considering the form of the Shannon entropy. Then, $F''(x) = -1/x$ and

$$\langle F(\frac{f_i}{m}) \rangle = -p \log p - \frac{1-p}{2m}, \tag{4.9}$$

Therefore,

$$\langle H^* \rangle = \sum_i \langle F(\frac{f_i}{m} \rangle = -\sum_i p_i \log p_i - \frac{\sum_i (1-p_i)}{2m} + ... = H - \frac{k-1}{2m} + ..., \tag{4.10}$$

The Shannon entropy is then the calculated entropy from simulation, H^*, plus the binomial correction term $(k-1)/2m$, a term clearly tending to zero as m tends to infinity. This approximation works well under two conditions. First, $mp \geq 1$, in order to allow the Taylor expansion to converge. Second the contribution of the probabilities below $1/m$ to the Shannon entropy must be a practically insignificant term. If this is not the case, additional binomial correction terms must be used. However, these terms will not be independent of p_i, therefore making the calculation significantly more complicated. It is of interest in the present work to ensure that both conditions necessary for the use of only the first term of the binomial

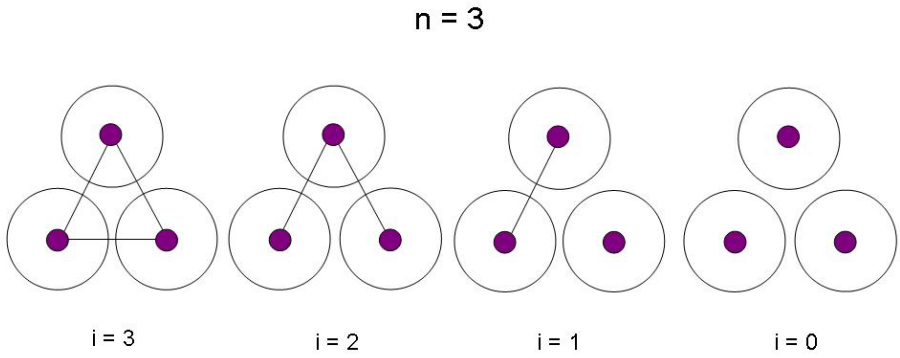

Figure 4.1: Classes of graphs for n=3. There are only 4 possible graphs, 0 contacts, 1 contact, 2 contacts, or 3 contacts.

correction are applicable.

A simple example of graph classes can be seen when $n = 3$. Figure 4.1 shows exactly 4 possible graphs that can be achieved, consisting of $0, 1, 2$ and 3 connections between 3 Delaunay contacts. Each graph falls into a class of $i = 1 \rightarrow 4$. The random process of selecting a graph with $n = 3$ is done m times, continuously calculating the probability of f_i, as defined in Eq. (4.4).

Assuming the above described binomial distribution of the probability of having a cluster of class i observed exactly f_i times, the first order finite sampling correction to H^* therefore results in

$$\frac{H(n)}{\lambda} = \frac{H^*(n)}{\lambda} + \frac{k-1}{2m}. \tag{4.11}$$

To include the crystal correction, we redefine the Shannon entropy as follows:

$$\frac{H'(n)}{\lambda} = \frac{H(n)}{\lambda} - g(n), \tag{4.12}$$

and the entropy density is

$$s = \lim_{n\to\infty}[H'(n+1) - H'(n)]. \tag{4.13}$$

4.2 Application to Emulsions

Here, an experiment is reviewed wherein the Shannon entropy calculation is realized in an emulsion.

Pouring sugar into a cup is the simplest example of a fluid to solid transition which takes place because of an increase in the systems density, identified as the jamming transition [26]. If the particles are deformable, the applied stress is also an important control parameter for jammed systems as the density increases with the applied load [63]. When the density is high enough to support an external weight without the constituent grains starting to flow and rearrange, the material has the properties of a solid and is known to be at the isostatic limit. This state arises when the particles have enough contacts between them such that all the forces balance according to Newton's equations [62]. The average number of contacts per particle, $\langle Z \rangle$, known as the coordination number, is therefore the key parameter that determines the mechanical properties of granular materials. Theory predicts that a system of frictionless spherical particles has a minimal average number of contacts for mechanical stability $\langle Z \rangle = 2D$ [67], where D is the dimension of the system.

The problem with jammed matter, from sand piles to mayonnaise, is that it is difficult to take a look inside the particulate packing to measure Z. Indeed, in the

old days Mason, a postgraduate student of Bernal, took on the task of shaking glass balls in a sack and "freezing" the resulting configuration by pouring wax over the whole system. He would then carefully take the packing apart, ball by ball, noting the positions of contacts for each particle [43]. Since this labor-intensive method patented half a century ago, yet still used in recent studies [83], other groups have extracted data at the level of the constituent particles using X-ray tomography [84]. However, neither method could directly determine the contacts in order to be sure whether the particles were touching or just very close together. Moreover, these methods only provide insight into large particles and do not lend themselves to the exploration of jammed matter on the colloidal length scale. Given the recent boom of theories unifying the concepts in granular materials and glasses [26], the characterization of all jammed matter is important for the advancement of this field.

Here, a different method highlights the contacts between droplets in a dyed jammed emulsion. While previous experiments were based on the visualization of the areas of droplet deformation [60, 59], here the origin of the enhanced fluorescence at the contacts is explained in terms of the polarity of the environment of the dye. Since the dye has amphophilic character it preferentially sits at the oil-water interface, where its emission wavelength band is blue-shifted compared to the emission of the same dye in the oil droplet core. As two droplets touch on length scales below the resolution of the microscope, the concentration of these interfacial dye species increases, giving rise to highlighted areas of contact that can then be identified.

Emulsion system - The model system to study jammed matter is a transparent

emulsion. It consists of fluorescently labelled silicone oil droplets with Nile red dye, suspended in a solution of 1:1.05 water to glycerol volume ratio to ensure refractive index matching between the droplets and the continuous phase [60]. This emulsion system is stabilized by Sodium Dodecyl Sulfate (SDS) surfactant, at 10mM concentration, i.e. below the critical micellar concentration (CMC), thus avoiding depletion attraction between the droplets [85]. A crude emulsion was first made by rapid mixing of the two phases in the presence of surfactant, after which the droplet size distribution was refined using the narrow gap shear method [86] to yield a radius distribution of $2 \pm 0.7\mu$m, shown in Fig.4.2. The emulsions were characterized using a laser scanning confocal microscope (LSCM, Zeiss). The droplet radii were measured with subvoxel accuracy from the 3D confocal images containing 1869 droplets using image analysis techniques developed in [60]. The emulsion serves as a model for a granular material composed of soft spheres, which can be considered frictionless due to the lubrication by the continuous phase fluid.

Average coordination number - From the detection of contacts, via spatially resolved confocal microscope images (see Fig 4.3, now compute the average number of contacts per particle. With N frictionless particles in dimension D, one has ND Newton equations and $N\langle Z\rangle/2$ unknowns corresponding to the normal forces between droplets. For the system to be solvable, it requires $\langle Z\rangle = 2D$. In 3 dimensions, this leads to $\langle Z\rangle = 6$, the isostatic limit. Experiments to measure this coordination number have been performed on grains. For instance, Bernal [43] found $\langle Z\rangle = 6$, while for frictional grains the prediction is $\langle Z\rangle = D + 1 = 4$ [63]. Additionally, molecular dynamics simulations have shown that $\langle Z\rangle$ can

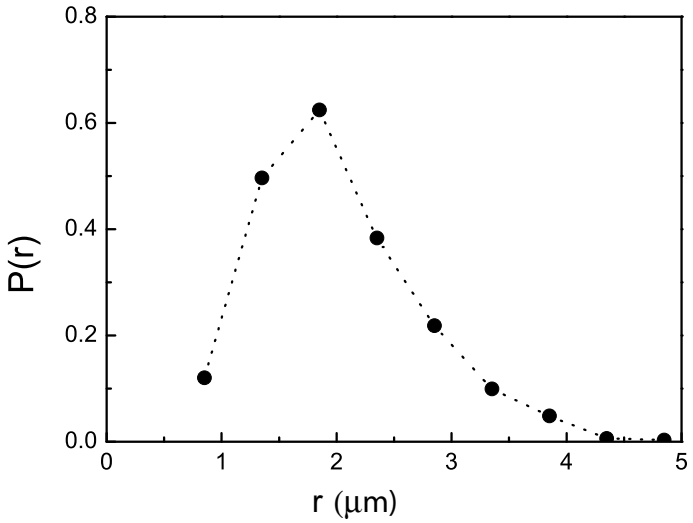

Figure 4.2: Radius (in microns) distribution of 1869 emulsion droplets, obtained from a Fourier Transform 3D image analysis of the confocal microscope images.

be a function of the friction coefficient, reducing smoothly from 6 as friction is introduced [65]. It is therefore interesting to measure this quantity in a truly frictionless case. A 3D image analysis technique is employed to measure the droplet radii and positions with subvoxel accuracy, as well as the contact areas between those droplets that exert forces on one another. Due to the polydispersity of the system, the droplet volume fraction for six such images is calculated to be $\phi = 74\%$ at the applied pressure of $\sigma = 4.5Pa$ per droplet, since the droplets are able to pack more efficiently than their monodisperse counterparts. Within these packings an inner window is identified where all the neighbouring droplets have been identified and run a coordination number analysis on 1544 such droplets. A contact is considered when the area of deformation is larger than the resolution limit of the technique.

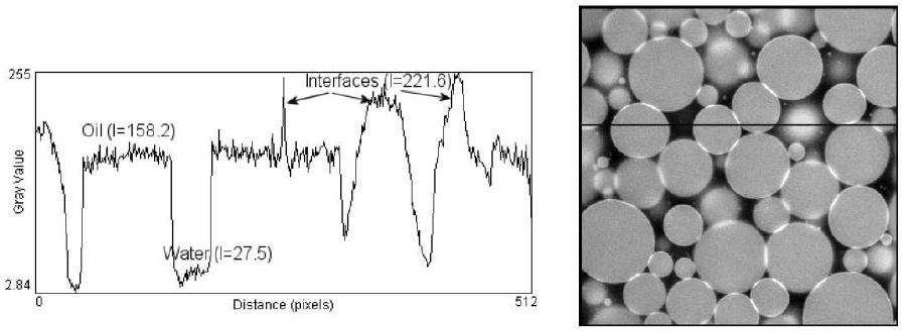

Figure 4.3: (a) Intensity profile along the black line of image (b), indicating the enhancement at the droplet contacts.

The distribution of Z is represented in Fig. 4.4a. The mean value extracted from this distribution is $\langle Z \rangle = 6.08$, in close agreement with the theoretical value of 6. The slight excess of contacts can be attributed to the pressure exerted on the system. Note that the distribution $\mathrm{P}(Z)$ exhibits an exponential tail due to the polydispersity of the particles which enables a more efficient packing, but despite this large polydispersity, the average value of 6 still holds. This provides experimental evidence for the prediction $\langle Z \rangle = 2D$, for the case of frictionless particles at the colloidal length scale.

Entropy considerations - Determining the entropy through the statistics of volumes, as suggested in numerous theoretical works [34, 53], would require the knowledge of the density of states, which is still an open issue. Therefore, the above alternative method is used to characterize the states of the system via graph theoretical representations and compute the entropy density s using information theory (Shannon entropy) [87, 81]. To achieve this, knowledge of the contact positions is used to build the corresponding network. In this representation, a cluster of n

droplets is simply a graph which, by means of graph automorphism [88], can be transformed into a standard form (also known as "class") so that two topologically equivalent graphs belong to the same class. A given class i can then be considered as a state with an occurrence $p(i)$.

The result is shown in Fig. 4.4b. At large n, H clearly suffers finite size effects, but the existence of a linear regime for intermediate values of n demonstrates the rapid convergence of Eq. (4.3). The fact that there is a regime (between $n = 6$ and 10) where the entropy is proportional to the number of particles per cluster indicates that entropy is an extensive property and the entropy density is constant and well-defined. Moreover, this linear regime happens at lower numbers of particles per cluster than what has recently been observed in two-dimensional granular materials [58]. The entropy per grain is then given by the slope of the linear section of the graph, giving $s \simeq 1.4$ (in units of λ). Beyond this value, the method shows that the cluster entropy is equivalent to system entropy, enabling us to determine an entropy as a function of the control parameters, such as the density of the system.

To conclude, an experimental technique for getting through a jammed system in a matter of seconds is presented, giving direct access to contact positions. This method opens the way for further studies, such as the calculation of coordination number, entropy and pressure as a function of volume fraction, in order to reach an equation of state for jammed systems [63].

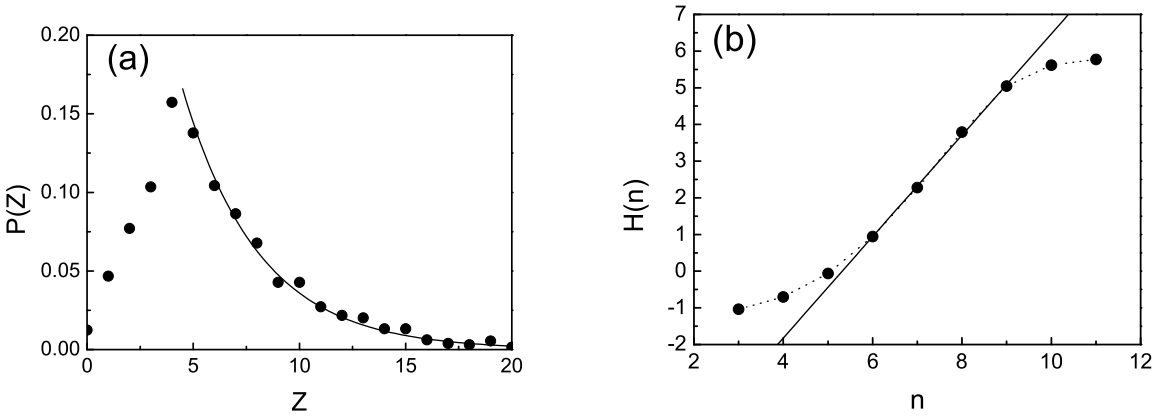

Figure 4.4: (a) Distribution of the number of contacts per particle, Z. The mean value is $\langle Z \rangle = 6.08$. The solid line is an exponential fit of the tail of the distribution. (b) H as a function of the cluster size n.

Chapter 5

Jamming III: Entropy of Jammed Matter

5.1 Introduction

Jamming has since been characterized by innumerable studies, yet fundamental questions remain unanswered, including: What is a jammed state and how to characterize its state of randomness? While a minimum requirement for jamming is that the particles should satisfy mechanical equilibrium, such a condition is not sufficient for a jammed state which must be stable under perturbations and macroscopically reversible [34]. In an attempt to define the jammed states in a rigorous way, Torquato and coworkers have proposed three categories of jamming [74]: locally, collectively and strictly jammed. This problem is intimately related to the existence of well-defined upper and lower limits in the density of disordered packings; random close packing (RCP) and random loose packing (RLP) [43]; a

longstanding open question in the field. A definition of RCP requires proper definitions of *jammed states* and the concept of *randomness* [61]. Indeed it was conjectured [61] that the RCP concept could be replaced with the maximally random jammed (MRJ) conception in terms of an ensemble of order parameters.

Previous definitions of jamming are based purely on geometrical considerations, sufficient to describe frictionless grains [74] but not for granular materials where friction dominates [66]. Fig. 5.1 illustrates the point: a frictionless hard sphere system is not locally jammed if only normal forces are considered, since the ball can freely move in the vertical direction. The same geometrical configuration is locally jammed if friction is allowed between the particles, revealing the importance of forces in the definition of jamming for frictional particles. Other approaches based on the potential energy landscape [64] fail for granular materials, as such a potential does not exist for frictional grains due to their inherent path-dependency. Thus, the definition of the jammed state for granular materials must consider inter-particle normal and tangential contact forces beyond geometrical constraint.

This study follows an alternative approach to characterize jamming and the degree of randomness for the general case of frictional hard spheres. The framework is rooted in statistical mechanics [34] and considers the definition of jamming at the volume-force (V-F) ensemble level [34] through force and torque balance conditions. First, frictional packings of granular spheres are investigated at the jamming transition generated via computer simulations to compute the equations of state, entropy and compactivity, as a function of volume fraction, ranging from RLP to RCP. The entropy is calculated by two methods. First, a direct analysis of volume fluctuations explores the clustering of microscopic volumes. Second,

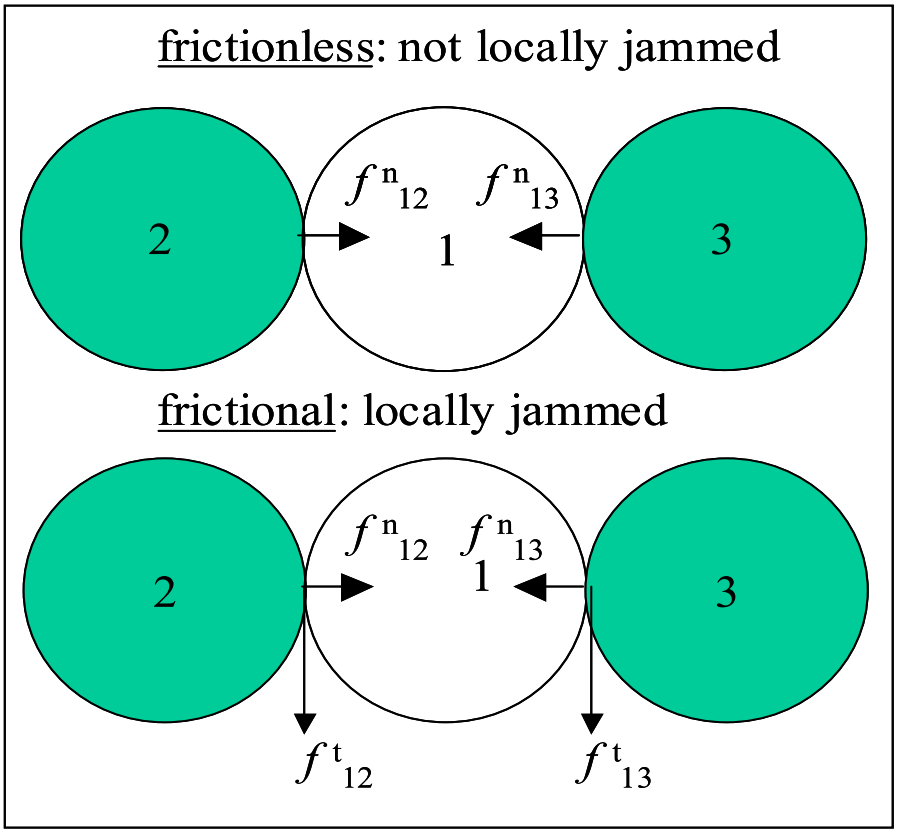

Figure 5.1: Numerical results. (a) The inset shows a ball in 2d under mechanical equilibrium by two nearest neighbor contacts. The ball is not jammed under a normal force interaction. It jams only when tangential forces are present.

graph theoretical methods using the Shannon entropy analyze the network forming properties of the granular system. Simulations show that random loose packings are more disordered and have higher compactivity than random close packings. The concept of randomness is well-defined for the V-F ensemble following the Gibbs distribution [34], which is different from the measurement of randomness of single packing in term of the ensemble of order parameters [61]. Mechanical equilibrium imposes an average coordination number, Z, larger or equal than the minimum isostatic coordination as conjectured by Alexander [67] (see also [90, 63, 64, 66, 65, 91]) defining the $Z-$ensemble at the mesoscopic level. Calculations are done under the quasiparticle approximation of [40] giving rise to a mesoscopic configurational entropy, achieving a minimal value at the volume fraction of RCP and maximal value at the minimum RLP limit. The results define RCP and RLP at the mesoscopic level and are in general agreement with the simulations. They also suggest that the configurational entropy requires augmentation to include the entropy of the microscopic states neglected at the mesoscopic level.

5.2 Simulations and Results

5.2.1 Packing Preparation

The entropy of jammed granular matter is investigated by analyzing computer generated packings of 10,000 spherical equal-size particles of 100μm diameter. The details of such a protocol are extensively discussed in Chapter 3, and reproduced for packings of 1024 particles.

The Coulomb friction coefficient, μ, between the particles ranges from 0 to

∞ producing packings with coordination number varying from $Z \approx 6$ to $Z \approx 4$, respectively. There exits a common function $Z(\mu)$ over the different Γ and ϕ_i. For $\mu \to \infty$, ϕ ranges from the RLP limit $\phi_{\text{RLP}} \approx 0.55$ obtained when $\Gamma \to 0$ and $\phi_i < 0.54$ to the RCP limit $\phi_{\text{RCP}} \approx 0.64$ obtained for larger Γ and $\phi_i \to 0.64$.

For $\mu = 0$, the density is approximately $\phi \approx \phi_{\text{RCP}}$. For intermediate μ, the packings follow the phase diagram as obtained in [40].

5.2.2 Phase Diagram

Simple counting arguments, neglecting correlations between nearest neighbors, consider that a necessary condition for mechanical equilibrium is that the number of independent force variables must be larger or equal than the number of linear independent force/torque balance equations. Alexander [67] conjectured that at the transition point for frictionless spherical packings [67, 90, 52] the system is exactly isostatic with a minimal coordination, $Z = 2d = 6$ in 3d. Such a conjecture can be extended to the infinite friction case, where $Z = d + 1 = 4$ [92, 52]. In the presence of finite inter-particle friction coefficient μ, the analytic form of $Z(\mu)$ is very difficult to work out since the counting argument now involves nonlinear inequality constraints through the Coulomb condition. Despite the theoretical difficulty, there exists a dependency of Z between μ suggested by simulations [66, 65].

Fig. 5.2 shows the phase diagram used for all equation of state calculations presented herein, as obtained using the "split" algorithm as described above. As discussed in Chapter 3, packings along the RCP line are most difficult to obtain, especially those near the C point, suggesting a possible first order phase transition near the C point resulting in higher values of the lowest achievable stress for those

packings. The G-line, at $Z = 4.0$, indicates the theoretical Z for infinite friction packings. The grey line at $Z = 4.2$ indicates the approximate lowest achievable Z possible using the present "split algorithm". This further suggests a possible first order phase transition when approaching the G-line, not only in stress, but also coordination number. The solid lines in Fig. 5.2 are averages used in all following calculations, and are weighted away from those values obtained near the RLP and RCP lines. This allows us to use a constant value as an approximation for the mechanical coordination number.

This result is compared to the phase diagram as predicted by theoretical model asserted in [40], shown in Fig. 3.3. Note that the isostatic condition [67] predicts $Z = 6$, while Fig. 5.2 includes packings with $6 < Z \leq 6.2$, and $\phi > 0.634$ as predicted by the theory for RCP. These packings may be new microstates of jammed matter (indicated by the shaded portion of the phase diagram). While they remain a component of the ensemble generated via the above described simulation protocol, their existence remains a topic of ongoing study. Note that when compared to the phase diagram in Fig. 3.3, the phase diagram of Fig. 5.2 does not display the same accuracy with respect to averaging along lines of constant μ to obtain the mechanical coordination number. This seems due in part to the increase in system size from 1024 to 10,000, and such a finite size effect will be considered in future studies. Regardless, the results presented in Fig. 5.2 complete the phase diagram well enough for the proposed statistical analysis.

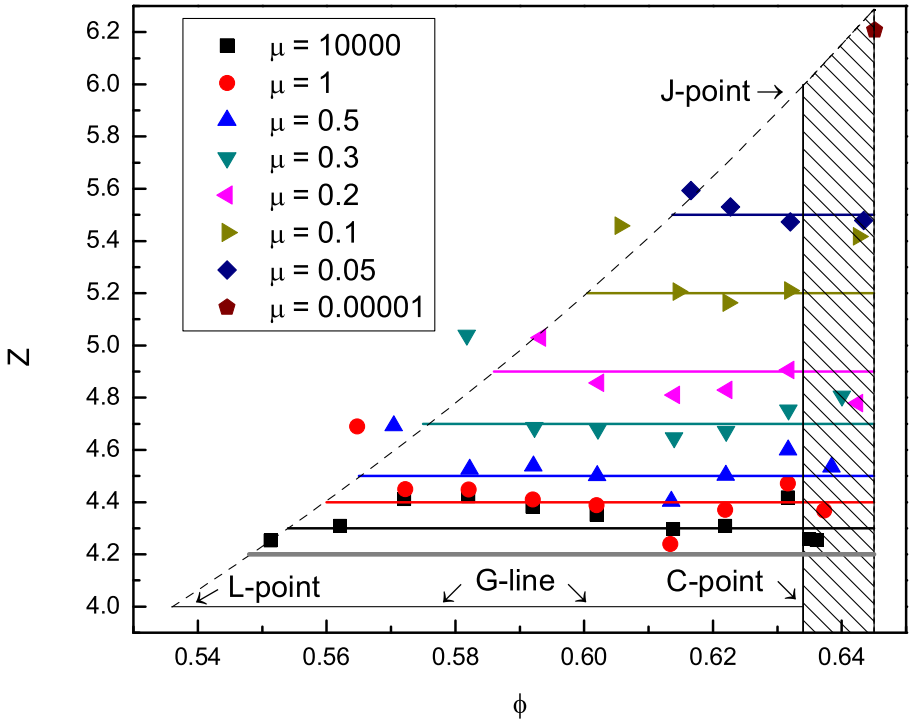

Figure 5.2: The phase diagram of jamming from simulation results. Horizontal lines show the average coordination number used for packings of constant μ. The dashed line represents the theoretical RLP line. The solid vertical line at $\phi = 0.634$ is the theoretical RCP line obtained in [40]. Notice that some packings exist to the right of the RCP line. Such packings are not captured by the theory, indicating that microscopic fluctuations beyond the mesoscopic theory of [40] are important close to the RCP state. The solid grey line at $Z = 4.2$ indicates the lower limit for Z available using the present split algorithm. The J-point, located at $(\phi, Z) = (0.634,6.0)$, is the theoretical frictionless jamming point. The L-point, located at $(\phi, Z) = (0.536,4.0)$, is the theoretical jamming point for $\mu \to \infty$ with minimal ϕ_i. The C-point, located at $(\phi, Z) = (0.634,4.0)$, is the theoretical jamming point for $\mu \to \infty$ with $\phi_i \to 0.634$. The G-line, $Z = 4.0$ is the theoretical average Z achieved for all infinite friction packings of identical spherical grains in 3d.

5.2.3 Entropy from Voronoi Volume Fluctuations

In the absence of energy conservation, a different statistical approach is necessary to describe the system properties of jammed granular matter. Along this line of research, Edwards [34] proposes replacing the system energy by the volume as the conservative quantity such that a canonical partition function of jammed states can be defined and a statistical mechanical analysis is plausible. Therefore, a microscopic volume must be associated with each grain.

As detailed in [40], the definition of a Voronoi cell is a convex polygon whose interior consists of all points closer to a given particle than to any other. Further, it is additive and tiles the system volume completely. Its formula in terms of particle positions for monodisperse spherical packings in 3d is

$$\mathcal{W}_i^{\text{vor}} = \frac{1}{3}\left\langle \left(\frac{1}{2R} \min_j \frac{r_{ij}}{\cos\theta_{ij}} \right)^3 \right\rangle, \tag{5.1}$$

where $\vec{r}_{ij}$ is the vector from the position of particle i to that of particle j, the average is over all the directions $\hat{s}$ forming an angle θ_{ij} with $\vec{r}_{ij}$ as shown in Chapter 3, and R is the radius of the grain. The Voronoi volume is used to tile the total system volume, and replaces energy as the conserved quantity in a new micro-canonical ensemble for jammed granular matter. Therefore, fluctuations in Voronoi cell volumes are related to the compactivity of the jammed system, much like energy fluctuations are directly related to the system temperature in equilibrium thermodynamics.

In practice, a trigonometric approach is used to determine the Voronoi cell associated with each particle i, thereby obtaining its Voronoi volume $\mathcal{W}_i$. Calculation

of a Voronoi cell volume begins by defining the polygon between two Delaunay contacts, having finite number, m, vertices. Delaunay contacts are defined by the network of grain positions and radii calculated using QHull software, available at http://www.qhull.org. The contribution of this polygon to calculating the Voronoi volume comes from the ability to associate a pyramid, comprised of the center of each particle as the apex, and the m-sided polygon as its base, as shown in Fig 5.3, to each particle. The two pyramids are symmetric. The volume of this pyramid is the contribution to the Voronoi volume of the cell surrounding a particle, exclusive to the particular Delaunay contact which shares the polygon base. Repeating this process for each Delaunay contact results in the complete Voronoi volume surrounding a particle. The Voronoi volume is thereby the microscopic volume associated with each grain. Note that one could obtain the exact same formulation for the microscopic volume per grain utilizing the analytical form of the Voronoi cell presented in [40].

A statistical analysis of the volume fluctuations is performed by considering a cluster of n particles. This cluster consists of a single particle, and its $n-1$ nearest neighbors, with volume $\mathcal{W}_n = \sum_i^n \mathcal{W}_i$. Studying fluctuations in single Voronoi cells is the microscopic fluctuation. Using such a clustering technique reveals fluctuations larger than those observed in the microscopic volumes, or individual Voronoi cells. As the theory presented in [40] focuses on a coarse graining over several particle diameters, in an effort to define a volume function, or "Hamiltonian", clusters of grains will more closely represent the fluctuations that the theory necessitates. Note that the RCP state is considered to have zero mesoscopic fluctuation. Therefore, the value of the Voronoi volume fluctuation density at RCP is subtracted

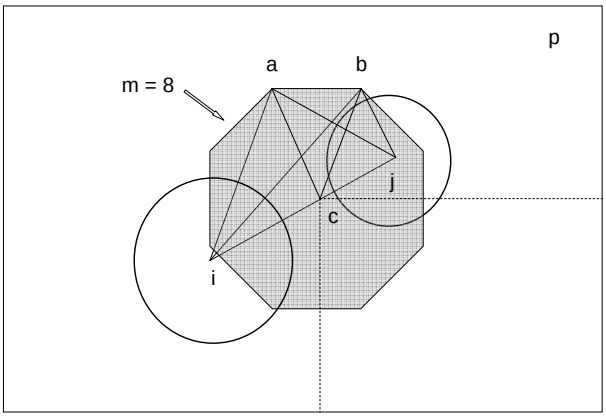

Figure 5.3: The line between the centers of particles i and j is defined by $\overline{ij}$, equivalent to r_{ij}. The plane perpendicular to the bisection of $\overline{ij}$ is defined by p, intersecting $\overline{ij}$ at point c. Plane p is intersected by $m-$ other planes, creating an m-sided polygon between particles i and j. Each plane intersecting plane p (not shown) is a plane bisecting $\overline{ik}$, the line between the centers of particle i (or j) and another particle k in the system, where k is one of m particular particles. A pyramid is thereby formed using the m-sided polygon as the base, and i (or j) as the apex. This pyramid is symmetric over plane p, and its volume is the contribution to the Voronoi volume of particle i from particle j, or vice versa, exclusively. The volume of the pyramid is calculated by separating the pyramid into 8 smaller pyramids, using the triangle composed of one of the m available sides, and c as its base and i as its apex. This is illustrated by using $\overline{ab}$ and c as the base of a pyramid with apex i. The volume of this pyramid is calculated and the process is repeated for each of the m sides, adding each obtained volume to the Voronoi volume of both i and j. The entire process is then repeated for all Delaunay contacts for a given particle, resulting in the total Voronoi volume for that particle.

from all values of the fluctuation density used herein.

The fluctuation relation is defined as follows:

$$\sigma_n^2 = \langle (\mathcal{W}_n - \langle \mathcal{W}_n \rangle)^2 \rangle = \lambda X^2 d\langle \mathcal{W}_n \rangle / dX \tag{5.2}$$

Equation (5.2) is analogous to equilibrium thermodynamics, replacing energy and temperature by volume and compactivity in the Edwards picture.

The average volume, $\langle \mathcal{W}_n \rangle$ is calculated and fluctuations $\langle (\mathcal{W}_n - \langle \mathcal{W}_n \rangle)^2 \rangle$, where $\langle \cdot \rangle$ is an average over many n-clusters. From the large n behavior the fluctuations as a function of ϕ are extracted for every packing studied. Figure 5.4 shows the fluctuations as a function of n for packings with infinite friction, displaying the largest range of volume fractions in the data used herein. For sufficiently large n, the fluctuations scale with n and therefore are extensive and well-defined.

Figure 5.5 shows the approximate value of n at which the extensive nature of the fluctuations reaches its maximal value, as a function of ϕ. Lower volume fractions, approaching RLP, require higher values of $n \approx 1000$ to achieve this condition. This result contrasts with the results of [58], although there the system was smaller, $n \approx 100$, and two-dimensional. For packings approaching RCP, the extensive nature of the fluctuations occurs at $n \approx 10\ 100$. Reference [58] acknowledges that if grain volumes can be treated as independent random variables, then the fluctuation in clusters of n Voronoi cell volumes should scale with n. For clusters of jammed grains, this is not observed, indicating the existence of correlations between the Voronoi cell volumes within a cluster. However, in this study, the value of n at which the fluctuations reach a maximal density is a function of ϕ_c, shown in Fig. 5.5. In [58], this phenomena is observed, but the density is

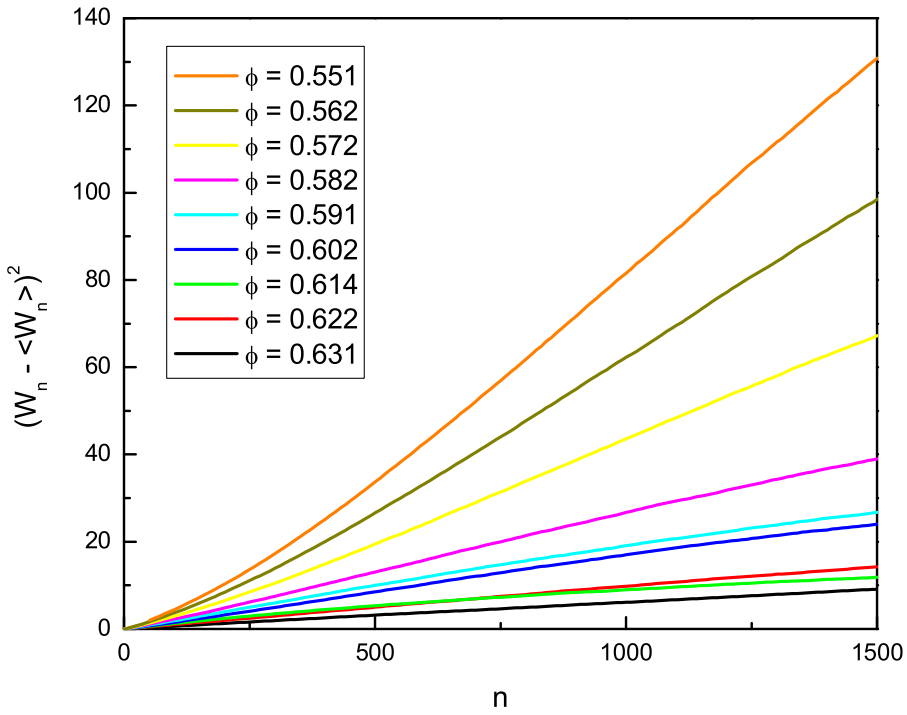

Figure 5.4: $\langle \Delta \mathcal{W}_n^2 \rangle$ versus n for packings with $\mu \to \infty$, with $Z \approx 4.3$, for different ϕ.

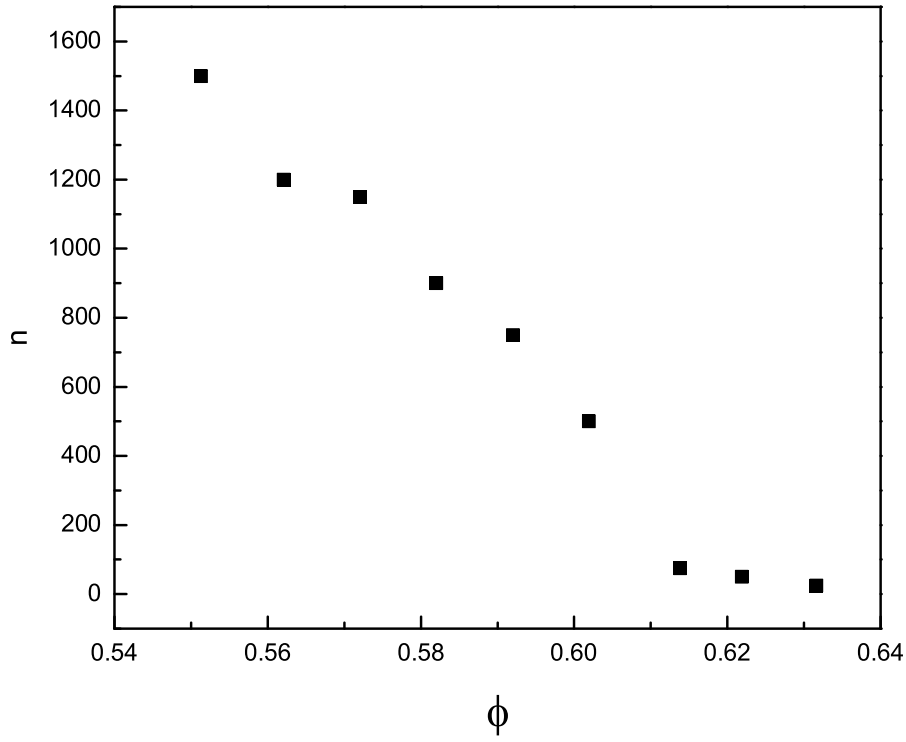

Figure 5.5: n vs ϕ showing maximal value of extensive nature. Values of ϕ are taken along $\mu \to \infty$, with $Z \approx 4.3$, to display largest range of ϕ.

apparently independent of the volume fraction, and occurs at the same value of n for each packing. Figure 5.6 shows the fluctuation density, $\langle(\mathcal{W}_n - \langle\mathcal{W}_n\rangle)^2\rangle_n$, or fluctuation per grain, as a function of ϕ for all packings used herein.

An important note is that this extensive relationship occurs well before n is large enough such that finite size effects of the system force the fluctuations to tend to zero. Further, the linear relationship extracted from n-clusters is different from that extracted from n randomly chosen Voronoi cells, implying a correlation between Voronoi cell volumes, revealed using the clustering technique. Analysis of

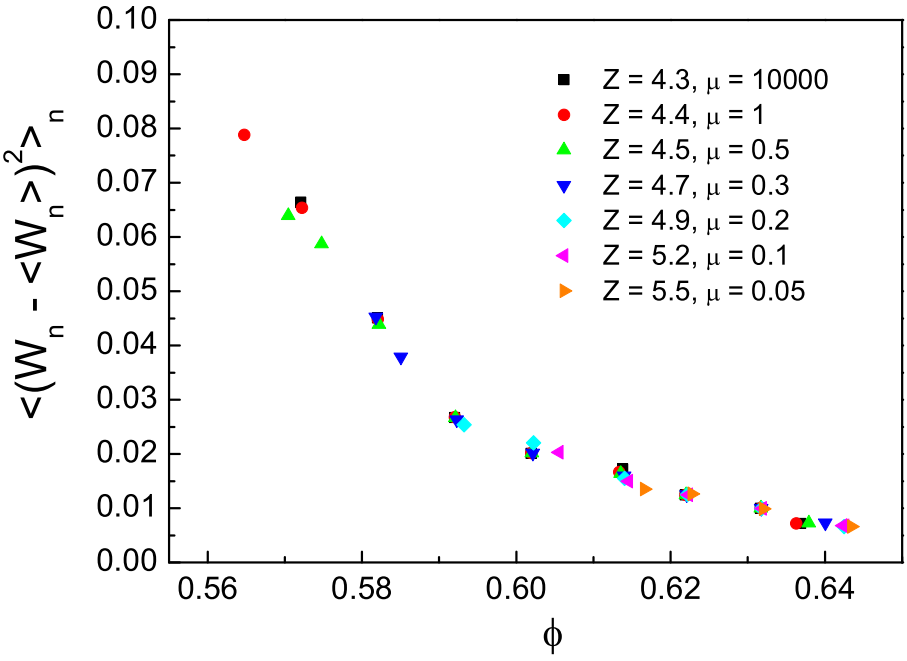

Figure 5.6: $\langle \Delta \mathcal{W}_n^2 \rangle_n$ versus ϕ.

the fluctuation density reveals the following formula:

$$\begin{aligned} \Delta\sigma_n^2 \equiv \langle (\mathcal{W}_n - \langle \mathcal{W}_n \rangle)^2 \rangle_n &= \frac{1}{2}((\sigma_{n+1}^2 - \sigma_n^2) + (\sigma_n^2 - \sigma_{n-1}^2)) \\ &= \sigma_1^2 + \langle \mathcal{W}_n \Delta\mathcal{W}_{n+1} \rangle + \langle \mathcal{W}_{n-1} \Delta\mathcal{W}_n \rangle \\ &- \langle \mathcal{W}_n \rangle \langle \Delta\mathcal{W}_{n+1} \rangle - \langle \mathcal{W}_{n-1} \rangle \langle \Delta\mathcal{W}_n \rangle, \end{aligned} \tag{5.3}$$

where σ_1^2 is the single particle, or microscopic, fluctuation in Voronoi volume, and $\Delta\mathcal{W}_{n+1} = V_{n+1}^{vor} - \langle V^{vor} \rangle$ is the $n+1$ free Voronoi volume to be added to the cluster of n Voronoi volumes being averaged. If volumes are chosen randomly, as opposed to the clustering condition, the fluctuation density collapses to the microscopic fluctuation density, as the correlation tends to *zero*. Therefore, the fluctuations will scale exactly with n, as indicated in [58]. Further, if the averaging process is

taken to be equal to or larger than the system size, then $\langle \Delta \mathcal{W}_{n+1} \rangle = \langle \Delta \mathcal{W}_n \rangle = 0$, such that Eq. (5.3) is rewritten as

$$\Delta \sigma_n^2 = \sigma_1^2 + \langle \mathcal{W}_n \Delta \mathcal{W}_{n+1} \rangle + \langle \mathcal{W}_{n-1} \Delta \mathcal{W}_n \rangle. \tag{5.4}$$

Equation (5.4) thereby provides an analytical form for the curves presented in Fig. 5.4, as a function of n. It remains a possibility that larger values of n, or large cluster sizes, overuse the available data, skewing the results for the fluctuation density. However, the minimum value for the fluctuation density is always the single particle fluctuation density, displaying a very similar scaling property to that of Fig. 5.6, only with smaller values. Using these smaller values does not greatly impact the equations of state presented herein.

Compactivity.—The compactivity is then obtained via the integration of the Eq. (5.2):

$$X^{-1} = \lambda \int_{\phi(X)}^{\phi_{\mathrm{RLP}}} \frac{d\langle \mathcal{W}_n \rangle}{\langle (\mathcal{W}_n - \langle \mathcal{W}_n \rangle)^2 \rangle}, \tag{5.5}$$

where $\phi(X \to \infty) \to \phi_{\mathrm{RLP}}$ and λ is the analogue of the Boltzmann constant that defines the units of compactivity. Since Voronoi volumes are additive, $\langle \mathcal{W}_n \rangle = \langle \mathcal{W} \rangle = NV_g/\phi$. The fluctuations in Voronoi volume are divided by the number of grains, N, thereby introducing the fluctuation density, shown in Fig. 5.6 into Eq. (5.5). Therefore, the above integration is rewritten as:

$$(X/V_g)^{-1} = \lambda \int_{\phi_{\mathrm{RLP}}}^{\phi(X)} \frac{d\phi}{\phi^2 \langle (\mathcal{W}_n - \langle \mathcal{W}_n \rangle)^2 \rangle_n}., \tag{5.6}$$

and then utilize the fluctuations as a function of ϕ, and integrate along a line of constant $Z(\mu)$. Note that while the fluctuations for all $Z(\mu)$ in this study collapse onto a single curve, as illustrated in Fig 5.6, the limit of integration, ϕ_{RLP} in Eq. (5.6), changes as discussed in the phase diagram of [40], increasing as μ decreases.

Following the method presented above, ϕ_{RLP} is extracted from the phase diagram, and used as a limit of integration in order to calculate $X(\phi)$ from fluctuations in Voronoi volume, in Eq. (5.6). The equation of state, $\phi(X)$, is plotted in Fig. 5.7 for different values of the average coordination number of the packings, $Z(\mu)$, revealing that when approaching $\phi_{\mathrm{RCP}} \approx 0.64$, $X \to 0$, regardless of the value of μ. Further, $X \to \infty$ when approaching ϕ_{RLP}, with the smallest volume fraction of the RLP appearing for $\mu \to \infty$ and $Z \approx 4$ in the high-compactivity limit, $\phi_{\mathrm{RLP}} \approx 0.55$. The compactivity curve plotted in Fig. 5.7 is continuous, even though the volume fluctuation data is the result of a discrete set of simulations. This is due to the approximation of the volume fluctuations as a function of ϕ, resulting in a smooth integration for the compactivity, and subsequently the entropy.

Entropy.— The entropy, S, and its density, $s = S/N$, are obtained by integrating

$$X^{-1} = \frac{\partial S}{\partial V} \tag{5.7}$$

By virtue of having a fixed total volume, V, for any particular system defined by ϕ, substitute $V = NV_g/\phi$ such that:

$$(X/V_g)^{-1} = \frac{-\phi^2 \partial s}{\partial \phi} \tag{5.8}$$

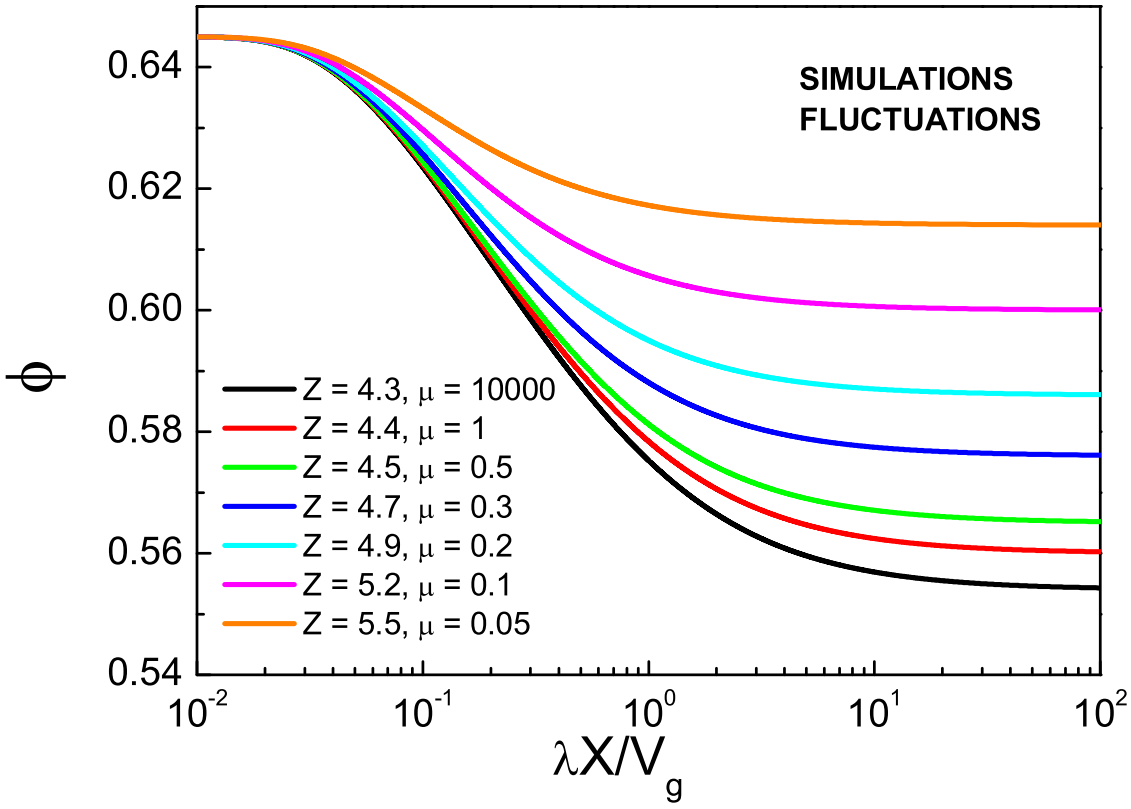

Figure 5.7: ϕ versus X from the integration of Voronoi volume fluctuations.

Using the concept that ϕ_{RCP} is a fixed value in the phase diagram for all values of $Z(\mu)$, integrate between the limits of ϕ_{RCP} and the desired ϕ.

$$s(\phi) - s(\phi_{\mathrm{RCP}}) = \lambda \int_{\phi}^{\phi_{\mathrm{RCP}}} \frac{d\phi}{(\lambda X/V_g)\phi^2}. \tag{5.9}$$

Eq. (5.6) and Eq. (5.9) can be combined to provide an equation for s as a function of the Voronoi volume fluctuations.

$$s(\phi) = \lambda \int_{\phi}^{\phi_{\mathrm{RCP}}} d\phi'/\phi'^2 \int_{\phi_{\mathrm{RLP}}}^{\phi'} d\phi''/(\phi''^2 \langle (\mathcal{W}_n - \langle \mathcal{W}_n \rangle)^2 \rangle)_n + s(\phi_{\mathrm{RCP}}) \tag{5.10}$$

Integration of the compactivity curve achieved via simulation provides the entropy, up to a constant value at ϕ_{RCP}, as defined by Eq. (5.9). The entropy from simulations is plotted in Fig. 5.8 as a function of ϕ for different values of Z.

Therefore, $s(\phi)/\lambda$ is calculated, up to a constant of integration $s(\phi_{\mathrm{RCP}})$, based on the coarse-grained fluctuations of a packing of identical jammed spherical grains. Integration of the compactivity curve achieved via simulation provides the entropy, up to a constant value at ϕ_{RCP}, as defined by Eq. (5.9). The entropy from simulations is plotted in Fig. 5.8 as a function of ϕ for different values of Z.

5.2.4 Entropy from Information Theory

Analysis of the entropy from fluctuations in Voronoi volume clusters provides a value for entropy density up to a constant of integration $s(\phi_{\mathrm{RCP}})$, as shown in Eq. (5.10). To obtain the entropy of RCP an independent method based on information theory [87, 81] is utilized, which does not require a constant of integration.

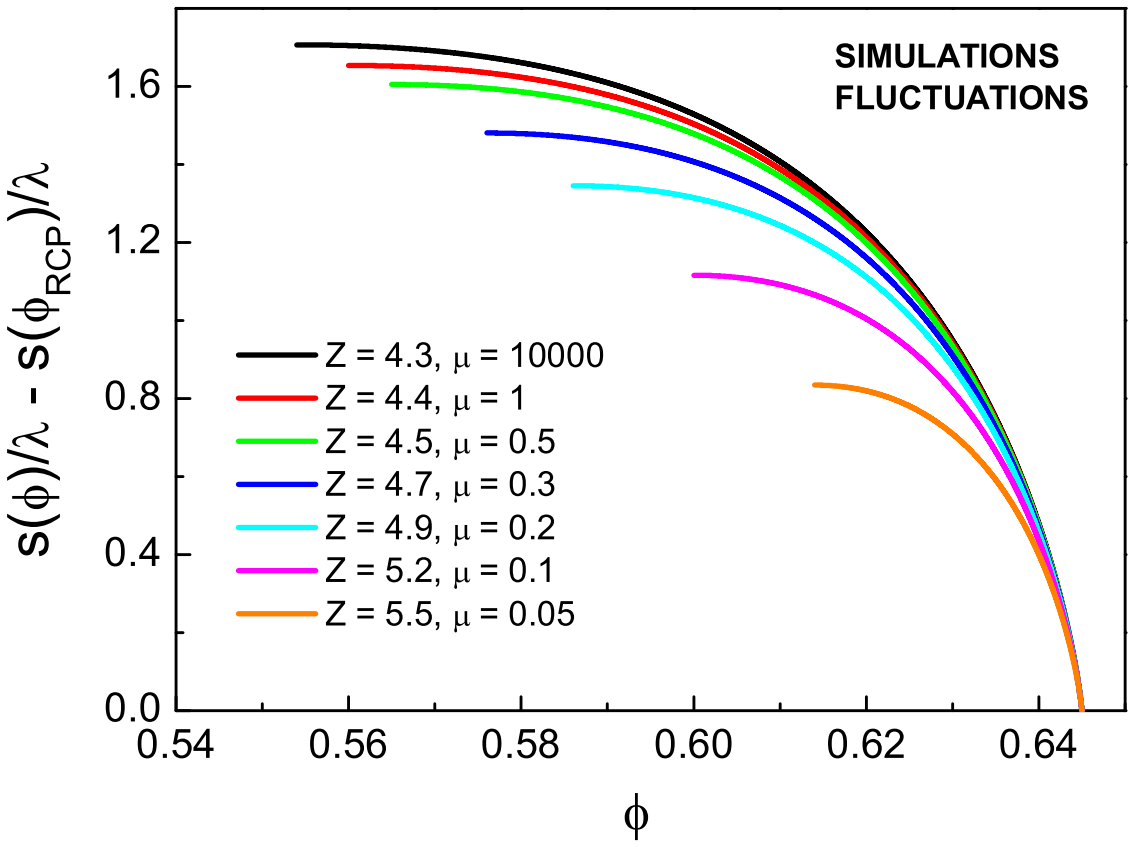

Figure 5.8: Entropy density versus ϕ from the integration of X.

Voronoi cell and Delaunay triangulation is applied to each particle to define a Voronoi network by considering contacts when a Voronoi side is shared between two particles, and hence are Delaunay contacts. In order to facilitate periodic boundary conditions, the finite box enclosing all Voronoi cells is surrounded by 26 virtual boxes. These boxes enclose virtual particles, translated in all possible combinations from the real box. QHull calculates all Delaunay contacts, and only those pairs of contacts which contain at least one real particle are considered, while pairs of virtual contacts are discarded, thus ensuring complete periodic boundary conditions. Further details of the Shannon entropy calculation are described in Chapter 4. Note that in the present study, the crystal correction term is augmented by using the exact values obtained for $g(n)$, and not a fit, as shown in Fig 5.9.

The Shannon entropy is thereby redefined as follows:

$$H'(n) = H(n) - g(n) \tag{5.11}$$

and the entropy density is

$$s = \lim_{n\to\infty} [H'(n+1) - H'(n)] \tag{5.12}$$

which converges so rapidly, as shown in Fig. 5.10 that even moderate values of n are enough to obtain a sufficient approximation of s [81].

When examining values of the Shannon entropy for values of $\phi < \phi_{RCP}$, Fig. 5.11 displays an increase in the entropy as volume fraction decreases, similar to that of the entropy as calculated via Voronoi volume fluctuation density. However, this increase does not appear dependent on the mechanical coordination number of the

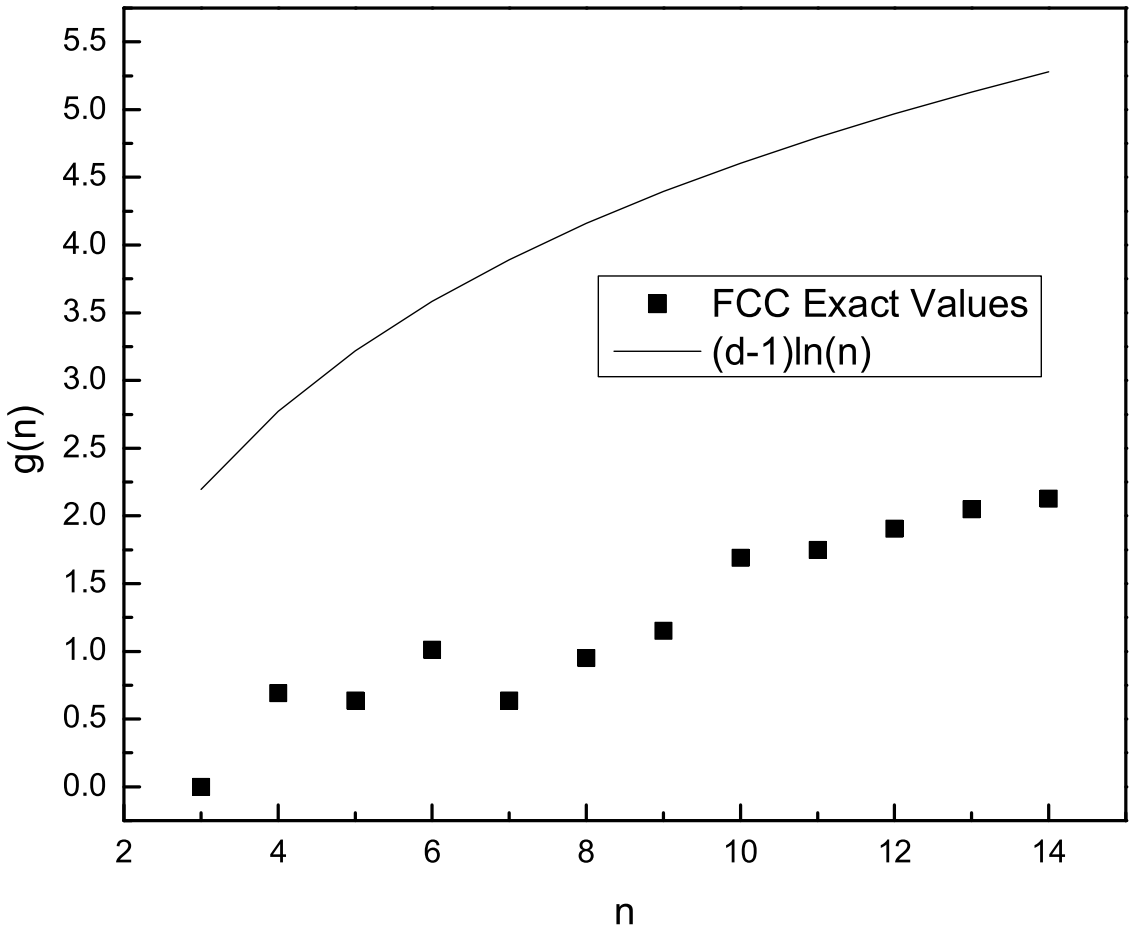

Figure 5.9: Entropy of crystal (FCC) packing as calculated using graph theoretical methods. While the entropy is approximately equal to $(d-1)ln(n)$, minus a meaningless constant, exact values are used herein.

packings. Further, the Shannon entropy does not increase by the same magnitude as observed in the entropy from fluctuations. As suggested in [82], this discrepancy may be due to the freedom to move grains within the packing without disrupting the Delaunay network, and hence not affecting the probabilities of obtaining a particular class of network. Analysis of such calculations requires a Monte Carlo simulation, in which the available phase space volume the packings can explore is probed [82], with the additional constraint that the packing much maintain the jamming condition under all possible rearrangements. This calculation will be the topic of future study.

Fig 5.11 shows that when approaching ϕ_{RCP} for all values of Z using information theory, $H'(n)/\lambda \simeq 1.1$. Therefore $s(\phi_{RCP})/\lambda = 1.1$, the value of the entropy as calculated via graph theoretical methods.

The Shannon entropy density provides an estimation of the entropy for the RCP state, $s(\phi_{\mathrm{RCP}}) \approx 1.1\lambda$, serving as the constant of integration for the entropy density as realized by volume fluctuations. Thus, the mesoscopic entropy of Fig. 5.8 can be shifted vertically by s_{RCP} as calculated via Shannon entropy methods. Figure 5.12 shows the entropy shifted by this constant value, as calculated via simulation.

The Shannon entropy model is considered herein as the microscopic entropy, as it is independent of the fluctuations in clusters of n Voronoi volumes. For a given set of n Delaunay contacts, each class, i, of graphs contains within it a set of isomorphic graphs. By virtue of grouping all such graphs into a single class, the fluctuations in Voronoi volume between the constituent grains does not impact the Shannon entropy calculation.

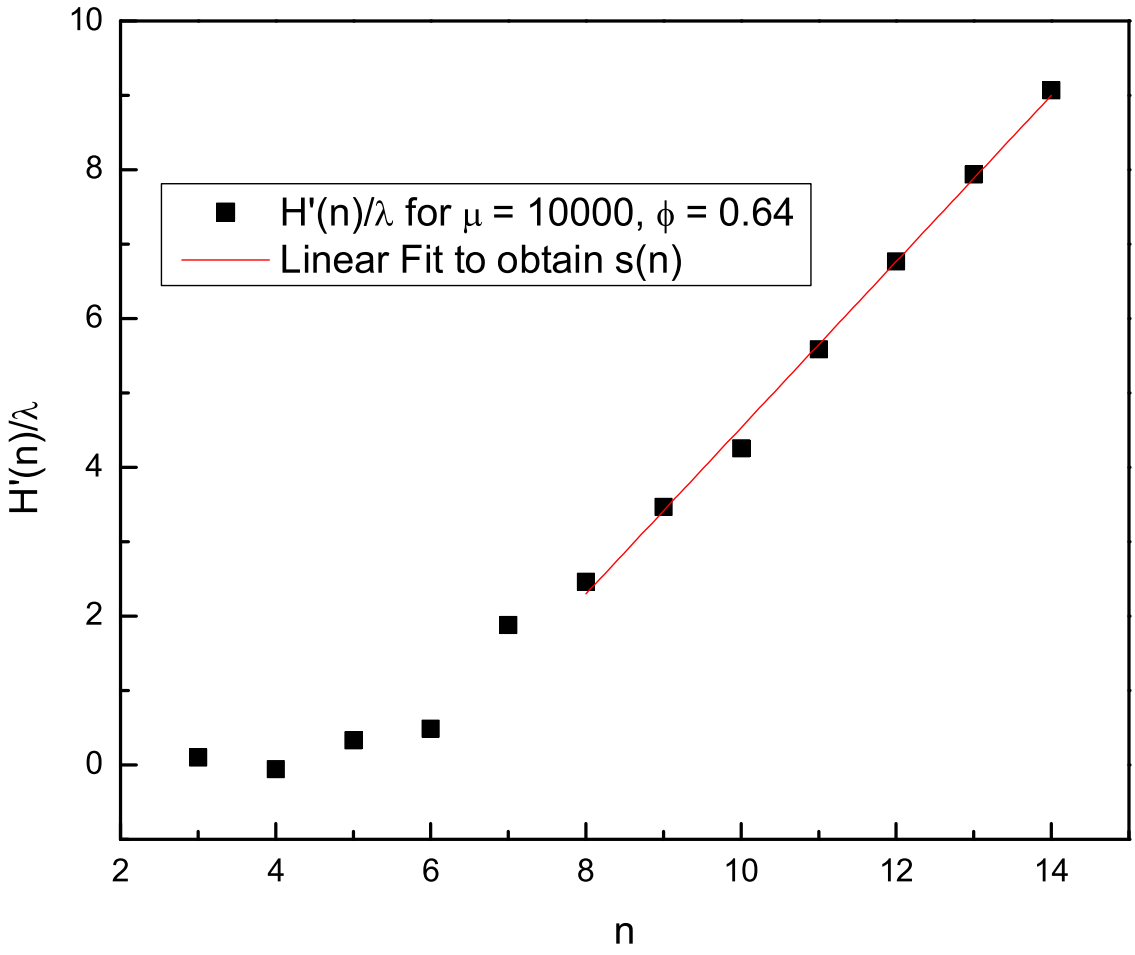

Figure 5.10: Shannon entropy function of n, with $\mu = 10000$ and $\phi = 0.64$. The red line displays a linear fit between $n = 8$ and $n = 14$, from which the entropy density is extracted. This process is repeated for all packings used herein.

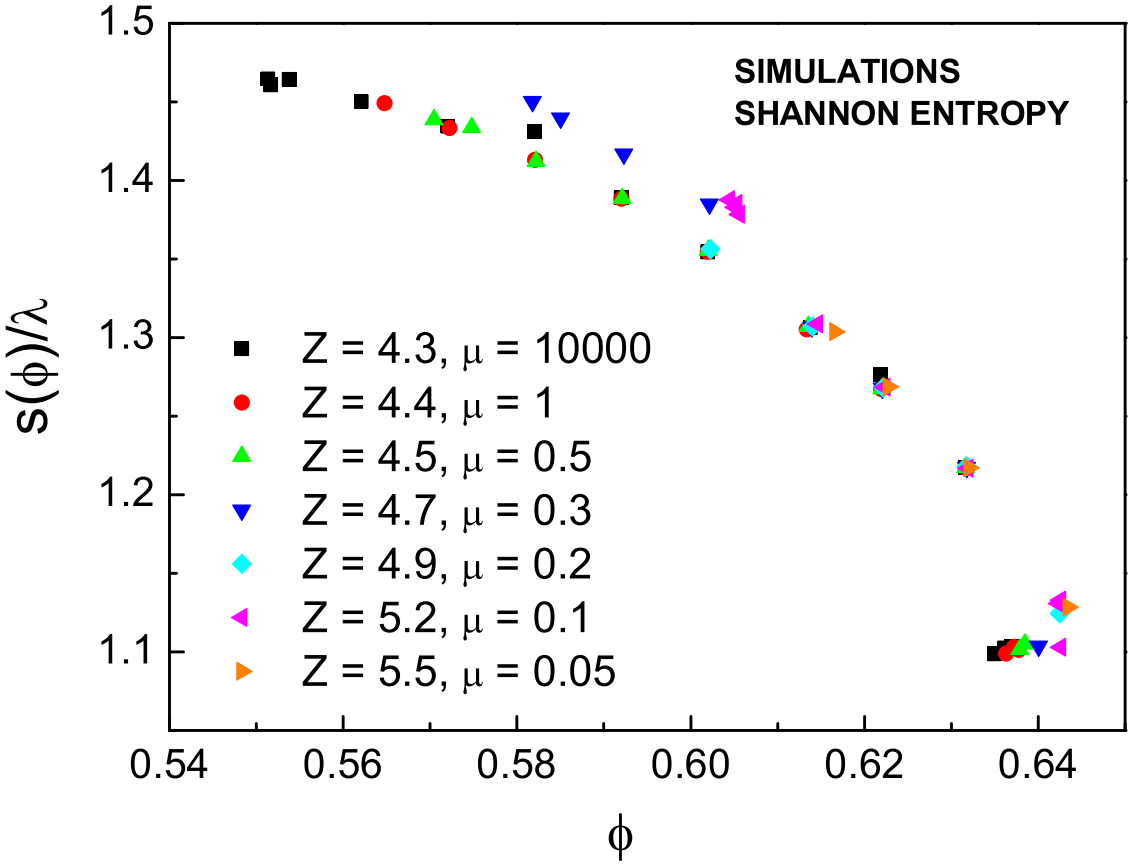

Figure 5.11: Shannon entropy density, $s(\phi)$ for all packings used herein. The minimum value of the entropy density is achieved at RCP, and may be used as a constant of integration. λ is assumed to be unity.

It is asserted that the Shannon entropy, $H'(n)$, evaluated at ϕ_{RCP} is equivalent to the microscopic entropy as defined above. The Shannon entropy density is plotted in Fig. 5.11 versus ϕ for different $Z(\mu)$ Fig 5.11 shows that when approaching ϕ_{RCP} for all values of Z using information theory, $H(n)/\lambda \simeq 1.1$. Therefore, $s_{meso}(\phi_{RCP})/\lambda = 1.1$, the value of the microscopic entropy as calculated via graph theoretical methods.

Thus, the mesoscopic entropy of Fig. 5.8 is shifted vertically by s_{RCP} as cal-

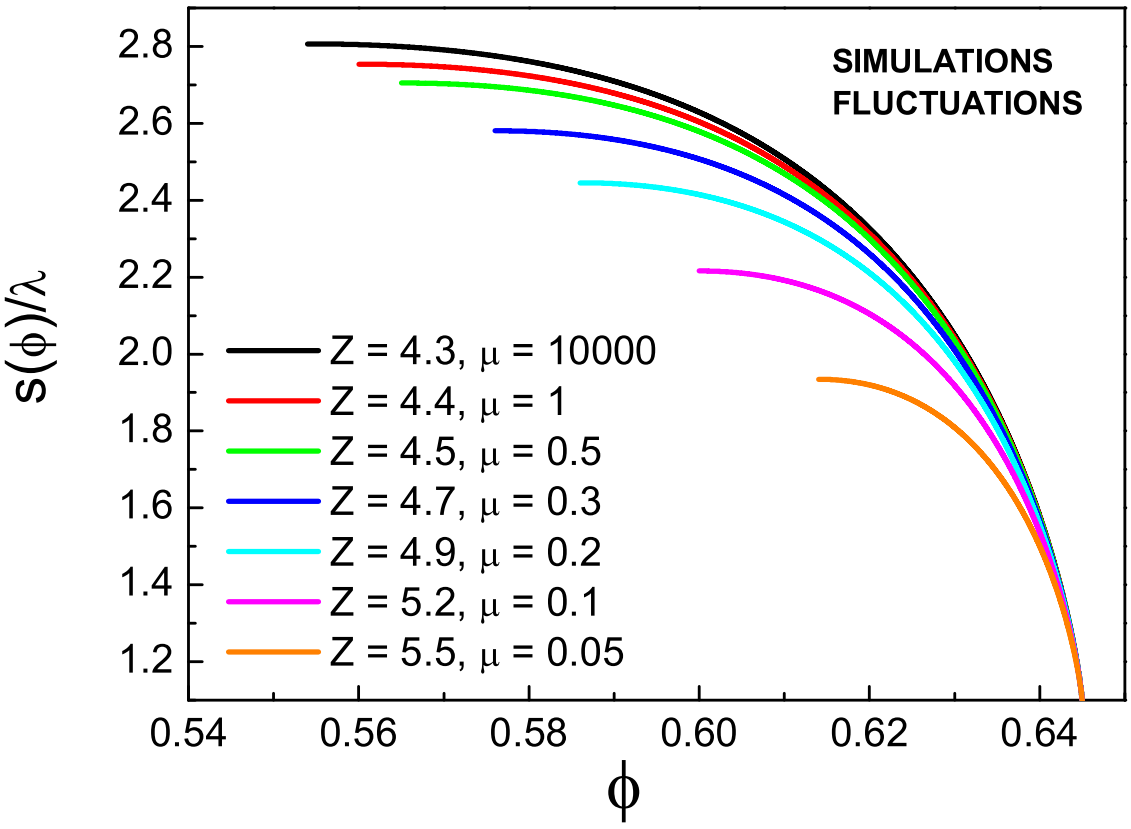

Figure 5.12: Entropy at RCP achieves a value of 1.1 as calculated by the Shannon Entropy at RCP. λ is assumed to be unity.

culated via Shannon entropy methods. Fig. 5.12 shows the mesoscopic entropy shifted by this constant value, as both predicted by theory and calculated via simulation. While the values of both ϕ_{RCP} and $\phi_{\mathrm{RLP}}(Z)$ from the theory are well reproduced by the simulation results, it is clear that the values of s are not. This discrepancy is true for both the magnitude of the entropy and separation between the maximal values of the entropy for different ensembles of constant Z, implying a necessary change to the form of the density of states, $g(Z)$.

5.3 Theoretical Model

5.3.1 Statistical mechanics of frictional hard spheres

Experiments of shaken grains, fluidized beds and oscillatory compression of grains [20] indicate that granular materials show reversible behavior, and the analogue of the conserved energy, E, in thermal systems is the volume $V = NV_g/\phi$, for a system with N grains of volume V_g at position $\vec{r}_i$. Thus, the number of configurations, Ω, and the entropy in the micro-canonical ensemble of jammed hard spheres is defined as [34]:

$$\Omega(V) = e^{S(V)/\lambda} = \int \delta(V - \mathcal{W}(\vec{r}_i)) \;\; \Theta_{\rm jam}(\vec{r}_i) \; \mathcal{D}\vec{r}_i. \tag{5.13}$$

Just as $\partial E/\partial S = T$ is the temperature in equilibrium system, the "temperature" in granular matter is $X = \partial V/\partial S$. Here $\Theta_{\rm jam}(\vec{r}_i)$ is a constraint function restricting the integral to the ensemble of jammed states, $\mathcal{W}(\vec{r}_i)$ is the volume function associated with each particle taking the role of the Hamiltonian in thermal systems. The crux of the matter is then to properly define $\Theta_{\rm jam}$ and $\mathcal{W}$ to calculate the entropy and volume in the ensemble of jammed matter.

Volume and force V-F-ensemble.— A minimum requirement of $\Theta_{\rm jam}(\vec{r}_i)$ is to ensure touching grains, and obedience to Newton's force and torque laws. As in the numerical simulations, the volume function, $\mathcal{W}(\vec{r}_i)$, is taken as the volume of the Voronoi cell associated with each particle at position $\vec{r}_i$, for which an analytical form has been obtained in [40]. The entropy in the V-F-ensemble of frictional hard

spheres is:

$$\Omega_{\rm VF} = e^{S(V)/\lambda} = \int \delta\left(V - \mathcal{W}(\vec{r}_i)\right) \times$$
$$\prod_i \{\delta\left(\sum_{j\neq i} \vec{f}_{ij}\right) \delta\left(\sum_{j\neq i} \vec{f}_{ij} \times \vec{r}_{ij}\right)\ \delta(\vec{f}_{ij} - \vec{f}_{ji}) \times \tag{5.14}$$
$$\prod_{j\neq i} [\Theta(\mu {f_{ij}}^N - {f_{ij}}^T) \delta\left([(\vec{r}_{ij})^2 - 1](\vec{f}_{ij})^2\right) \mathcal{D}f_{ij}] \mathcal{D}r_i\},$$

where $\vec{r}_{ij} \equiv \vec{r}_i - \vec{r}_j$, the normal inter-particle force is ${f_{ij}}^N \equiv |\vec{f}_{ij} \cdot \hat{r}_{ij}|$, the tangential force: ${f_{ij}}^T \equiv |\vec{f}_{ij} - (\vec{f}_{ij} \cdot \hat{r}_{ij})\hat{r}_{ij}|$. All quantities are assumed properly a-dimensional for simplicity of notation. The terms inside the brackets $\{\cdot\}$ correspond to the jamming constraint function $\Theta_{\rm jam}$ in Eq. (5.13), and therefore define the ensemble of jammed states. The first three $\delta-$functions inside the big brackets impose Newton's second and third law. The Heaviside $\Theta-$function imposes the Coulomb condition and the last $\delta-$function the touching grain condition for hard spheres, assuming identical grains of unit radius. Integration is over all forces and positions which are assumed to be equally probable as in the flat average assumption in the micro-canonical ensemble.

The conditions specified in Eq. (5.14) are met in the numerical packings, and the results can be interpreted as the ensemble average Eq. (5.14) under assumption of uniformity of the jammed configurations. However, Eq. (5.14) is difficult to solve. Analytical progress can be done by considering a coarse-graining of the Voronoi volume function and working with quasi-particle theory [40] to obtain a configurational entropy at the mesoscopic level. This analysis requires a corollary of the force-balance ensemble: the isostatic conjecture [67] in addition to a

coarse-grained volume function in terms of the coordination number as shown next, summarizing the details of Chapter 3

5.3.2 Volume Function

The mesoscopic theory presented in [40] coarse grains the Voronoi volumes of a jammed granular packing over a mesoscopic length scale and calculate an average volume function. The coarsening reduces the degrees of freedom to one variable, the geometrical coordination number of each grain, and defines a mesoscopic volume function:

$$w(z) = \frac{2\sqrt{3}}{z}, \tag{5.15}$$

If the system is fully random the assumption of uniformity can be extended from the mesoscopic scale to the macroscopic scale, such an equation of state relating $\phi^{-1} = w + 1$ with z is:

$$\phi = \frac{z}{z + 2\sqrt{3}}. \tag{5.16}$$

5.3.3 Partition Function

In the limit of vanishing boundary stress, the system is described by the volume statistics alone. Since the sum over each quasiparticle with volume $w(z)$ is the total volume [40], the partition function can be written as:

$$\mathcal{Z}_{\text{iso}} = \int g(z) e^{\frac{w(z)}{\lambda X}} dz \tag{5.17}$$

The compactivity, is denoted by X and λ is the analogue of the Boltzmann

constant. Eq. (5.17) is the single particle partition function, such that the full partition function for N particles is $\mathcal{Z}_{\text{iso}}^{N}$. Here, $g(z)$ is the density of states.

The density of states is conjectured to take the form [40]:

$$g(z) = (h_z)^{z-2d}, \tag{5.18}$$

where h_z as the analogue of the Planck constant.

The bounds of the geometrical coordination number as $Z \leq z \leq 6$ induce bounds upon the limits of integration in the partition function, accounting for the jamming restriction, Θ_{jam}.

The isostatic partition function thereby becomes:

$$\mathcal{Z}_{\text{iso}}(X, Z) = \int_{Z}^{6} (h_z)^z \exp\left(-\frac{2\sqrt{3}}{zX}\right) dz. \tag{5.19}$$

Obtaining the phase diagram is then a matter of calculating the average volume fraction, $\phi(X, Z)$ by solving the partition function for different values of X and Z.

$$\phi(X, Z) = \frac{1}{\mathcal{Z}_{\text{iso}}(X, Z)} \int_{Z}^{6} \frac{z}{z + 2\sqrt{3}} \exp\left(-\frac{2\sqrt{3}}{zX} + z \ln h_z\right) dz. \tag{5.20}$$

Note that Z_{RCP} appears slightly higher than $Z = 6$ as predicted by the Alexander conjecture [67], [40], and in Chapter 3, falling closer to $Z_{\text{RCP}} = 6.2$ as shown in Fig. 5.2. When considering the upper bound of the partition function as the integral limit of the jamming condition, $Z_{max} = 6.2$. While states with $Z_{max} > 6$ are though to be partially crystallized as described in Chapter 3, packings existing

within the shaded grey region of Fig. 5.2 to not exhibit any grains having $Z = 12$. These packings are thereby considered disordered, within the confines of this analysis. Further, since the variation in Z is small as when examining lines of constant μ, the average of $Z(\mu)$ can be used as the lower bound of the limit in the partition function.

The dotted line in Fig. 5.2 is a plot of the equation of state presented in Eq. (5.16). It is an important result that the values of $\phi(Z_{\mathrm{RLP}})$ well fit $\phi = \frac{Z}{Z+2\sqrt{3}}$, a fact that becomes even more significant upon careful examination of the volume function, as presented below.

5.3.4 Mesoscopic Compactivity

The results presented in Fig. 5.7 are compared to the theoretical model presented in Chapter 3. The theoretical calculation for $\phi(X)$ is achieved exactly as described for $\phi(Z)$ in Eq. (5.20), and is presented in Fig. 5.13.

Highlighting the details of Chapter 3:

In the limit of vanishing compactivity ($X \to 0$) for the theoretical model, only the minimum volume or ground state at $z = 6$ contributes to the partition function. Then the RCP state is:

$$\phi_{\mathrm{RCP}} = \phi(X = 0, Z) = \frac{6}{6 + 2\sqrt{3}} \approx 0.634, \quad Z(\mu) \in [4, 6]. \tag{5.21}$$

In the limit of infinite compactivity ($X \to \infty$), the Boltzmann factor $e^{-2\sqrt{3}/(zX)} \to 1$, and the average in (5.20) is taken over all the states with equal probability.

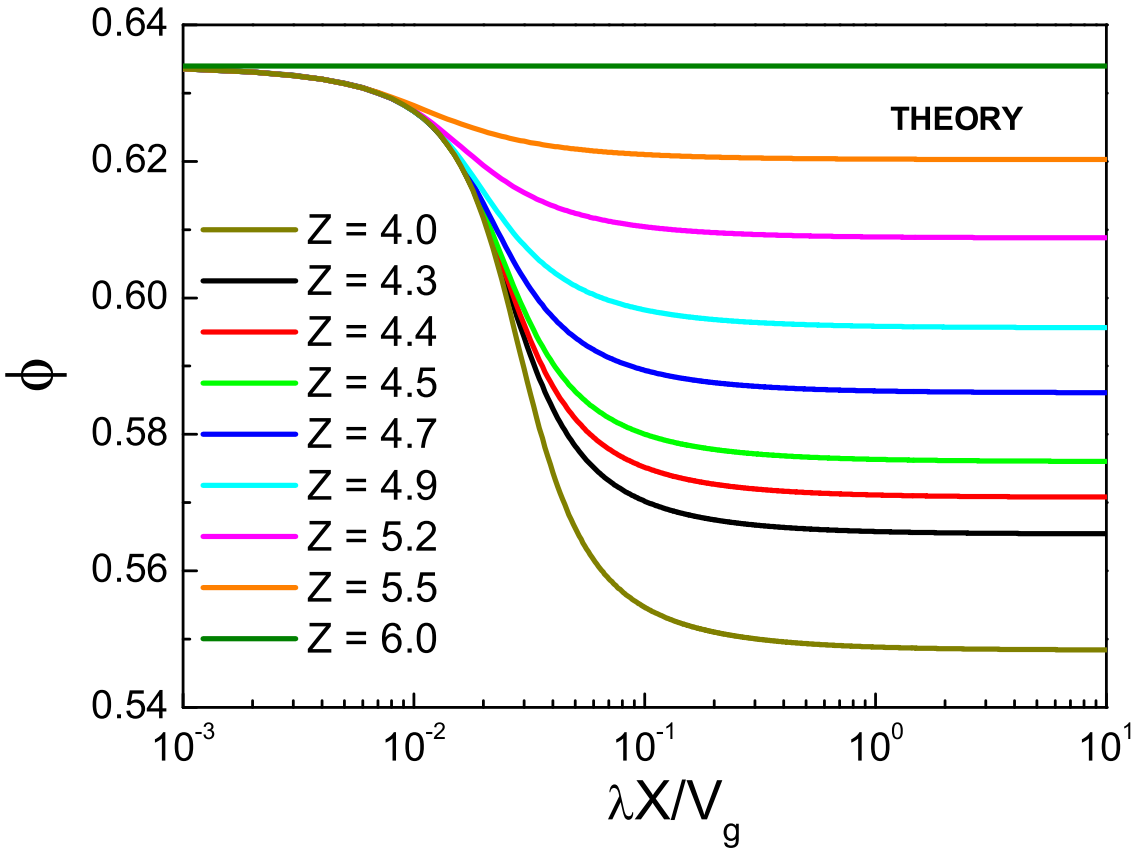

Figure 5.13: Prediction of the mesoscopic theory for $\phi(X)$.

$$\phi_{\mathrm{RLP}}(Z) = \phi(X \to \infty, Z) = \\ \frac{1}{\mathcal{Q}_{\mathrm{iso}}(\infty, Z)} \int_Z^6 \frac{z}{z + 2\sqrt{3}} \exp\left(z \ln h_z\right) dz. \tag{5.22}$$

Assuming $h_z \ll 1$, such that the exponential in Eq. (5.22) decays rapidly, the leading contribution to Eq. (5.22) is from the highest volume at $z = Z$ and therefore:

$$\phi_{\mathrm{RLP}}(Z) \approx \frac{Z}{Z + 2\sqrt{3}}, \quad Z(\mu) \in [4, 6]. \tag{5.23}$$

The general shape of $\phi(X)$, achieved via simulation well matches that as predicted by the mesoscopic theory, if not in magnitude, when using an exponential distribution for $g(Z)$. These results are in agreement with the results of Reference [20]. The compactivity achieves maximal value at the minimal available volume fraction, as observed both when examining the fluctuations in Voronoi volume and within the confines of the mesoscopic theory. Packings near RLP, being the least dense, have the greatest room to be further compacted, or increase density, and therefore approach infinite compactivity. Packings near RCP, being the most dense, have either minimal or zero room for to be further compacted, and therefore cannot increase density and tend towards zero compactivity. This helps to establish the concept of compactivity as a static "effective temperature", acting as a state variable that may link the results of packings preparation and specific packing protocols. The static nature of the compactivity serves to embellish the idea of a zero temperature statistical mechanics framework.

5.3.5 Mesoscopic Entropy

Comparison to the theoretical model begins by defining the equation of state for the entropy density. The entropy of the jammed granular system, can be defined by:

$$S_{meso}(X, Z) = \langle W \rangle / X + \lambda \ln \mathcal{Z}_{\text{sph}}^{\text{hard}}(X, Z) \tag{5.24}$$

where $\mathcal{Z}_{\text{sph}}^{\text{hard}}(X, Z) = \mathcal{Z}_{\text{iso}}(X, Z)^N$ and $\langle W \rangle = N\langle w \rangle$, analogous to the partition function and average energy for a N particle system in equilibrium. The entropy density, $s = \frac{S}{N}$, is obtained as:

$$s_{meso}(X, Z) = \langle w \rangle / X + \ln \mathcal{Z}_{\text{iso}}(X, Z) \tag{5.25}$$

Values of the theoretical entropy density are plotted in Figure 5.14 for several values of Z. Fixing Z equivalently imposes a fixed μ upon the system, as $Z(\mu)$ is determined by μ exclusively within the confines of this model.

The theoretical entropy density captures the general behavior found in the simulations, i.e., it is maximal when approaching RLP for $Z = 4$ and $X \to \infty$ while approaching the minimum entropy at RCP. Furthermore, all the curves for different Z approach $S \sim \ln X$ as $X \to 0$, similar to a thermal ideal gas. Therefore, at the mesoscopic level, the entropy vanishes at RCP. In fact it diverges to $-\infty$ when $\phi \to \phi_{\text{RCP}}$ closer than a constant proportional to h_z (once again assuming an exponential distribution for $g(Z)$ with $h_z = 0.01$), much like the Planck constant imposes a finite size in the phase space of quantum mechanics. Thus, it can be asserted that the value of ϕ at which $\hat{s}(\phi) = 0$ in the theoretical model provides a

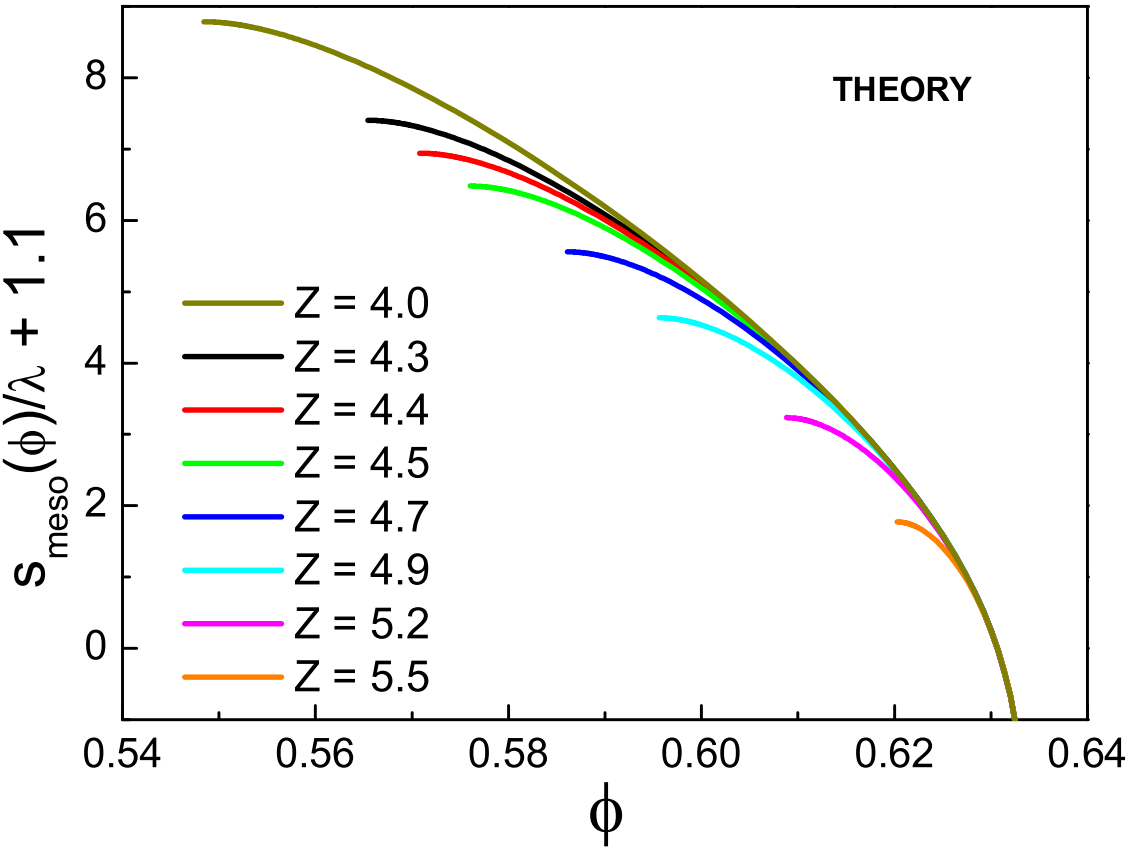

Figure 5.14: Prediction of the mesoscopic theory for $s_{\rm meso}(\phi)$.

definition of RCP at the mesoscopic level.

While $h_z = 0.01$ is used in Fig 5.14 such that the mesoscopic entropy vanishes very close to the predicted value of $\phi_{RCP} \approx 0.634$. However, the maximum value of $\phi_{RCP} \approx 0.642$ from simulation, introduces a discrepancy between the theoretical and simulated models of jammed granular matter. It remains to be determined what the value of $s(\phi_{\mathrm{RCP}})$ is.

While the values of both ϕ_{RCP} and $\phi_{\mathrm{RLP}}(Z)$ from the theory are well reproduced by the simulation results, it is clear that the values of s are not. This is directly due to the magnitude of h_z, and its implications towards the density of states, $g(z)$. We examining $s(X \to \infty, Z)$, the entropy as a function of Z is archived along the RLP line. When $X \to \infty$, the equation of state in Eq. (5.25) is rewritten as

$$s_{meso}(X \to \infty, Z) = \lambda \ln \int_{Z}^{Z_{max}} (h_z)^z dz, \tag{5.26}$$

where $Z = Z_{min}$ and $Z_{max} = 6.2$. This equation is exactly solvable, resulting in the following formula for the mesoscopic entropy along the RLP line.

$$s_{meso}(X \to \infty, Z_{min}) = \lambda \ln\left(\frac{h_z^{Z_{max}} - h_z^{Z_{min}}}{\ln h_z}\right). \tag{5.27}$$

Adjusting the value of h_z directly affects the mesoscopic entropy along the RLP as defined by Eq. (5.27). By a similar analysis, one can obtain a functional form for $\langle \phi(X \to \infty, Z_{min}) \rangle$ along the RLP line.

$$\langle \phi(X \to \infty, Z_{min}) \rangle = \frac{\ln h_z}{h_z^{Z_{max}} - h_z^{Z_{min}}} \int_{Z_{min}}^{Z_{max}} \frac{z}{z + 2\sqrt{3}} (h_z)^z dz. \tag{5.28}$$

While this equation is not exactly solvable, it is easily seen that changing h_z will not only impact the magnitude of the mesoscopic entropy along the RLP line, but also impact the values of $\phi_{\mathrm{RLP}}(Z_{min})$ which define the left most boundary of the phase diagram. Further, the effect on one will be the inverse of the effect on the other. Simply stated, within the present mesoscopic framework, one cannot satisfy fitting both the entropy and phase diagram from simulation to the mesoscopic theory where h_z is the only adjustable parameter.

The full entropy should consider both mesoscopic and microscopic contributions, such that $s = s_{meso} + s_{micro}$. The mesoscopic contribution is obtained via the above described methods, while the microscopic contribution is obtained herein using the Shannon entropy method. When examining the simulations, the full entropy is augmented by its fixed value at RCP, and this value is $s_{RCP} = 1.1\lambda$. In Fig. 5.14, the addition of 1.1 to $s_{meso}(\phi)$ makes two assumptions. First, its assumes that $s_{meso}(RCP) = 0$. Second, it assumes that $s_{micro}(RCP) = s_{micro}(\phi_{\mathrm{RCP}}) = 1.1\lambda$, as determined by the Shannon entropy method, and is not an explicit function of ϕ, similar to the addition of the constant of integration in the full entropy achieved via simulation.

The discrepancy at ϕ_{RCP} reveals the existence of packings above the maximal predicted value using the "split" algorithm packing protocol, indicated by the shaded portion of Fig. 5.2. Packings of identical spherical grains are well known to exist above $\phi = 0.634$, up through the highest achievable packing fraction of $\phi_{\mathrm{FCC}} = 0.74$ in $3d$. This suggests that partial crystallization of the packings may occur as $X \to 0$ within the simulation protocol, shifting the resulting ϕ_c to the right of the theoretically predicted value of ϕ_{RCP}, even though these packings do

not exhibit any grains having $Z = 12$. It will be the topic of future study to analyze the process of partial crystallization, continuing the phase diagram, and equations of state, from RCP to FCC.

5.3.6 Density of States

Assumption of an exponential form for the density of states in the partition function implies the expectation of a single mesoscopic state at RCP, and a dramatic increase in the number of states when approaching RLP. This form can be explicitly corrected by utilizing values for the entropy density as calculated via the Fluctuation dissipation relation.

The formula for the entropy density of jammed matter can be rewritten as a differential equation:

$$\frac{s}{\lambda} = X\frac{\partial ln\mathcal{Q}_{iso}}{\partial X} + ln\mathcal{Q}_{iso} \tag{5.29}$$

This form has an exact solution for $\mathcal{Q}_{iso}$.

$$\mathcal{Q}_{iso} = e^{\frac{1}{\lambda X}\int sdX} \tag{5.30}$$

Examining this solution, a definition for $g(Z)$ is defined:

$$g(Z) = -(\frac{1}{\lambda X}\int \frac{\partial s}{\partial Z}dX)e^{\frac{2\sqrt{3}}{\lambda Z X}+\frac{1}{\lambda X}\int sdX} \tag{5.31}$$

Analysis of this definition, however, requires accurate knowledge of $S(X)$. Furthermore, it necessitates a knowledge of X at its intermediate values, a concept seemingly related to the value of ϕ at which the 'split' algorithm initiates fric-

tional forces, but such an analysis is not well defined. It is here where differences physical data and theoretical data pose an issue. When examining the limit of $\mathcal{Q}_{iso}$, when either $Z \to Z_{max}$ or $X \to 0$, it becomes evident that the value of $\mathcal{Q}_{iso}$ tends towards zero. Combining this with Eq. (5.30), the value of s must tend towards $-\infty$. This is in direct contradiction with physical data for s as measured by volume fluctuations, which has $s \approx 0$, and considers s_{RCP}) to be a microscopic constant experimentally calculated via simulation.

Therefore, analysis of $g(Z)$ using data as $X \to \infty$ is more physically reasonable, and computationally convenient. In this limit, Eq. (5.30) reduces to a more simple form

$$\mathcal{Q}_{iso} = e^{\frac{s}{\lambda}} \tag{5.32}$$

This is easily seen from the definition of the equation of state, as the term $\langle w \rangle / X$ reduces to zero. Further, in this limit, $\mathcal{Q}_{iso}$ considers all states equiprobable, much like in the infinite temperature limit of equilibrium thermodynamics. This results in the following equation for $g(Z)$, in terms of s.

$$g(Z) = -e^{\frac{s_\infty(Z)}{\lambda}} \frac{\partial(\frac{s_\infty(Z)}{\lambda})}{\partial Z} \tag{5.33}$$

where $\frac{s_\infty(Z)}{\lambda}$ is the value of s/λ taken at infinite compactivity, or along the RLP line of the phase diagram. The problem has been thereby reduced to examining s approaching RLP. Fig. 5.15 shows the entropy density as a function of Z at infinite compactivity.

The solid line in Fig. 5.15 is an initial logarithmic fit to the entropy density at

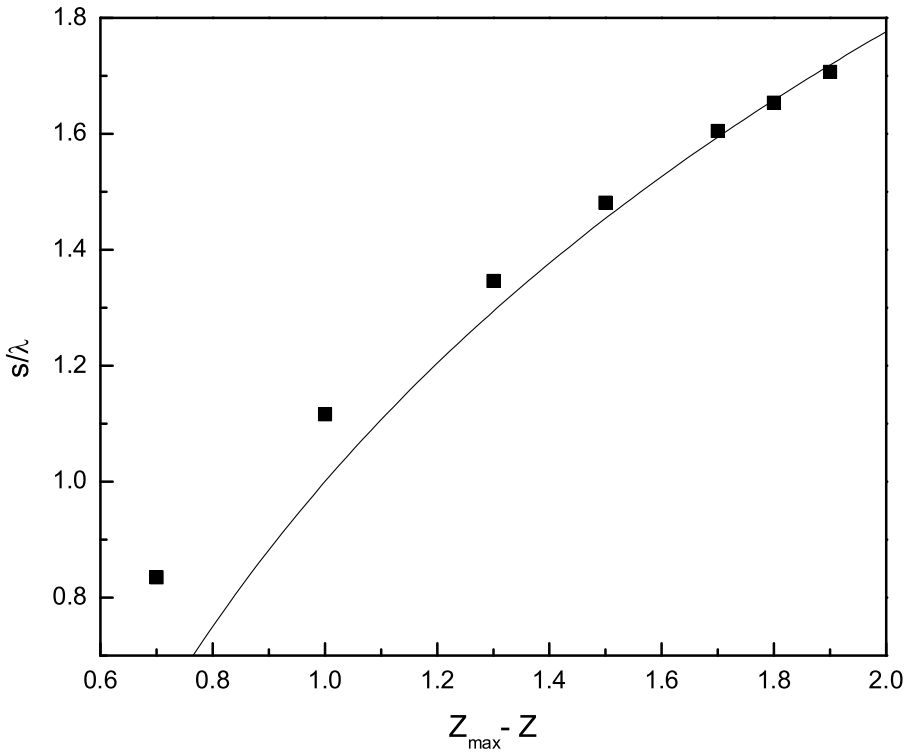

Figure 5.15: Mesoscopic Entropy Density, $s_\infty(\phi)$ at $X \to \infty$. Solid line shows log fitting, $\alpha ln(Z_{max} - Z) + \beta$ with $\alpha = 1.12$ and $\beta = 1.0$. $Z_{max} = 6.2$. The fitting diverges to $-\infty$ when approaching RCP.

infinite compactivity, or along the RLP line. This fit is a rough approximation, as fitting $s_\infty(Z)$ approaching the J-point is difficult. The fit is of the form

$$\frac{s_\infty(Z)}{\lambda} = \alpha ln(Z_{max} - Z) + \beta \tag{5.34}$$

with $\alpha = 1.12$ and $\beta = 1.0$. $Z_{max} = 6.2$, as determined from the phase diagram. Using this form in Eq. (5.33) results in the following power law form for the density of states

$$g(Z) = \alpha e^{\beta}(Z_{max} - Z)^{\alpha - 1} \tag{5.35}$$

The graph of $g(Z)$, shown in Fig 5.16 shows a decreasing number of states when approaching RCP from RLP. However, this fit does not allow for a single mesoscopic state at RCP, as predicted by the theoretical exponential form for $g(Z)$, since $g(Z) \to 0$ at RCP. The small value for α allows for a very sharp increase in the density of states at RCP, such that $g(Z) = 1$ very close to RCP.

Inserting the newly calculated $g(Z)$ into the partition function for jammed granular matter, shown in Fig 5.17, the values of s at RLP are well reproduced, though the accuracy decreases when approaching $Z_{max} = 6.2$, or the J-point. The equation of state, however, fails to accurately predict the values of $\phi_{\mathrm{RLP}}(Z) \approx \frac{Z}{Z+2\sqrt{3}}$, which are well represented in the phase diagram used herein. This implies a need for further correction to the partition function, one possibility of which is presented below.

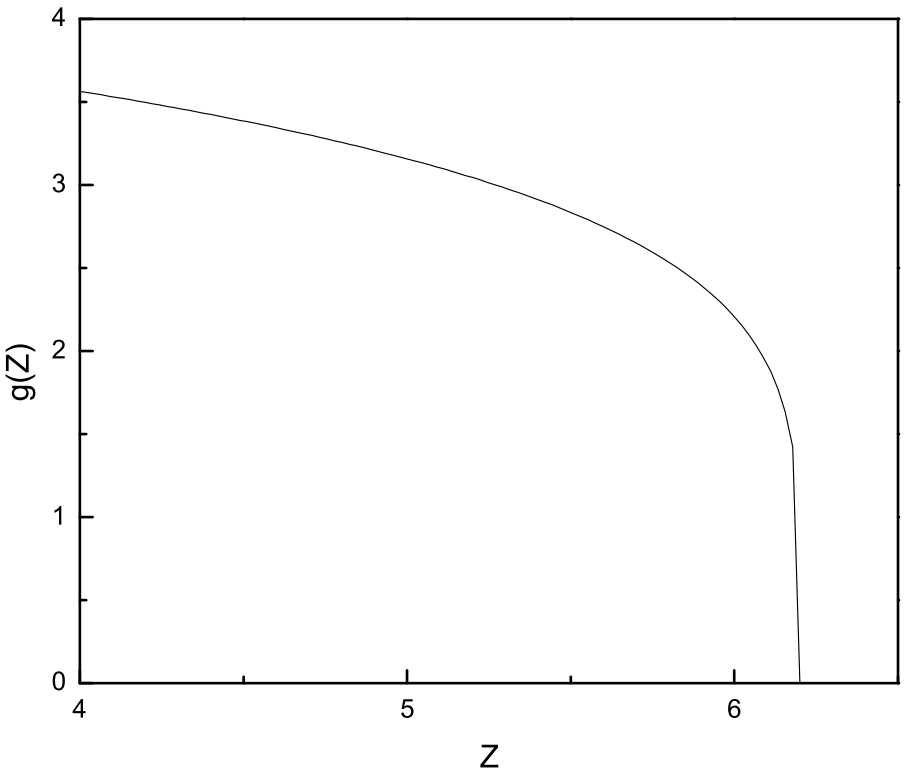

Figure 5.16: Density of States, $g(Z)$, as approximated by numerical methods. $g(Z)$ is maximal at RLP and minimal at RCP, following a power-law relationship, $\alpha e^{\beta}(Z_{max} - Z)^{1-\alpha}$ with $\alpha = 1.12$ and $\beta = 1.0$. $Z_{max} = 6.2$.

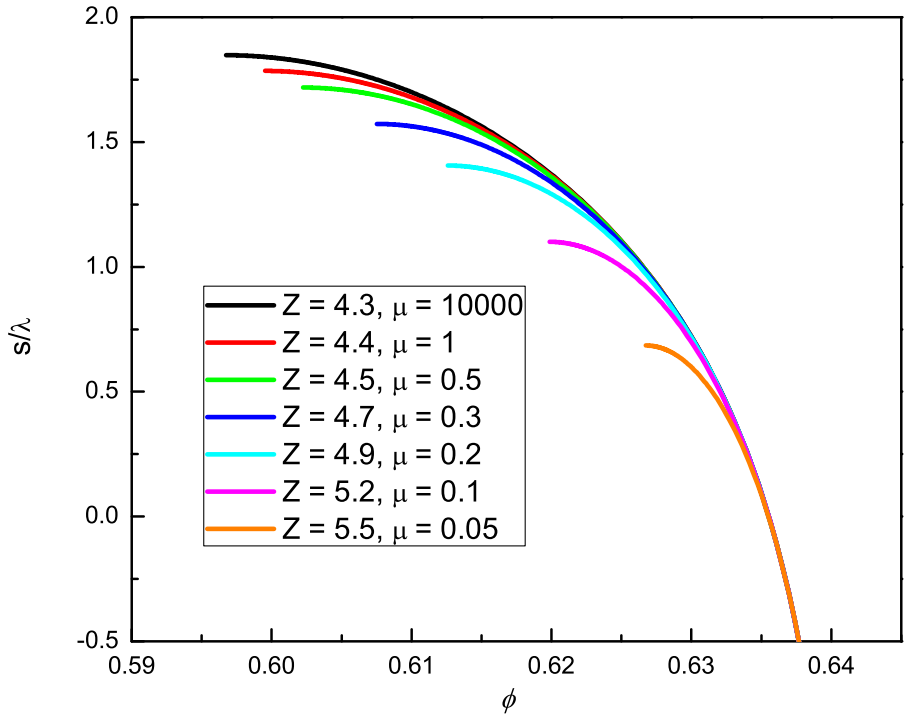

Figure 5.17: Entropy density as calculated using theoretical methods with new $g(Z)$. RCP is well predicted, while the RLP is notably inaccurate, as the curve fails to explore the full phase diagram.

5.3.7 Modified Volume Function

In order to obtain the proper values of s at RLP, the above $g(Z)$, or a close approximation to it, must be used within the scope of the partition function for jammed granular matter. In an effort to simultaneously achieve the correct values for $\phi_{\mathrm{RLP}}(Z)$, a similar method is used to that of calculating $g(Z)$ above.

Within the scope of the partition function, the average free volume per particle is defined as

$$\langle w \rangle = \frac{\int_Z^{6.2} w(z) g(z) e^{\frac{w(z)}{\lambda X}} dz}{\mathcal{Q}_{iso}} \tag{5.36}$$

Simulations well reproduce the approximation of $\langle w(Z) \rangle = 2\sqrt{3}/Z$, but Eq. (5.36), incorporating the modified density of states, $g(Z)$, from above, does not. This is because the magnitude of $g(Z)/g(Z_{max})$ is not large enough, such that values of $w(Z)$ with $Z > Z_{min}$ contribute more to the overall average. It becomes a plausible concept to suggest that $w(Z) \neq \langle w(Z) \rangle$ for all values of Z. Here, a correction to $w(z)$ is calculated such that both $s(\phi_{\mathrm{RLP}})$ and $\phi_{\mathrm{RLP}}(Z)$ as calculated from the theoretical model have approximately consistent values with those obtained via simulation.

Eq. (5.36) can be rewritten as

$$\frac{2\sqrt{3}}{Z} = \frac{\int_Z^{6.2} w(z) g(z) dz}{\mathcal{Q}_{iso}} \tag{5.37}$$

with $X \to \infty$ and $\langle w(Z) \rangle = 2\sqrt{3}/Z$. With a simple differentiation with respect to Z, and the fact that the partition function is easily integrable in the infinite compactivity limit, this equation can be easily solved resulting in a form for $w(Z)$

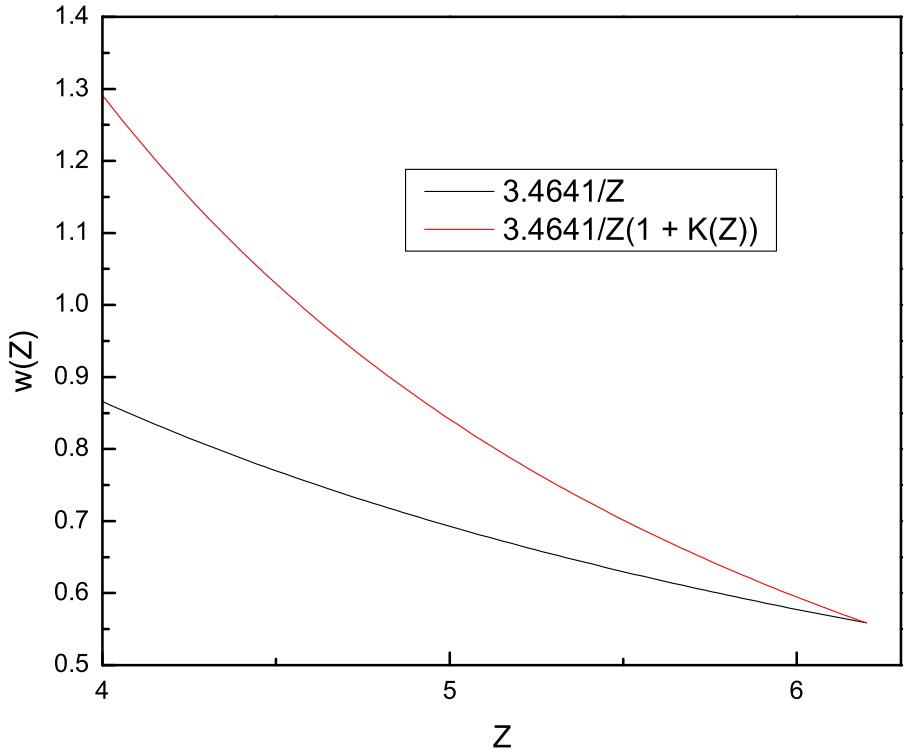

Figure 5.18: The volume function, $w(Z)$. The solid black line shows $w(Z) = \frac{2\sqrt{3}}{Z}$, while the solid red line shows $w(Z) = \frac{2\sqrt{3}}{Z}(1 + K(Z))$, where $K(Z) = \frac{Z_{max}-Z}{\alpha Z}$.

$$w(Z) = \frac{2\sqrt{3}}{Z}(1 + K(Z)) \tag{5.38}$$

where $K(z) = \frac{Z_{max}-Z}{\alpha Z}$. When $Z = Z_{max}$, $w(Z) = \langle w(Z) \rangle$, but, for all other values of Z, $w(Z) > \langle w(Z) \rangle$, as shown in Fig 5.18, thereby weighing more heavily those values of the volume function for lower Z, reproducing the correct average value.

When this modified volume function is used in conjunction with $g(Z)$ as calculated above, the equations of state well reproduce those obtained via simulation, as shown in Fig. 5.19 and Fig. 5.20.

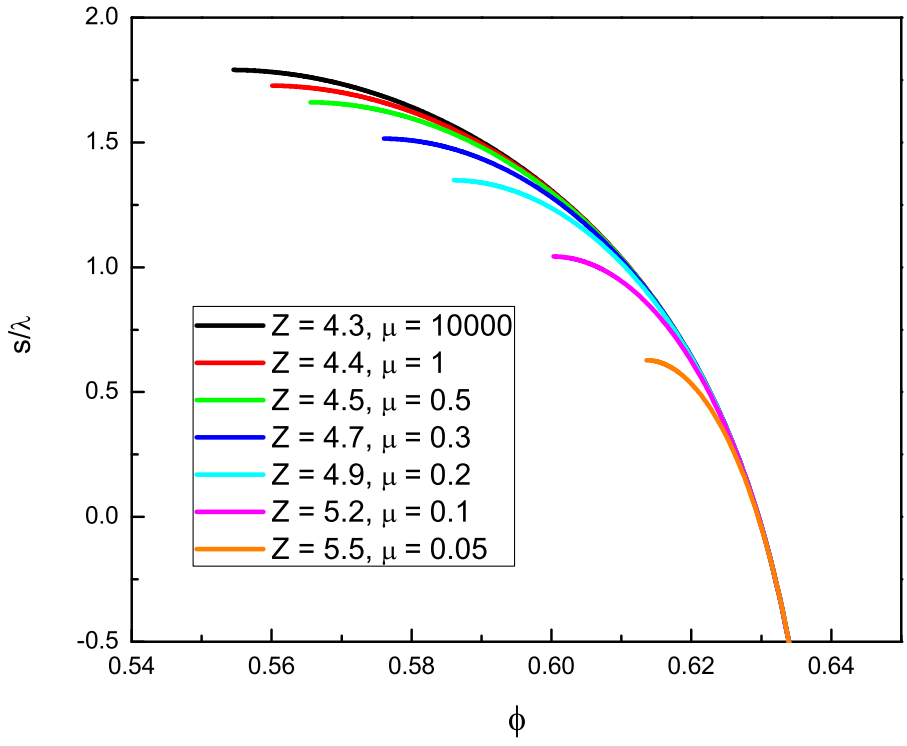

Figure 5.19: Entropy density, $s(\phi)$, calculated using theoretical methods with new $g(Z)$ and modified $w(Z)$. RCP and RLP are well matched by simulation results.

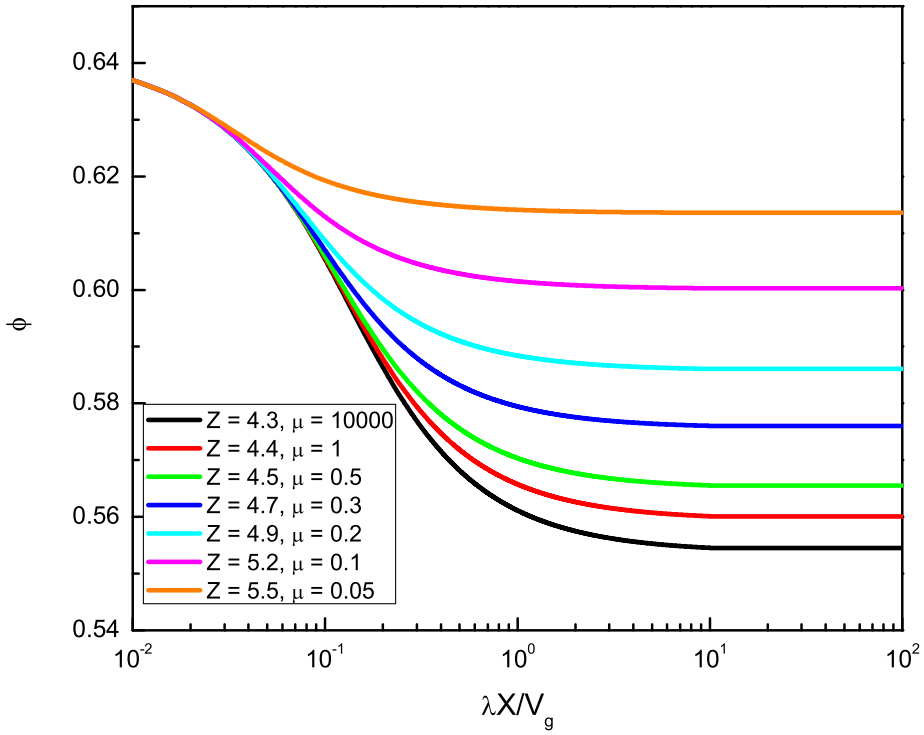

Figure 5.20: Compactivity, $\phi(X)$ as calculated using theoretical methods with new g(Z) and w(Z). The curves well match simulation results, with a significant improvement when comparing lines of isocompactivity.

Upon shifting the mesoscopic entropy density by 1.1, as determined via microscopic calculations, the entropy vanishes in the modified theoretical model at a volume fraction observed to be significantly closer to the J point of simulations. Fig. 5.21 shows this comparison for $Z = 4.3$, the lowest mechanical coordination number achieved for the simulations used herein.

5.3.8 Negative Compactivity

Analyzing the partition function from a mathematical approach, the concept of negative compactivity and its effect on the equation of state are a topic of interest.

When $X \to 0^+$, $\phi(X \to 0^+) \to \phi_{\text{RCP}} = \frac{1}{\langle w(Z_{max})\rangle+1}$, where Z_{max} is the upper limit of integration in Eq. (3.19). Under the assumption of a very large $g(Z)$ at Z_{min}, with respect to any higher Z, $X \to \infty$, $\phi(X \to \infty) \to \phi_{\text{RLP}} = \frac{1}{\langle w(Z_{min})\rangle+1}$, where Z_{min} is the lower limit of integration in Eq. (3.19). This occurs because when using the partition function of [40], with $h_z \ll 1$, $g(z) \sim \delta(z - z_{min})$. However, as evidenced above, an exponential form for $g(z)$ may not well reproduce simulation results for the entropy. Altering $g(z)$ is shown to better reproduce the entropy equation of state, but shifts the predicted value of ϕ_{RLP} higher. Examination of a negative compactivity within the above presented statistical mechanics framework should allow us to achieve the minimum value of RLP in the limit $X \to 0^-$.

When $X \to 0^+$, the Boltzmann factor in the partition function of Eq. (3.19) tends towards zero. As such, the largest value of z, or the smallest value of $1/z$ will give the largest value of the Boltzmann factor when using the partition function to calculate observable averages. This results in the calculation of the RCP state. However, when $X \to 0^-$, the Boltzmann factor in the partition function tends

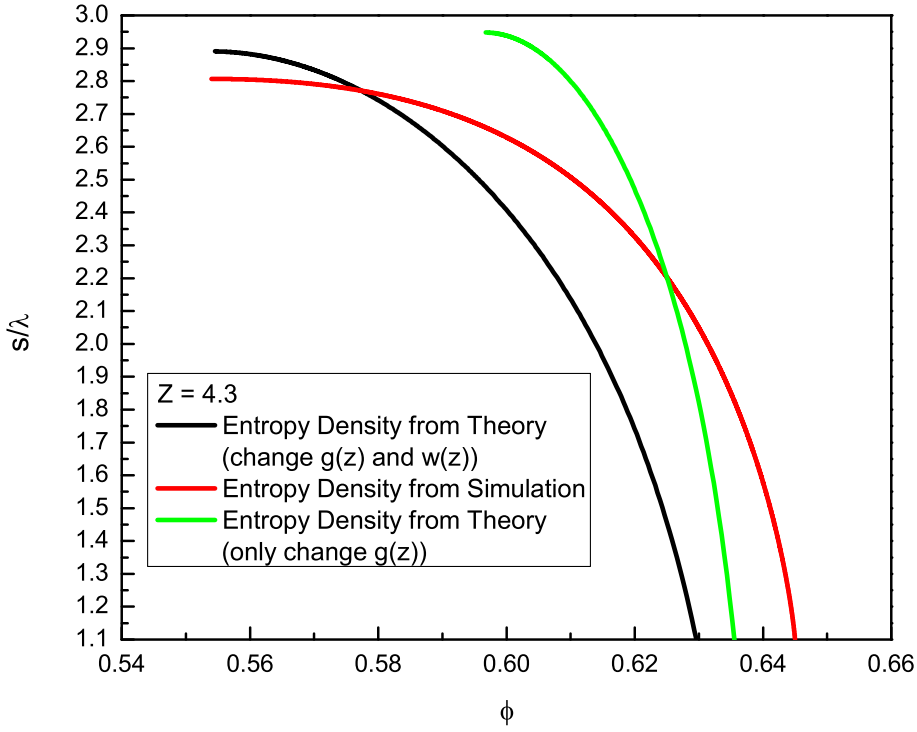

Figure 5.21: Entropy density from theory and simulation, compared for Z = 4.3. The red line indicates results from simulation. The green line indicates the theoretical model, with only g(Z) modified, clearly not exploring the entire phase diagram. The black line indicates the theoretical model, with both g(Z) and w(Z) modified, exploring a much larger part of the phase diagram. Note that all curves assume $s_{\mathrm{RCP}} = 1.1\lambda$, as predicted by the Shannon entropy.

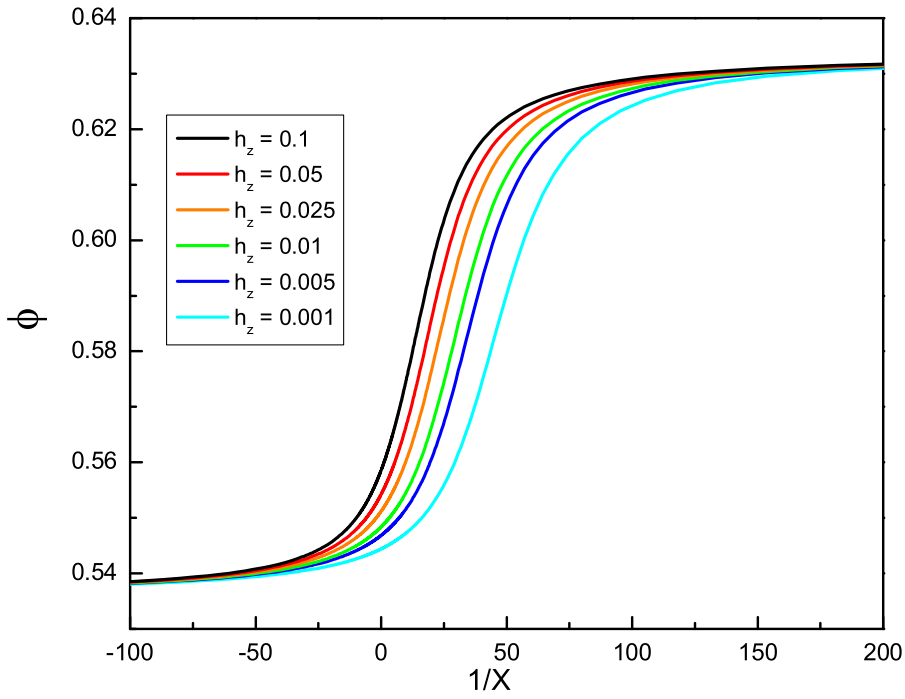

Figure 5.22: Volume fraction as a function of the inverse of compactivity, for Z = 4, as calculated using theoretical methods, including negative compactivity values, for h_z ranging from 0.001 to 0.1. When X discontinuously jumps from ∞ to $-\infty$, $\phi(X)$ exhibits continuous behavior. However, when X continuously goes from 0^- to 0^+, $\phi(X)$ exhibits a discontinuous jump from ≈ 0.536 to ≈ 0.634.

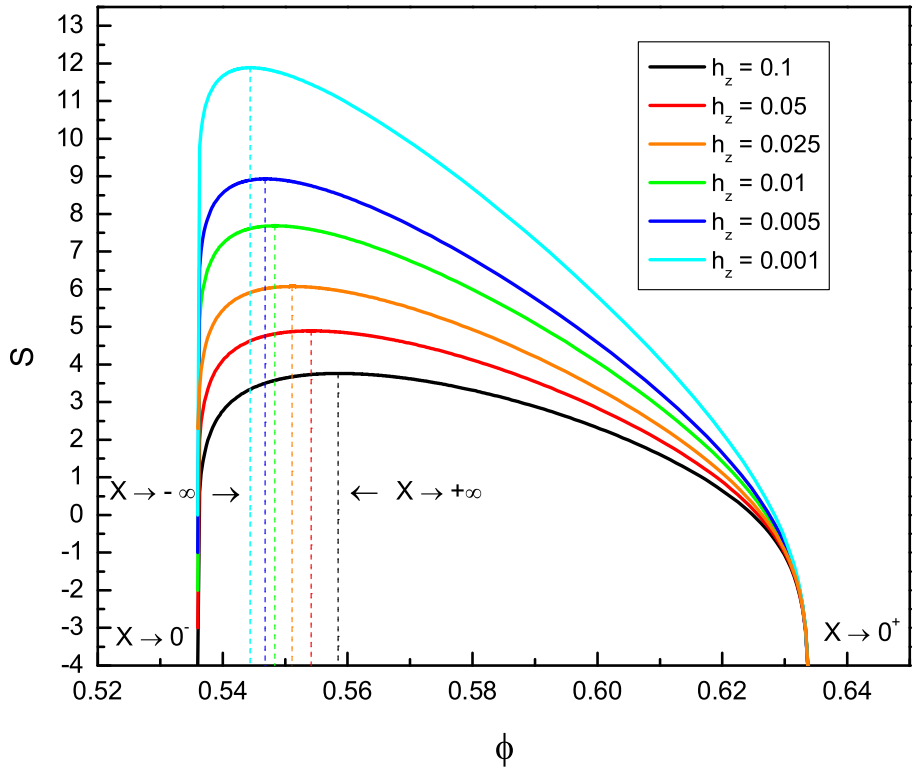

Figure 5.23: Entropy plotted for Z = 4, as calculated using theoretical methods, including negative compactivity values. $S(\phi)$ tends towards $-\infty$ at $\phi = 0.536$ ($X \to 0^-$ and $\phi = 0.634$ ($X \to 0^+$), the minimal value of RLP and RCP, respectively, for any value of h_z. Dashed vertical lines show $\phi(X)$ for $X \to \pm\infty$, acknowledging the lowest physically achievable volume fraction at $Z = 4$ for a particular value of h_z. Larger values of h_z result in larger values of $\phi(X \to \pm\infty)$.

towards infinity, not zero, and the largest value of Z, or the smallest value of $1/z$ will give the largest value of the Boltzmann factor. When calculating the average volume function in either case, the density of states will not greatly impact the results with respect to the contribution from the Boltzmann factor. Therefore, when $X \to 0^-$, the average volume fraction will reduce to the predicted value of the RLP line, $\phi_{\text{RLP}} = \frac{1}{\langle w(Z_{min})\rangle+1}$, with $\langle w(Z)\rangle = \frac{2\sqrt{3}}{Z}$. Fig. 5.22 exemplifies this phenomena.

The entropy equation of state should achieve the same values as $X \to +\infty$ and $X \to -\infty$, since $g(z)$ is independent of compactivity, as presented herein, and the Boltzmann factor approaches unity in either case. Although not as obvious, the same can be said for $X \to 0^+$ and $X \to 0^-$. The equation of state (5.25) can be rewritten as:

$$s_{meso}(X, Z) = \ln \int_Z^6 (h_z)^z e^{-\frac{1}{X}(w(z)-\langle w(z)\rangle)} dz. \tag{5.39}$$

In the case of $X \to 0^+$, X is positive, and $w(z) \geq \langle w(z)\rangle$, as RCP represents the lowest attainable value of $\langle w(z)\rangle$. The exponentiated term in the partition function is always negative, such that the entropy approaches $-\infty$. Conversely, when $X \to 0^-$, X is negative, and $w(z) \leq \langle w(z)\rangle$, as RLP represents the highest attainable value of $\langle w(z)\rangle$. Again, the exponentiated term in the partition function is always negative, such that the entropy approaches $-\infty$.

Fig. 5.23 displays the equation of state along the G-line as calculated by the theoretical model of [40]. $Z_{min} = 4$ and $Z_{max} = 6$ are used as the limits of integration for the partition function of Eq. (3.19), the exact values predicted by the Alexander conjecture for packings with $\mu \to \infty$ in $3d$. The value of h_z

is increased to show that larger values of $g(z)$ at RLP result in a more precise agreement between $\phi(X \to \pm\infty)$ and $\phi(X \to 0^-)$. The dashed vertical lines of Fig. 5.23 show $\phi(X)$ for $X \to \pm\infty$, acknowledging the lowest physically achievable volume fraction at $Z = 4$ for a particular value of h_z. Larger values of h_z result in larger values of $\phi(X \to \pm\infty)$, allowing for the existence of a greater range of packings with a negative compactivity, having $\phi(X \to 0^-) < \phi < \phi(X \to -\infty)$.

Some models exist where the concept of a negative temperature finds physical meaning, including nuclear spins and semiconducting lasers. In Reference [95] an attempt is made to include the concept of a negative temperature within a statistical mechanics framework. By means of a lattice model in $2d$, utilizing a discrete phase space, mechanically stable packings, or microstates, are shown to exist beneath the volume fraction with the largest number of microstates, at a particular μ. The highest entropy occurs when the largest number of microstates are available, and is the equivalent of ϕ_{RLP} in the above presented mesoscopic theory. Under the assumption of an ergodic exploration of the volume fractions available to the lattice model, this implies that packings with $\phi < \phi_{\mathrm{RLP}}$ exist, with entropy below the maximal value, and that these packings can be explained via the concept of a negative temperature. Reference [95] thereby considers ϕ_{RLP} to be the "loosest possible random packing that is mechanically stable that one can achieve by pouring grains".

Although the present work analyzes packings in $3d$, the results of mesoscopic theory find agreement with the simulations of [95]. Fig. 5.23 shows a maximal entropy at ϕ_{RLP}, indicating the largest number of available microstates to the system. The introduction of a negative compactivity, as described above, allows the theory

to probe states such that $\phi < \phi_{\mathrm{RLP}}$, while $s_{meso}(\phi) < s_{meso}(\phi_{\mathrm{RLP}})$. It becomes apparent that the range of ϕ in which these states may exist is directly related to the magnitude of h_z, decreasing as the discretization of phase space within the confines of the mesoscopic theory such that in the limit of a continuous phase space none of these packings are mechanically stable. The theoretical model includes the concept of a discrete phase space for jammed grains, and simulations show that $h_z < 1$, but not necessarily $h_z \ll 1$. Further, the "split" algorithm utilized simulates a pouring of grains with respect to the method of packing creation. It is possible the concept of a negative compactivity could help to explain areas in the phase diagram of Fig. 5.2 unavailable within the scope of the present study, along with the notion of a first order phase transition. It remains a topic of future study to consider if the packings explored in the present study of a negative compactivity, and those in [95], exceed merely the condition of mechanical stability and further satisfy the jamming condition.

5.4 Outlook

Although extensive detail is presented in this study regarding the various steps necessary to analyze the equations of state, several questions remain unclear.

The derivation of the entropy for jammed granular matter is explicitly calculated via fluctuations in Voronoi cell volume for each packing presented herein. As this study focuses on random packings, crystal states are not achieved with anything other than measure zero probability. Thus, the highest available volume fraction for any given packing is RCP, $\phi \simeq 0.64$, not FCC, $\phi \simeq 0.74$, as corrob-

orated by simulation results. This result is the apparent limit of the preparation protocols used herein. It can be said with certainty that FCC packings have zero fluctuation with respect to their constituent Voronoi cells. At RCP, however, simulations reveal a non-zero fluctuation, as discussed above. This value, while small, is subtracted from the fluctuations calculated in all packings as a microscopic fluctuation to be removed from a mesoscopic theory. This approach, however, does not account for the possibility that for packings above RCP, but below FCC, achieve a continuous, monotonic, degree of crystallization. Such a condition would permit a continuous decrease in fluctuation to exactly zero, from RCP to FCC, thereby rendering the removal of microscopic fluctuations questionable within the scope of a more complete theory that includes random and partially crystallized packings. The compactivity curves presented in Fig. 5.7 no longer reach a plateau when approaching RCP if the microscopic fluctuations are not subtracted, but reach a finite, non-zero, value. It remains possible that a phase transition occurs at RCP, and packings of higher volume fraction need not preserve the properties of a fully random system. It is also a possibility that the packings studied herein at RCP do not necessarily have $X = 0$. It is also a possibility that the packings studied herein at RCP do not necessarily have $X = 0$, but a small finite value leading towards zero compactivity at FCC. It remains an open topic how one would define compactivity between RCP and FCC, as compactivity as been herein attributed to packing protocols resulting in random packings. It should be noted that such a study will not greatly affect the equation of state for the entropy of jammed matter.

The mesoscopic theory of [40] utilized herein considers a vanishing entropy at,

or near, RCP. Taking into consideration the FCC state, a more complete theory including packings between RCP and FCC should be characterized, such that the entropy of jammed matter approaches zero when approaching FCC, not RCP. Figure 5.24 displays a possible interpretation for an extension of the entropic equation of state. The entropy attains a maximal value at ϕ_{RLP}, as predicted by the existing mesoscopic theory. When $\phi_{\mathrm{RLP}} < \phi < \phi_{\mathrm{RCP}}$, the packing consists of purely random microstates, and the entropy decreases when approaching RCP from lower volume fractions, also as predicted. At some point close to ϕ_{RCP}, the entropy deviates from its predicted decrease to zero at ϕ_{RLP}, and follows one of two possible paths. One path exhibits a discontinuity in the first derivative of the entropy, following a straight line to exactly zero entropy at ϕ_{FCC}. The other path exhibits a discontinuity in the second derivative of the entropy, following a smooth, first derivative continuous path, to exactly zero entropy at ϕ_{FCC}. When $\phi_{\mathrm{RCP}} < \phi < \phi_{\mathrm{FCC}}$ a coexistence between random and crystalized microstates may exist, ultimately leading to a purely crystalized packing at FCC. The exact nature of the transition from purely random states to a coexistence of states remains an open topic. The incorporation of microscopic fluctuations and microscopic crystalized states into the existing mesoscopic theory may result in a more complete characterization of the entropy of jammed granular matter.

An additional assumption made in calculating the compactivity of jammed granular matter is that those packings along the RLP line have $X = \infty$. This assumption directly allows for the $\phi(X)$ equation of state without any constants due to integration techniques. It appears to be reasonable to presume that X is large along the simulated RLP line, with respect to X of all other packings used

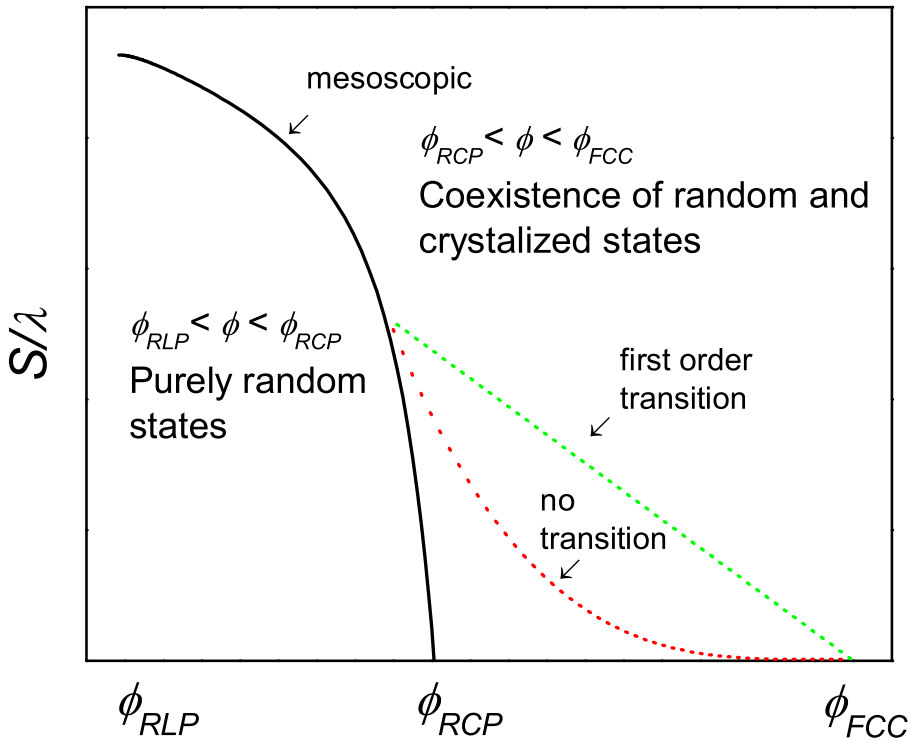

Figure 5.24: A possible extension of the entropy equation of state to include packings between RCP and FCC. For $\phi_{\mathrm{RLP}} < \phi < \phi_{\mathrm{RCP}}$, the packing consists of only random states, and the entropy decreases when approaching RCP from lower volume fractions, as predicted by the mesoscopic curve. At ϕ_{RCP}, the entropy does not decrease to zero, as predicted by the mesoscopic curve, and follows one of two possible paths. The green dashed line exhibits discontinuity in the first derivative of the entropy, while the red dashed line exhibits a discontinuity in the second derivative of the entropy. Both paths achieve exactly zero entropy at ϕ_{FCC}. When $\phi_{\mathrm{RCP}} < \phi < \phi_{\mathrm{FCC}}$ a coexistence between random and crystalized microstates may exist.

herein, and that the constant term $\frac{1}{X(\phi_{\mathrm{RLP}})}$ is very small.

While the concept of negative compactivity works well as a mathematical tool for achieved the RLP state of jammed granular matter, it remains difficult to attribute a physical meaning to such a condition. Recent studies in [95] suggest that negative compactivity probes mechanically stable states that exist beneath RLP, but are not accessible by means of grain pouring. This concept may elucidate the reason why packings near the predicted RLP line exhibit a small discontinuous jump in observables, such as Z and σ. While these jumps indicate the possibility of a first order phase transition, they may also be the product of a physical change in structure from a positive to a negative compactivity. Such ideas are in their infancy, and will remain the topic of future studies.

As mentioned above, there exists a small fluctuation density in Voronoi volume at RCP. The fluctuation density increases as n increases, and comes to a maximal value at a particular range of n, where n is larger when approaching lower values of ϕ as shown in Fig. 5.5. This increase in value is due to selecting of clusters of n Voronoi volumes, as opposed to n randomly chosen grains. In the case of randomly chosen grains, the fluctuation density remains constant, equal to the fluctuation at $n = 1$. Such a change implies a correlation between the Voronoi volumes in clusters of grains, exemplified by Eq. (5.4). This correlation may create a scale separation, such that microscopic correlations dominate the fluctuations at lower n and mesoscopic correlations dominate at higher n. This scale separation would result in a difference between local and global compactivities, suggested in [93], and is a topic of continuing study. It also remains possible that fluctuation densities calculated using larger n sized clusters overuse the data set by largely repeating

constituent Voronoi cells in cluster volumes, thereby rendering the fluctuation densities questionable for packings approaching RLP. Again, it should be noted that simply using the microscopic fluctuations does not greatly effect the entropy calculations. In the event the data is found not to be overused, the correlations may imply a physical reason to include a term of "interaction" within the Hamiltonian for jammed granular matter.

The mesoscopic theory predicts $S \rightarrow -\infty$ when approaching RCP for any μ. This concept does not adhere to physical measurements, where the minimal entropy should be zero. Taking this into consideration, another method must be used to calculate the entropy of packings at RCP, independent of the distribution of Voronoi volumes used to facilitate the mesoscopic theory. The Shannon entropy calculation applies graph theoretical methods, resulting in a non-zero value for the entropy of RCP, well suited for a more complete equation of state. While it can be said with some degree of certainty that the Shannon entropy calculation contributes to the entropy at RCP, it is unclear whether it does so completely. Other methods may be available that provide all of the entropy at RCP, or give additional terms to the Shannon entropy, another topic of continuing study. Further, as discussed above with respect to fluctuation density, packings between RCP and FCC have partial degrees of crystallization, such that the entropy of an FCC packing is exactly zero, or $-\infty$ as described in the theory. Recent work [94] suggests that the entropy experiences an increase immediately following RCP, due to mixing between random and crystal states. Incorporation of these ideas into the present work remains a topic of ongoing study.

The mesoscopic theory presented in Chapter 3 alludes to a single mesoscopic

state available at RCP for all of the packings in the jamming phase diagram. The new density of states, presented herein as a power law and not an exponential distribution, tends to zero when approaching RCP, not unity. This is due to the constants α and β not retaining any dependence on z. Careful examination of Eq. (5.33) shows that an were the entropy at infinite compactivity to tend towards $ln(z_{max} - z)$ at RCP, then $g(z)$ would approach unity at RCP, exactly. Such a function for the entropy is not unreasonable, as the theory necessitates a value of negative infinity at RCP. However, as discussed above, simulation data results in a value of zero as the minimal entropy, not $-\infty$, therefore introducing a fitting into this study that is not possible to well match at lower values of compactivity. Without the ability to fit the entropy curve completely when approaching zero compactivity, attempts to determine $\alpha \rightarrow \alpha(z)$ and $\beta \rightarrow \beta(z)$ are beyond the scope of this paper and will be investigated in future studies. It should be noted that the exponential distribution also exactly solves $g(z_{max}) = 1$ at RCP, but does not reproduce simulated values for the entropy.

Continued analysis of the density of states revealed a need to reexamine the partition function in an effort to provide a theory to correctly predict both the equation of state and the phase diagram simultaneously. A possible solution, presented above, proposed to modify the volume function of [40], such that $w(z) \neq \langle w(z) \rangle$ necessarily. Simulations, however, do well reproduce the RLP line of the jamming phase diagram, implying that any solution for the volume function should have $\langle w(z) \rangle = \frac{2\sqrt{3}}{z}$ when approaching RLP. Such a model is extracted from the results of the entropy simulations and the mathematical structure of the partition function, and achieves the simultaneously correct predictions necessary for a more

complete theory. However, while based somewhat on simulation data, also relies on the assumption of a completely correct partition function, such that there may be insufficient physical basis for the statement $w(z) \neq \langle w(z) \rangle$. In [40] detailed analysis is provided to state otherwise. It is a possibility that this result implies a difference between the micro-canonical ensemble average and the canonical ensemble average. Further consideration on this topic is undergoing.

It is important to note that the above presented corrections to an exponential distribution for the density of states are largely due to an issue with magnitude. An exponential distribution with a very small value of h_z provides a very accurate phase diagram, but values for the entropy that are $1-2$ orders of magnitude larger than those achieved via simulation. It remains possible that the methods presented herein simply do not capture all of the entropy for jammed matter, and larger values from simulation are possible, such that corrections to the density of states and volume function would be minimized.

5.5 Conclusions

Simulation results as derived from mesoscopic fluctuations are presented in Figures 5.8 and 5.7. When comparing all the packings with different $Z(\mu)$ and ϕ, the maximum entropy is at the minimum volume fraction of RLP $\phi_{\mathrm{RLP}} \approx 0.54$ when $X \to \infty$ but only infinite friction. The minimum entropy is found for the RCP state at $\phi_{\mathrm{RCP}} \approx 0.64$ for $X \to 0$, now for all the values of friction, indicating the degeneracy of the RCP state. It is commonly believed that the RCP limit corresponds to a state with the highest number of configurations and therefore the

highest entropy. However, the states with a higher compactivity are shown to have a higher entropy, corresponding to looser packings. Within a statistical mechanics framework of jammed matter, this result is a natural consequence, and gives support to such an underlying statistical picture. Note that the values of fluctuations from simulation do not allow for an explicit divergence of the compactivity at ϕ_{RCP}, limited by methods of numerical integration. This directly affects the values of the entropy density at ϕ_{RLP}.

The values of the $s(\phi_{RLP})$ are not sufficiently large to properly integrate them within the confines of the proposed partition function and obtain the predicted equation of state. This results in the modification of the density of states, $g(z)$ and the volume function itself $w(z)$. A density of states following a power law is able to adjust the theoretical entropy such that it approximates the simulated values within reason. Further, extending the volume function beyond the assumption that it is equivalent to its average value is necessary in order to obtain a good fit for $\phi(Z_{RLP})$. It is important to note that the possibility exists that the methods presented herein do not capture the entire mesoscopic entropy of the packings. Larger values of the entropy density at RLP would eliminate the need for a modified volume function, though not the density of states which further depends on differences in $s(Z_{RLP})$ for different ensembles of constant Z. Regardless, the herein presented modifications to the mesoscopic theory explore a much larger portion of the phase diagram shown in Fig. 5.2, and well capture the values of the entropy within the scope of presented fluctuation-dissipation technique.

Each curve in the Figures 5.19 and 5.20 corresponds to a system with a different $Z(\mu)$. The projections $S(X)$ and $S(\phi)$ in Fig. 5.9 characterize the nature of

randomness in the packings. When comparing all the packings, the maximum entropy is at $\phi_{\mathrm{RLP}}^{\mathrm{min}}$ and $X \to \infty$ while the entropy is minimum for ϕ_{RCP} at $X \to 0$. Following the G-line in the phase diagram, the entropy for infinitely rough spheres shows a larger entropy for the RLP than the RCP. The same conclusion is obtained for the other packings at finite friction ($4 < Z(\mu) < 6$). Therefore, the RLP states are more disordered than the RCP states. Approaching the frictionless J-point, $\mu \to 0$ ($Z = 6$) the entropy vanishes. More precisely, it vanishes for a slightly smaller ϕ than ϕ_{RCP} of the order h_z. Strictly speaking it diverges to $-\infty$ at ϕ_{RCP} as $S \to \ln X$ for any value of Z, in analogy with the classical equation of state. However, this is an unphysical limit, as it would be considering distances in phase space smaller the minimal distance in the jamming phase space. Thus only packings with an entropy density greater than or equal to 0 are considered to as "physical" packings. Note that the compactivity curves from the theoretical model match simulation with remarkable accuracy, with lines of isocompactivity displaying a minimal discrepancy even when $X \to 0$.

At the J-point, minimal fluctuation exists with respect to Voronoi volumes associated to each grain. This implies the surprising conclusion of a minimal number of mesoscopic states for frictionless systems at the J-point . Considering these minimal fluctuations to be essentially zero, the J-point has zero entropy and no fluctuations with respect to a mesoscopic coarse-graining over the ensemble. This is the frictionless jamming transition of [63] and [64]. In principle, at the mesoscopic level this transition point is well-defined. However a mesoscopic state parameterized by a given average coordination number contains many microscopic states which are averaged out in the coarse-graining procedure to calculate the

volume function at the quasi-particle level. Therefore, these microscopic states are expected to contribute to a nonzero entropy at the J-point. It is commonly believed that the RCP limit corresponds to a state with the highest number of configurations and therefore the highest entropy. However, here the states with a higher compactivity are shown to have a higher entropy, corresponding to looser packings. At RCP the entropy vanishes. Therefore, the J-point is identified as a "Kauzmann point", or K-point, in analogy with the density, or temperature, at which the configurational entropy of a colloidal, or molecular, glass vanishes at the ideal glass transition [96]. From this point the entropy increases monotonically with X, being maximum for the RLP limit. Packings with packing fractions above RCP to $\phi_{fcc} = 0.74$, the optimal packing fraction for spheres in 3d, do not appear in the theory because they exhibit some degree of order, or crystallization. By doing so, crystals or partially crystalline packings are explicitly not considered in the ensemble. While the Alexander conjecture suggests that this implies an upper bound of $z = 6$ for the geometrical coordination number, simulation data finds that this limit may fluctuate towards higher values for z, with $z = Z = 6.2$ at the J-point, presented herein. Packings with $6 < Z \leq 6.2$ may or may not exhibit partial crystallization, though none of the grains have $Z = 12$.

This implies an intrinsic difference between the mesoscopic theory, where $s \to -\infty$ at the K-point, and the full Edwards' entropy given by Eq. (5.14) and calculated in the simulations, where $s \to 0$ at the K-point. The mesoscopic entropy is augmented by the entropy of the microscopic states to obtain the full entropy as $s = s_{\text{meso}} + s_{\text{micro}}$. Since for frictionless packings s_{meso} vanishes, then $s = s_{\text{micro}}$, implying that one can obtain s_{micro} from the full entropy of the K-point as calculated

numerically. Therefore, Fig. 5.21 is plotted as $s_{\text{meso}} + 1.1\lambda$ to obtain a plot of the full mesoscopic entropy as calculated from the theoretical prediction of Chapter 3, for $Z = 4.3$ along the G-line from simulation.

The differences displayed between theoretical and simulated entropy can to some extent be considered within the scope of disagreement between classical and quantum entropy. Classical entropy measurements are primarily interested in ΔS, having a minimum value of 0 when approaching the ground state, though $S \to -\infty$. Quantum entropy measurements assume a minimum value of phase space over which one can integrate degrees of freedom for a give system. This results in a $S = 0$ exactly at the ground state. Determination of a well defined minimum phase space volume for jammed matter would adjust the number of available microstates, Ω, within the micro-canonical ensemble as presented by Edwards, and will be the topic of future study.

In summary, a notion of jamming is presented that applies to frictional hard spheres, as well as frictionless ones. The entropy reveals interesting features of the RCP and RLP states such as the fact that RLP is maximally random with respect to RCP and that both limits can be seen in terms of the entropy and equation of state. Overall, the agreement between theory and simulation is sufficient to indicate that the methods presented herein are appropriate for evaluating the entropy of jammed matter and characterizing randomness in systems of identical spheres.

Bibliography

[1] L. D. Landau and E. M. Lifshitz, *Statistical Physics*, (Pergamon, New York, 1970).

[2] L. F. Cugliandolo, J. Kurchan and L. Peliti, *Phys. Rev. E* **55**, 3898 (1997).

[3] S. A. Langer and A. J. Liu, *Europhysics Lett.* **49**, 68 (2000).

[4] A. Barrat, J. Kurchan, V. Loreto and M. Sellitto, *Phys. Rev. Lett.* **85**, 5034 (2000).

[5] F. Sciortino and P. Tartaglia, *Phys. Rev. Lett.* **86**, 107 (2001).

[6] J. L. Barrat and L. Berthier, *Phys. Rev. E* **63**, 012503 (2001).

[7] I. K. Ono, C. S. O'Hern, D. J. Durian, S. A. Langer, A. J. Liu and S. R. Nagel, *Phys. Rev. Lett.* **89**, 095703 (2002).

[8] H. A. Makse and J. Kurchan, *Nature* **415**, 614 (2002).

[9] S. F. Edwards, The role of entropy in the specification of a powder, in *Granular Matter: an Interdisciplinary Approach* (Mehta, A., editor) 121-140 (Springer-Verlag, New York, 1994).

[10] H. M. Jaeger, S. R. Nagel and R. P. Behringer, *Rev. Mod. Phys.* **68**, 1259 (1996).

[11] D. W. Howell, R. P. Behringer and C. T. Veje, *Phys. Rev. Lett* **82,** 5241 (1999).

[12] C. T. Veje, D. W. Howell and R. P. Behringer, *Phys. Rev. E* **59,** 739 (1999).

[13] D. M. Mueth, G. F. Debregeas, G. S. Karczmar, P. J. Eng, S. R. Nagel, and H. M. Jaeger, *Nature* **406**, 385 (2000).

[14] D. M. Mueth *Phys. Rev. E* **67**, 011304 (2003).

[15] B. Utter and R. P. Behringer, *Phys. Rev. E* **69**, 031308 (2004).

[16] R. Nedderman, *Statics and Kinematics of Granular Materials* (Cambridge Univ. Press, Cambridge, 1992).

[17] T. G. Drake, *J. Geophys. Res.* **95**, 8681 (1990).

[18] C. Song, P. Wang, and H. A. Makse, *Proc. Nat. Acad. Sci.* **102**, 2299 (2005).

[19] P. Wang, C. Song and H. A. Makse, *Nature Physics* **2**, 526 (2006).

[20] E. R. Nowak, J. B. Knight, E. BenNaim, H. M. Jaeger and S. R. Nagel, Phys. Rev. E **57**, 1971 (1998).

[21] R. Khosropour, J. Zirinsky, H. K. Pak and R. P. Behringer, *Phys. Rev. E* **56**, 4467 (1997).

[22] J. A. Drahun and J. Bridgwater, *Powder Technol.* **36**, 39 (1983).

[23] G. Taylor, *Proc. Roy. Soc. A* **219**, 186 (1953).

[24] G. D'Anna, P. Mayor, A. Barrat, V. Loreto and F. Nori, *Nature* **424**, 909 (2003).

[25] D. C. Rapaport, *The Art of Molecular Dynamics Simulation* (Cambridge University Press, Cambridge, 1995).

[26] A. Coniglio, A. Fierro, H. J. Herrmann and M. Nicodemi, (eds) *Unifying Concepts in Granular Media and Glasses* (Elsevier, Amsterdam, 2004).

[27] S. B. Savage, *Adv. Appl. Mech.* **24**, 289 (1994).

[28] G. I. Tardos, S. McNamara and I. Talu, *Powder Tech* **131** 23 (2003).

[29] N. Xu and C. S. O'Hern, *Phys. Rev. Lett.* **94**, 055701 (2005).

[30] K. Feitosa and N. Menon, *Phys. Rev. Lett.* **88**, 198301 (2002).

[31] A. J. Liu and S. R. Nagel, (eds) *Jamming and Rheology: Constrained Dynamics on Microscopic and Macroscopic Scales*, (Taylor & Francis, London, 2001).

[32] A. Mehta and T. C. Halsey, (eds) *Challenges in Granular Physics* (World Scientific, Singapore, 2002).

[33] H. Hinrichsen and D. E. Wolf, (eds) *The Physics of Granular Media* (Wiley-VCH Verlag, 2004).

[34] S. F. Edwards and R. B. S. Oakeshott, *Physica A* **157**, 1080 (1989).

[35] J. Kurchan, *J. Phys.: Condens. Matter* **12**, 6611 (2000).

[36] A. Fierro, M. Nicodemi and A. Coniglio, *Europhys. Lett.* **59**, 642 (2002); A. Fierro, M. Nicodemi, and A. Coniglio, *Phys. Rev. E* **66**, 061301 (2002).

[37] A. Mehta and J. M. Luck, *J. Phys. A.: Math. Gen.* **36**, L365 (2003).

[38] J. Berg and A. Mehta, *Phys. Rev. E* **65**, 031305 (2002).

[39] H. A. Makse, J. Brujić and S. F. Edwards, Statistical Mechanics of Jammed Matter, in H. Hinrichsen and D. E. Wolf, (eds) *The Physics of Granular Media* (Wiley-VCH Verlag, 2004).

[40] C. Song, P. Wang and H. A. Makse, *Nature* **453**, 629 (2008).

[41] R. P. Behringer and J. T. Jenkins, eds., Powders & Grains 97 (Balkema, Rotterdam, 1997).

[42] T. C. Hales. The Kepler conjecture. http://arxiv.org/abs/math.MG/9811078

[43] J. D. Bernal and J. Mason, Nature **188**, 910 (1960).

[44] Anonymous, Nature **239**, 488 (1972).

[45] G. D. Scott, and D. M. Kilgour, Brit. J. Appl Phys (J. Phys. D) **2**, 863-866 (1969); G. D. Scott, Nature, **188**, 908 (1960).

[46] J. L. Finney, Proc. Roy. Soc. London, Ser. A **319**, 479 (1970).

[47] J. D. Berryman, Phys. Rev. A **27**, 1053-1061 (1983).

[48] G. Y. Onoda, and E. G. Liniger, Phys. Rev. Lett. **64**, 2727 (1990).

[49] S. Henkes and B. Chakraborty, Phys. Rev. Lett. **95**, 198002 (2005).

[50] R. Blumenfeld, On entropic characterization of granular materials, in Lecture Notes in Complex Systems Vol. 8: Granular and Complex Materials, 43-53, eds (2007).

[51] S. F. Edwards, *Physics A* **353**, 114 (2005).

[52] R. C. Ball and R. Blumenfeld, Phys. Rev. Lett. **88**, 115505-1 (2002).

[53] R. Blumenfeld and S. F. Edwards, Phys. Rev. Lett. **90**, 114303-1 (2003).

[54] R. Blumenfeld, Eur. Phys. J. B **29**, 261 (2002).

[55] T. Aste, M. Saadatfar, T. J. Senden, J. Stat. Mech., P07010 (2006).

[56] M. Schröter, D. I. Goldman, H. L. Swinney, Phys. Rev. E **71**, 030301(R) (2005).

[57] F. da Cruz, F. Lechenault, O. Dauchot, and E. Bertin, Powders and Grains 2005, R. García-Rojo, H. J. Herrmann, and S. McNamara Eds. (A. A. Balkema, Rotterdam, 2005).

[58] F. Léchenault, O. Dauchot and E. Bertin, J. Stat. Mech., P07009 (2006). E. Bertin, O. Dauchot and M. Droz, Phys. Rev. Lett. **96**, 120601 (2006).

[59] J. Zhou, S. Long, Q. Wang and A. D. Dinsmore, Science **312**, 1631 (2006).

[60] J. Brujić *et al.*, Physica A **327**, 201 (2003).

[61] S. Torquato, T. M. Truskett, P. G. Debenedetti, Phys. Rev. Lett. **84**, 2064 (2000).

[62] S. F. Edwards and D. V. Grinev, Phys. Rev. Lett. **82**, 5397 (1999).

[63] H. A. Makse, D. L. Johnson and L. M. Schwartz, Phys. Rev. Lett. **84**, 4160 (2000).

[64] C. S. O'Hern, S. A. Langer, A. J. Liu, and S. R. Nagel, Phys Rev. Lett. **88**, 075507 (2002).

[65] L. E. Silbert, D. Ertas, G. S. Grest, T. C. Halsey, D. Levine, Phys. Rev. E **65**, 031304 (2002).

[66] T. Under, J. Kertesz, and D. E. Wolf, Phys. Rev. Lett. **94**, 178001 (2005).

[67] S. Alexander, Phys. Rep. **296**, 65 (1998).

[68] C. S. O'Hern, L. E. Silbert, A. J. Liu, and S. R. Nagel, Phys. Rev. E **68**, 011306 (2003).

[69] K. Shundyak, M. van Hecke and W. van Saarloos, Phys. Rev. E **75**, 010301 (2007).

[70] L. D. Landau and E. M. Lifshitz, Theory of Elasticity, (Pergamon, NY, 1970).

[71] R. D. Mindlin, J. Appl. Mech. (ASME) **71**, (1949).

[72] H. Zhang and H. A. Makse, Phys. Rev. E **72** 011301 (2005).

[73] G. Parisi, and F. Zamponi, J. Chem. Phys. **123**, 144501 (2005); arXiv:cond-mat/08022180.

[74] S. Torquato, F. H. Stillinger, *J. Phys. Chem B* **105**, 11849 (2001).

[75] J. Brujić, P. Wang, C. Song, D. L. Johnson, O. Sindt, and H. A. Makse, Phys. Rev. Lett. **95**, 128001 (2005).

[76] F. Zamponi, Nature **453**, 606 (2008).

[77] M. P. Ciamarra, A. Coniglio, M. Nicodemi, Phys. Rev. Lett. **97**, 158001 (2006).

[78] P. Philippe, and D. Bideau, Europhys. Lett. **60**, 677 (2002).

[79] H. A. Makse, N. Gland, D. L. Johnson, and L. M. Schwartz, Phys. Rev. Lett. 83, 5070 (1999);

[80] H. A. Makse, N. Gland, D. L. Johnson, and L. M. Schwartz, Phys. Rev. E **70**, 061302 (2004).

[81] R. L. C. Vink and G. T. Barkema, Phys. Rev. Lett. **89**, 076405 (2002).

[82] P. Rombouts, R. L. C. Vink, Master's Thesis, (2004)

[83] A. Donev *et al.*, Science **303**, 990 (2004).

[84] P. Richard *et al.*, Phys. Rev. E **68**, 020301 (2003).

[85] T.G. Mason, J. Bibette and D. A. Weitz, Phys.Rev. Lett **75**, 2051 (1995).

[86] C. Mabille *et al.*, Langmuir **16**, 422 (2000).

[87] C. E. Shannon, Bell Sys. Tech. J. **27**, 1948 (1948).

[88] B. D. McKay, Nauty user's guide (version 1.5), Tech. Rep. TR-CS-90-02, Australian National University (1990).

[89] F. Krzakala and J. Kurchan, Phys. Rev. E **76**, 021122 (2007).

[90] Stealing the gold: a celebration of the pioneering physics of Sam Edwards, P. M. Goldbart, N. Goldenfeld, D. Sherrington, eds. (Oxford Science Publications, Oxford, 2004).

[91] Moukarzel, C. and Duxbury, P. M. and Leath, P. L., Phys. Rev. Lett. 78, 1480 - 1483 (1997)

[92] S. F. Edwards and D. V. Grinev, Statistical physics of the jamming transition: the search for simple models in Jamming and Rheology, Eds. A. Liu and S. R. Nagel (Taylor and Francis, New York, 2001).

[93] T. Aste and T. Di Matteo, Phys. Rev. E 77, 021309 (2008)

[94] T. Aste, A. V. Anikeenko and N. N. Medvedev, Phys. Rev E 77, 031101 (2008)

[95] M. P. Caimarra and A. Coniglio, Phys. Rev. Letters **101**, 128001 (2008).

[96] F. H Stillinger, Science **267**, 1935-1939 (1995).